Synthesis and thermoelectric studies of a narrow gap semiconducting alloy for cooling: BiSb

Sheng Gao

Advisor: Professor Joseph Poon

A Dissertation Presented to the Graduate Faculty
of the University of Virginia in Candidacy for the Degree of
Doctor of Philosophy

Department of Physics

University of Virginia

May, 2019

Abstract

Thermoelectric (TE) technology plays a vital role in heat-to-electrical energy conversion and refrigeration. Bismuth antimony (Bi-Sb) is one of the most promising materials for thermoelectric cooling. Therefore my research target was focused on designing, preparing and characterizing Bi-Sb alloys to achieve a high figure of merit ZT. Herein a high figure of merit ZT near 0.6 at cryogenic temperatures (100-150K) in zero magnetic field has been measured in nanocrystalline bulk n-type $Bi_{85}Sb_{15}$, nearly 50% higher than the polycrystalline-averaged ZT $\sim$ 0.4 of single crystal Bi-Sb from Yim and Amith. Magneto-thermoelectric effects of this nanobulk Bi-Sb further improved the TE properties. ZT was enhanced to $\sim$0.7 in a portable and compact BiSb/NdFeB material system. The improved thermoelectric properties can be attributed to the nanoscale microstructure achieved from rapid solidification, which not only significantly reduced the thermal conductivity but also avoided a segregation effect.A record low thermal conductivity of 1.5 W/m·K was measured using the "hot disk" method. The thermoelectric properties were analyzed within a two-band effective mass model, providing a deeper understanding of the transport mechanisms for this intriguing semimetal-semiconductor alloy system. The study revealed a gradual narrowing of the band gap at increasing temperature for the first time. The easily accessible low magnetic field for achieving high ZT enables the utilization of n-type BiSb in thermoelectric cooling applications. On the other hand, because of the demand of similar n-p TE legs in TE devices, great efforts were put into the investigation of doping effects to develop TE properties of p-type Bi-Sb system to build a similar counterpart to the intrinsic n-type Bi-Sb. Transition metals were used to suppress the electron mobility for a stronger p-type performance. One of the best ZT so far $\sim$ 0.13 around 200K was achieved with Ni and Pb co-doped p-type Bi-Sb alloy. The gap decreasing behavior mentioned before could be a heretofore unrealized obstacle to achieving a high thermoelectric figure of merit in p-type Bi-Sb alloys comparing with the n-type counterpart. After all, the present nano-structured Bi-Sb alloys can already be readily utilized in thermoelectric cooling applications.

This thesis started with the introduction of basic concepts of TE physics followed by a detailed description of experiments procedure and analysis of measurements data.

Acknowledgments

Great appreciation to my advisor prof. Joseph Poon's guidance during my Ph.D. study. He was the one who led the directions of the whole project to keep me moving forward. He also gave me lots of advice in time when I was stuck with difficulties.

Thanks to our collaborators prof. Patrick Hopkins and dr. John Gaskins that put in a lot of efforts into the thermal conductivity(TC) measurements of our samples and figured the inaccuracy of traditional PPMS TC measurements.

Thanks to my co-worker Xixiao Hu who helped with the sample preparations and essential works on the two-band transportation model simulations that revealed the indirect energy gap narrowing.

This work was supported by the Defense Advanced Research Projects Agency MATRIX Program contract HR0011-16-C-0011 (P.I. Dr. Rama Venkatasubramanian, Johns Hopkins University Applied Physics Laboratory). Also thank Dr. Normand Modine (Sandia National Laboratories) for his important input of density funtional theory (DFT) calculation.

More thanks to my parents and all my friends that always support me from behind during these years without hesitations.

I will not be able to finish my Ph.D. study without any of these helps above, thank you all!

Contents

List of Figures

List of Tables

Chapter 1

Introduction to Thermoelectric Materials

1.1 What are thermoelectric materials?

Generally speaking, thermoelectric(TE) materials are the ones which can directly convert a temperature difference into an electrical voltage or vice versa, generate temperature gradient when applied an electrical voltage across the material. These conversion behaviors between thermal and electrical energies are known as **thermoeletric effects**. Many materials more or less have some abilities to convert heat to electricity, but only the ones that have strong thermoelectric effects are called thermoelectric materials. In order to quantify thermoelectric effects, here we will start from the classification of different types of thermoelectric effects: **Seebeck effect**, **Peltier effect** and **Thomson effect**.

1.1.1 Seebeck effect

The Seebeck effect is the direct conversion from temperature gradient into electrical voltage. Since different materials will have different Seebeck effect power, therefore an electrical potential difference could also be detected at the junction of wires made by different materials. This is also the origin of thermocouples. See Fig. 1-1. Seebeck effect was firstly discovered in 1794 by Italian scientist Alessandro Volta, then independently rediscovered by the Baltic German physicist Thomas Johann Seebeck in 1821 and obtained its current name [1].

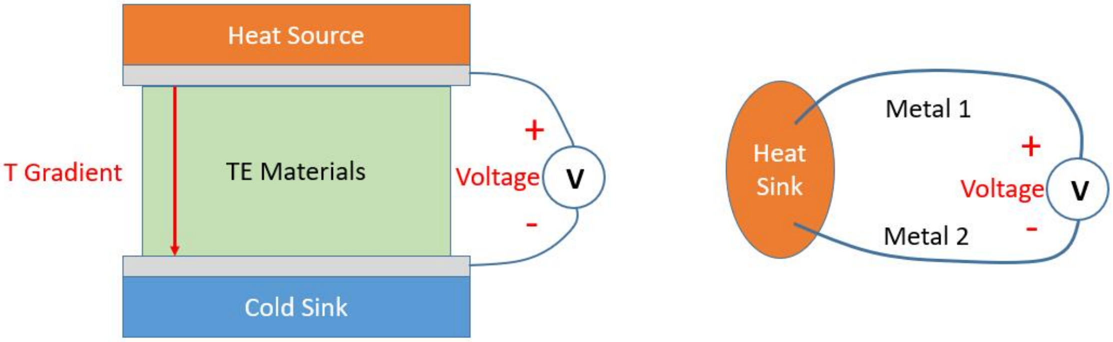

Figure 1-1: Demonstrations of the Seebeck Effect

To quantitatively describe Seebeck effect, the **Seebeck coefficient** was defined in the following equation:

$$\mathrm{S} = -\frac{\Delta V}{\Delta T} \tag{1.1}$$

where ΔV and ΔT are the thermoelectric voltage and temperature difference seen at the two ends, S is the Seebeck coefficient, also known as the thermopower. Note that usually this Seebeck voltage cannot be measured directly since the additional voltage contribution from the Seebeck effect of voltmeter leads always exists. So the further modification depending on the wire Seebeck coefficient is usually needed.

In a more general and technical description the Seebeck coefficient is defined in terms of electric current vector as in the differential equation:

$$\vec{J} = -\sigma \nabla V - \sigma S \nabla T \tag{1.2}$$

where $\vec{J}$ is the current density and σ is the electrical conductivity. When the system reaches its steady state where $\vec{J} = 0$ then the equation returns to the special case we had before in Eq. 1.1.

From the point of view of microscopic physics, the physical factors that determined the Seebeck coefficient are two significant things: charge-carrier diffusion and phonon drag [2]. Considering a uniform temperature gradient applied on a conductive material. The hotter end is more variation in energies compared to the colder end, this means that high energy levels have a higher carrier occupation per state on the hotter side. So when the carriers start to diffusive from two ends to the other, the carriers at the hotter end will have a stronger drift, therefore the net current will be generated and in the end, the Seebeck coefficient will be built. In particular, in electronic materials with weak electron-electron interactions, weak electron-phonon interactions, the process described above could be expressed using **Mott relations** [3]:

$$\sigma S = \frac{k_B}{-e} \int \frac{E-\mu}{k_B T} c(E) \left(-\frac{df(E)}{dE} \right) dE \tag{1.3}$$

where $c(E)$ is the energy-dependent conductivity, $f(E)$ is the FermiâĂŞDirac distribution function. The linear response conductance can be described using:

$$\sigma = \int c(E) \left(-\frac{df(E)}{dE} \right) dE \tag{1.4}$$

and the derivative

$$-\frac{df(E)}{dE} = \frac{1}{4k_B T} \mathrm{sech}^2 \left(\frac{E-\mu}{2k_B T} \right) \tag{1.5}$$

is a function peaked around the chemical potential μ with a width of approximately $3.5k_BT$. In metals and semiconductors, these formulas can be further developed into special expression, the details will not be addressed too much on here.

With the mechanics described above, when we come to discuss systems with two or more transport channels the effective Seebeck coefficient can be described using the conductivity weighted average of each channel:

$$S' = \frac{\sum_i \sigma_i S_i}{\sum_i \sigma_i} \tag{1.6}$$

The sign of the Seebeck coefficient needs to be considered when involved with systems of different type of carriers.

1.1.2 Other thermoelectric effects

As mentioned before, besides the Seebeck effect, there are also other thermoelectric effects occurs at certain situation. Since my research was focused on the Seebeck effect of the materials, so here I will only give a brief introduction about the other thermoelectric effects.

Peltier effect can be seen as the reversed Seebeck effect, which is the presence of heating or cooling at an electrified junction of two different conductors. It is named after French physicist Jean Charles Athanase Peltier, who discovered it in 1834 [4]. The Peltier heated per unit time $\dot{Q}$ generated at the junction can be expressed as:

$$\dot{Q} = (\Pi_A - \Pi_B)I \tag{1.7}$$

where Π_A and Π_A are the Peltier coefficients for the two conductors A and B respectively. The total heat generated may also include the Joule heat and thermal-gradient effects. The Peltier effect can be considered as the back-action counterpart to the Seebeck effect, there is a close relationship between the Seebeck coefficient and Peltier coefficient as:

$$\Pi = TS \tag{1.8}$$

Thomson effect describes the heating or cooling of a current-carrying conductor with a temperature gradient. In some material the Seebeck coefficient has temperature dependence, therefore a spatial temperature gradient on this material will result in a gradient in the Seebeck coefficient. And applying current to this system will also lead to a continuous version of the Peltier effect:

$$\dot{q} = -\mathrm{K}\vec{J} \cdot \nabla T \tag{1.9}$$

where $\dot{q}$ is the heat production rate per unit volume and K is the Thomson coefficient, which is related to the Seebeck coefficient as:

$$\mathrm{K} = T\frac{dS}{dT} \tag{1.10}$$

The Eq. 1.9 ignored the Joule heating and ordinary thermal conductivity, which can be included in the full thermoelectric equation as:

$$-\dot{q}_{ext} = \nabla \cdot (\kappa \nabla T) + \vec{J} \cdot (\sigma^{-1}\vec{J}) - T\vec{J} \cdot \nabla S \tag{1.11}$$

where $\dot{q}_{ext}$ is the heat added from an external source and κ is the thermal conductivity. This equation is valid in the case where the material has reached a steady state, the charge and temperature distributions are stable. The Last term in Eq. 1.11 described the thermoelectric effects in the system.

1.2 Why are thermoelectric materials important?

In modern society, energy sources have become a more and more hot topic. Scientists put many efforts into collecting and reuse of the massive amount of waste heat generated all the time everywhere in our daily life. Thermoelectric technology plays an essential role in heat-to-electrical energy conversion and refrigeration in an environmentally friendly manner. There are already many mature applications based on thermoelectric materials, the most popular commercialized ones are **thermoelectric generator** and **thermoelectric refrigerator**.

1.2.1 Thermoelectric generator

A thermoelectric generator can directly convert heat flux into electrical power through the Seebeck effect. Comparing with the traditional heat engine, it may be less efficient and more expensive, but the completely solid state design win thermoelectric generator important role in severe environment operations and it is also in synergistic with existing production methods. For examples, their non-orientation dependent allowing for use in zero-gravity or deep sea applications [5]. Thermoelectric generators also have no moving parts which produces a more reliable device that does not require maintenance for long periods. The durability and environmental stability have made thermoelectrics a favorite for NASA's deep space explorers among other applications [6]. Another critical advantage of thermoelectric generators outside of such specialized applications is that they can potentially be integrated into existing technologies to boost efficiency and reduce environmental impact by producing usable power from waste heat [7,8].

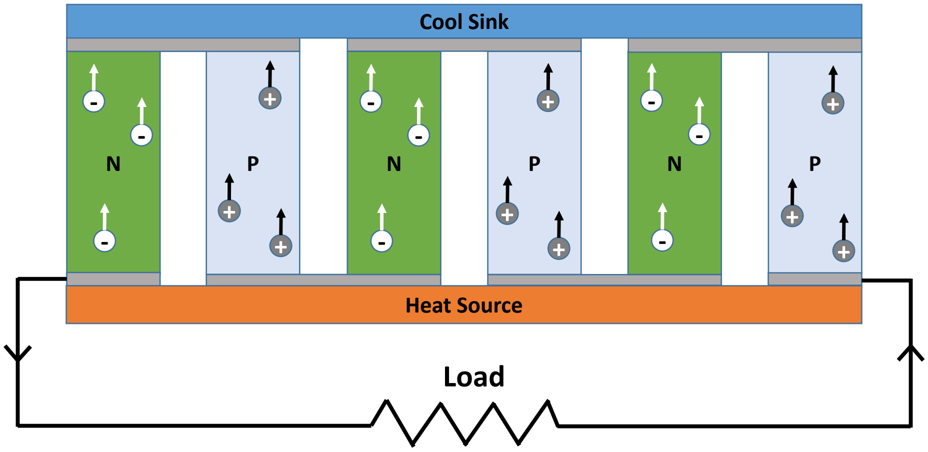

Figure 1-2: Demonstrations of Thermoelectric Generator

In Fig. 1-2, a simplified diagram demonstrated the basic working mechanism of thermoelectric generators. Since n-type and p-type thermoelectric materials have the opposite sign of the Seebeck coefficient, so giving the sample temperature gradient, an inverse Seebeck voltage will be generated. Connecting several n-p TE legs in series as shown in the figure, an electrical circuit is formed providing electrical power to the external load in the circuit. During this process, negative charges in the n-type leg and positive charges in the p-type leg are both moving toward the cold end and recombined there releasing energies. Therefore, the thermal power maintaining the temperature gradient is converted into electrical energy.

1.2.2 Thermoelectric refrigerator

Having the basic concepts of the thermoelectric generator, it is very natural to develop the same idea to a thermoelectric cooling device — in a reversed way. The thermoelectric refrigerator uses the Peltier effect to create a heat flux carrying heat from the cooled surface to a hotter end, this process is purely driven by an external electrical power connected to the thermoelectric n-p legs, as shown in Fig. 1-3. The negative charges of n-type legs and positive charges of p-type legs in the cold end are pushed to the hot end due to the electrical current, keep carrying thermal energies from the low-temperature terminal to the heat sink for dissipation.

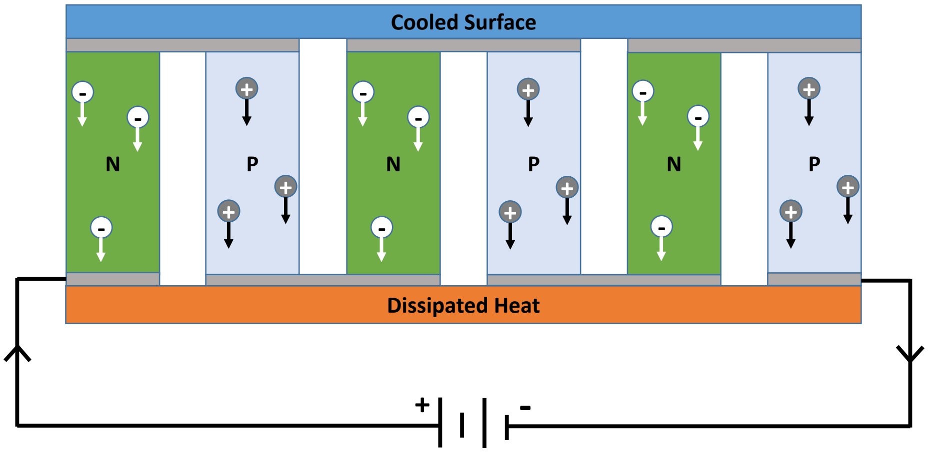

Figure 1-3: Demonstrations of Thermoelectric Refrigerator

The benefits of a thermoelectric refrigerator also come from its integrity. The lack of mechanical wear increases the lifespan of the system and lowers the maintenance requirement. Current technologies show the mean time between failures (MTBF) to exceed 100,000 hours at ambient temperatures [9]. Another significant advantage of thermoelectric cooler over the traditional coolers is the non-requirement of refrigerants during operation, this core feature creates an environmentally friendly way of refrigeration. However, thermoelectric coolers also have their own shortages. These systems are used in environments where the temperature difference between either end of the semiconductors is so small that it would not be possible to generate a large heat flux from it, and only a small amount of heat flux can be dissipated. In other words, it will be less efficient when dealing with large scale cooling works.

Even with its disadvantages, thermoelectric refrigerators already widely used in a variety of applications of different fields. For examples, in customer products like portable coolers, cooling electronic components and small instruments, tiny thermoelectric coolers can be found around our daily life. It is also shinning in industrial manufacturing, some of the applications include industrial electronics and telecommunications, automotive, laser equipment, thermoelectric air conditioners or coolers, mini refrigerators or incubators, military cabinets, IT enclosures, and more. Scientific devices are another relevant field. They are a common component in thermal cyclers, used for the synthesis of DNA by polymerase chain reaction (PCR), a common molecular biological technique, which requires the rapid heating and cooling of the reaction mixture for denaturation primer annealing and enzymatic synthesis cycles [10].

1.3 What are good thermoelectric materials?

Seeing all these applications of thermoelectric technologies, here naturally rises a question, what are good thermoelectric materials? In other words, what is the most crucial feature that is needed in thermoelectric devices? As we know, thermoelectric devices are the ones which convert energies between thermal and electricity, during this process, it is inevitable to have energy loss such as Joule heat or other forms. Therefore, we may need to ask what is the **energy conversion efficiency** of our systems, which leads to the directions of pursuing better thermoelectric materials.

1.3.1 Energy Conversion Efficiency

Using thermoelectric generator as an example, based on the definition, the energy conversion efficiency can be written as:

$$\eta=\frac{\text{power provided to the load}}{\text{heat input to the device}} \tag{1.12}$$

In a simplified case assuming the generator consists of one of each n-type and p-type thermoelectric leg. And the external load can be expressed by a resistance R_L, then the output power will be:

$$P_O = I^2 R_L \tag{1.13}$$

where I is the current going through the load. On the other hand, the net heat absorbed can be estimated from the sum of the Peltier, Fourier, and Joule heat terms [11]:

$$Q_{IN} = S_h I T_h + \bar{K}\Delta T - 0.5 I^2 (R_n + R_p) \tag{1.14}$$

where S_h and T_h are the Seebeck coefficient and temperature at the hot end, $\bar{K}$ is the average thermal conductance, ΔT is the temperature difference of two ends, R_n and R_p are the resistances of n-type and p-type legs respectively.

By putting Eq. 1.13 and Eq. 1.14 into Eq. 1.12, expressing all the terms using thermoelectric transport parameters, then taking derivative of R_L, one could find that in the ideal case, the maximum efficiency of a thermoelectric generator can be expressed as [12–14]:

$$\eta_{\max} = \frac{\Delta T}{T} \frac{\sqrt{1 + Z\bar{T}} - 1}{\sqrt{1 + Z\bar{T}} + \frac{T_c}{T_h}} \tag{1.15}$$

where T_c is the temperature of the cold end, and $Z\bar{T}$ is the modified dimensionless figure of merit, which takes into consideration the thermoelectric capacity of both thermoelectric materials being used in the device and, after geometrical optimization regarding the legs sections, is defined as [15]:

$$Z\bar{T} = \frac{(S_p - S_n)^2 \bar{T}}{(\sqrt{\rho_n \kappa_n} + \sqrt{\rho_p \kappa_p})^2} \tag{1.16}$$

where n and p subscripts represent n-type and p-type thermoelectric legs, S_p and S_n are the Seebeck coefficients, ρ_n and ρ_p are the resistivities, κ_n and κ_p are the thermal conductivities, $\bar{T}$ is the average temperature between the hot and cold surfaces.

On the other hand, the efficiency of a thermoelectric refrigerator can be derived in the same way and get similar results. Using real industrial values to put into Eq.

1.15, it can be estimated that with current thermoelectric technologies, the efficiency of commercial-level thermoelectric devices is only around 10% [11], which still has a large space to be improved in the future.

1.3.2 Figure of merit ZT

From the expression of modified dimensionless figure of merit in Eq. 1.16 for two legs, by decoupling the two components, we can write down the themoelectric figure of merit for one type of material using the same form:

$$ZT = \frac{S^2}{\rho\kappa}T = \frac{S^2}{\rho(\kappa_L + \kappa_e + \kappa_b)}T \tag{1.17}$$

where S is the Seebeck coefficient, ρ is the resistivity. κ is the total thermal conductivity, including lattice thermal conductivity κ_L, electronic thermal conductivity κ_e and sometimes also bipolar thermal conductivity κ_b.

It is rather easy to understand this formula based on how thermoelectric material works in the device. First of all, it is good to generate large electrical voltages using a small heat gradient, therefore a high Seebeck coefficient is crucial, which is expressed in a square term related to ZT. Secondly, since the thermoelectric legs are actually part of the circuit, by reducing the resistivity of the legs, the energy loss in the form of Joule heat will be significantly reduced. At the same time, there will be a larger portion of voltage potential being distributed to the external load. At last, having a small thermal conductivity will reduce the efforts needed to keep the thermal gradient on the device. Overall, a thermoelectric material with a high figure of merit ZT will lead to a high-performance TE device.

Using a simple single parabolic band model, the three main factors related to figure of merit can be expressed as [16]:

$$S = \frac{8\pi^2 k_{\mathrm{B}}^2}{3eh^2} m^* T \left(\frac{\pi}{3n}\right)^{2/3} \tag{1.18}$$

$$\sigma = 1/\rho = ne\mu \tag{1.19}$$

$$\kappa_{\mathrm{e}} = L\sigma T = ne\mu LT \tag{1.20}$$

where $m*$ is the effective mass of the carrier, n is the carrier concentration, σ is the electric conductivity, e is the electrical charge of an electron, k_B is the Boltzmann constant, μ is the carrier mobility, and L is the Lorenz number.

Eq. 1.18 to Eq. 1.20 shows that all of these thermoelectric parameters are entangled with each other, which is the major difficulties when pursuing a higher figure of merit ZT. When one tries to increase the electrical conductivity by introducing more carriers, the Seebeck coefficient will be decreased at the same time due to higher carrier concentrations. Moreover, the electrical thermal conductivity even has the full electrical conductivity term as a factor. Therefore it is very difficult to decrease resistivity without affecting the thermal conductivity. In Fig. 1-4 a typical ZT dependence of carrier concentration shows the fights between different thermoelectric factors that determined a narrow region with optimized ZT [17].

Over the years, there were many different efforts putting into investigating higher figure of merit ZT for thermoelectric materials [18–35]. One of the most of effective strategies are decouple σ or S to simultaneously increase their values by optimizing carrier concentration n [16, 36] and band engineering [37–41]. Such as varying compositions, introducing dopants, manipulating the defects to tune the bandgap and effective mass, and also possibly achieve resonant states. On the other hand, the nano-structure engineering increased the phonon scattering, that significantly reduced lattice thermal conductivity κ without sacrificing the electrical transport properties [42–46]. So overall the figure of merit ZT can be enhanced from a different aspect.

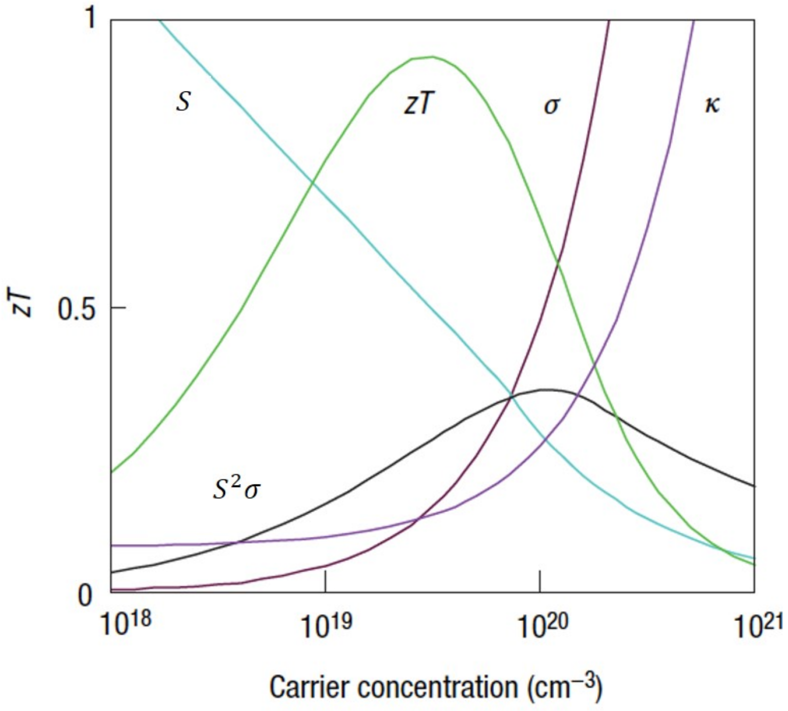

Figure 1-4: Figure of Merit ZT Varying with Carrier Concentration

1.4 Bi-Sb alloy

Because of the demands of various applications, the studies of thermoelectric materials were across a large temperature range from cryogenic temperature (0K to 150K) all the way up to thousands of Kelvins. Most of the materials are semiconducting binary or ternary compounds and alloys, such as Half-Heusler alloys, Bi-Te alloys, Perovskite alloys and so on. Fig. 1-5 shows the state-of-the-art until 2018 of typical thermoelectric materials in a temperature dependent ZT plots [18, 37, 47–60]. Even though there are many different kinds of thermoelectric materials, only a few of them could have a decent performance at cryogenic temperatures (0K to 150K). Among these low-temperature friendly materials, Bi-Sb alloys stood out due to its narrow energy gap (<30mEV) became one of the best thermoelectric materials. Fig. 1-6 shows some selected figure of merit ZT data for typical cryogenic temperature thermoelectric material [61–64]. It is clear that Bi-Sb alloys have obvious advantages over other listed low-temperature TE materials between 50K to 200K. Therefore this promising TE material had attracted attention from many researchers for more than

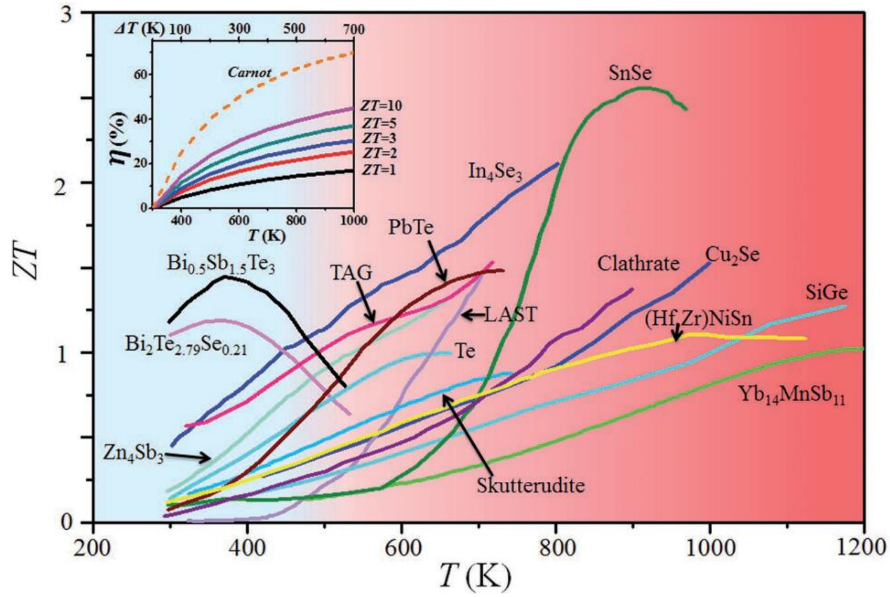

Figure 1-5: Temperature Dependent ZT of Typical Thermoelectric Materials

50 years [65,66]. In this section, a brief introduction of Bi-Sb alloy will be given from the space structure to both of the electrical and thermal properties.

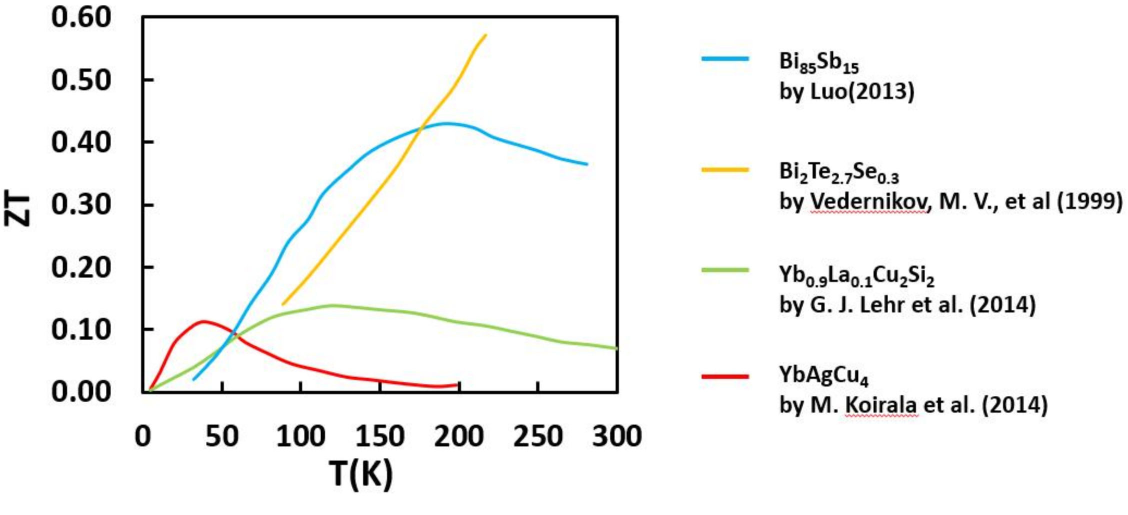

Figure 1-6: ZT of N-type Cryogenic Temperature Thermoelectric Materials

1.4.1 Crystal structure

All the three semimetals of group V share the same rhombohedral A_7 structure of space group $R_{\bar{3}}m$. Fig. 1-7 shows both rhombohedral primitive unit cell and structure in hexagonal representation. The primitive unit cell is described by three parameters: (1) The side of the rhombohedral a_R, (2) The rhombohedral angle α_R and (3) the atomic parameter u. Each unit cell contains two atoms A and B. In the hexagonal representation, the structure is described using the height and the side length of the hexagonal cylinder. The rhombohedral structure has one trigonal axis of threefold symmetry and three two-fold or binary axes each normal to the trigonal direction, as marked in the Fig. 1-7. Given this crystallographic symmetry and the principle of microscopic reversibility, any properties of Bi-Sb alloys described by a spacial tensor are limited. For example, the electrical resistivity ρ, the Seebeck coefficient S, and the thermal conductivity κ, have only two independent components, one along the trigonal axis (index 33) and one in the basal plane (index 11 or 22) [67].

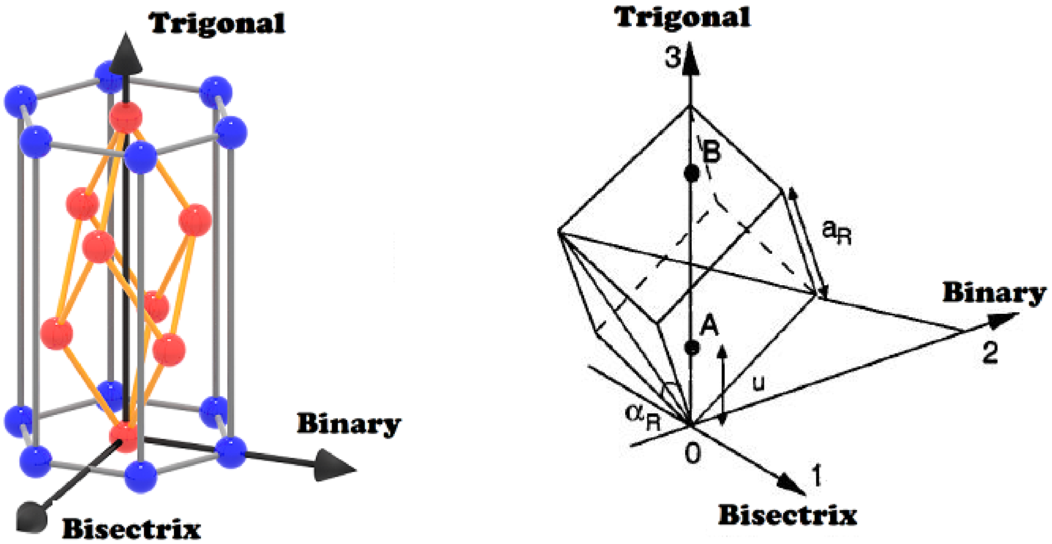

Figure 1-7: Rhombohedral Crystal Structure

The crystal parameters of pure bismuth and antimony at different temperatures are shown in Table. 1.4.1 [68]. Since bismuth and antimony have the same crystal

Table 1.1: Summary of the Crystal Parameters of Bismuth and Antimony at Different Temperatures

		Hexagonal			**Rhombohedral**		
	T(K)	a_H(Å)	c_H(Å)	c_H/a_H	a_R(Å)	α_R(°)	u
Bi	4.2	4.5330	11.797	2.6025	4.7236	57.350	0.23407
	78	4.5350	11.814	2.6051	4.7273	57.280	0.23400
	298	4.5460	11.862	2.6093	4.7458	57.230	0.23389
Sb	4.2	4.3007	11.222	2.6093	4.4898	57.233	0.23362
	78	4.3012	11.232	2.6114	4.4927	57.199	0.23364
	298	4.3084	11.274	2.6167	4.5067	57.110	0.23349

structures and similar lattice parameters, it is not surprising that Bi-Sb alloys could form a solid solution over the whole composition range while keeping the rhombohedral structure unchanged. Also as expected, the lattice parameters of Bi-Sb alloys are between those of pure bismuth and antimony. The lattice parameters will be reduced when increasing the antimony content in the alloy since Sb has a smaller lattice.

1.4.2 Electronic structure

Studies of the electronic band structure of bismuth and antimony have been reported by Dressselhaus [69] and Edelman [70], respectively. The explanation in this chapter will be mostly based on the summary from Lenoir, Scherrer and Caillat [67]. The bismuth and antimony lattice structure can be regarded as having a small distortion from the simple cubic lattice, which leads to the fact that bismuth and antimony are both semimetals characterized by a small overlap of the fifth and sixth bands. This resulted in the presence of a small equal number of electrons and holes at all temperature for ideal materials. Fig. 1-8 shows the Fermi surfaces of bismuth and antimony in the Brillouin zone with carrier pockets [67]. Where L points are for electrons, T and H points are for holes; axes 1, 2, 3 are parallel to the binary, bisectrix, and trigonal axes, respectively; ϕ_e and ϕ_t are the tilt angles of the electron and hole ellipsoids.

In bismuth, the highly anisotropic shape of electron quasi-ellipsoids pockets leads

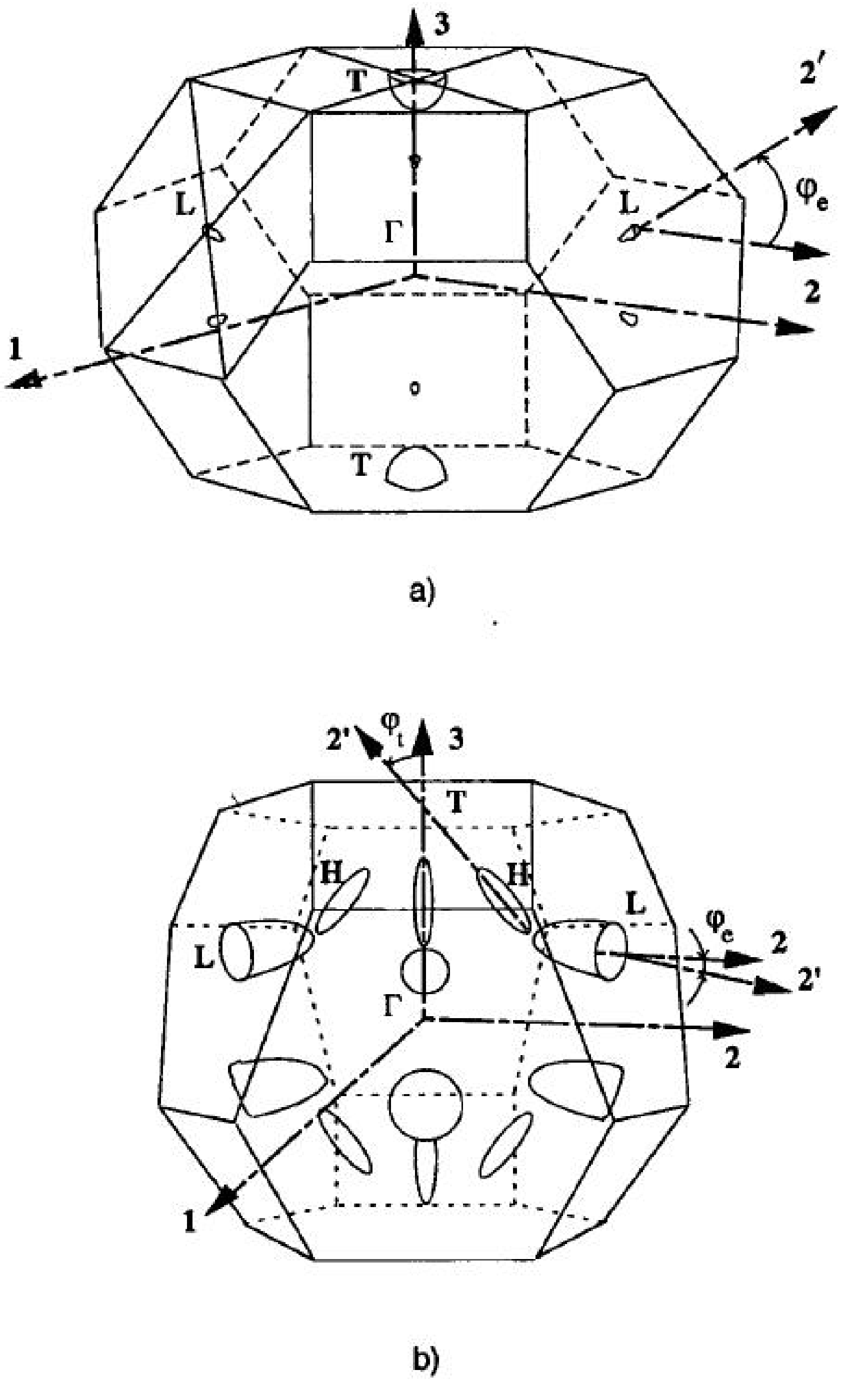

Figure 1-8: Fermi Surfaces of (a)Bismuth and (b)Antimony in the Brillouin Zone

Table 1.2: Band Parameters for Carriers in Bismuth and Antimony at 4.2K

Carriers	$m_{1'}$ (m_0 units)	$m_{2'}$ (m_0 units)	$m_{3'}$ (m_0 units)	E$_F$ (meV)	n=p 10^{17}	N$_v$
Bismuth						
L-electrons	0.00119	0.266	0.00228	27.2	2.7	3
T-holes	0.064	0.064	0.69	10.8	2.7	1
Antimony						
L-electrons	0.0093	1.14	0.088	93.1	374	3
H-holes	0.068	0.92	0.05	84.4	374	6

to unusually small effective masses along with two directions, resulting in very high electron mobility for bismuth and antimony semimetals(hundreds to thousands of times higher than ordinary metals). Similar structure occurs for the light L hole band, which is separated from the conduction band by a narrow energy gap E_g and coupled to it by the $\mathbf{k}\cdot\mathbf{p}$ interaction, causing a highly nonparabolic dispersion relationship of the two bands and a quasi-momentum dependence of the Bloch amplitude. Lax and Mavroides proposed the ellipsoidal non-parabolic (ENP) two-band model [71], which is the simplest dispersion relation for the L-bands. Expressed in the following form:

$$E\left(1+\frac{E}{E_{\mathrm{g}}}\right)=\frac{\hbar^2}{2m_0}\vec{k}\cdot\begin{pmatrix} m_{1'} & 0 & 0 \\ 0 & m_{2'} & 0 \\ 0 & 0 & m_{3'} \end{pmatrix}^{-1}\cdot\vec{k} \tag{1.21}$$

where E is the electron energy correspond to the bottom of the conduction band, m_0 is the free electron mass, m_i are the components of the effective mass tensor for electrons and L holes near the edges, $\vec{k}$ is the wave vector.

In antimony, as shown in Fig. 1-8 (b), the electron pockets are sitting at the L points in the Brillouin zone as well, and holes are located at six H points that are equivalent. Antimony deviates more from the cubic symmetry than bismuth, leading to a larger carrier density. Table 1.4.2 shows band parameters of effective mass tensor of bismuth and antimony [72]. It is important to note that the L, T and H hole bands differ greatly regard to the density of state effective mass m_d, which are equal to $m_{d,L} = 0.02m_0$, $m_{d,T} = 0.14m_0$, $m_{d,H} = 0.5m_0$, respectively.

1.4.3 Energy band and semi-conducting behavior

Both two elements contributed to the energy band structure of Bi-Sb alloys. In a bismuth rich Bi-Sb system, the substitution of Bi atoms by Sb atoms in the Bi lattice drastically modifies the band structure of bismuth.

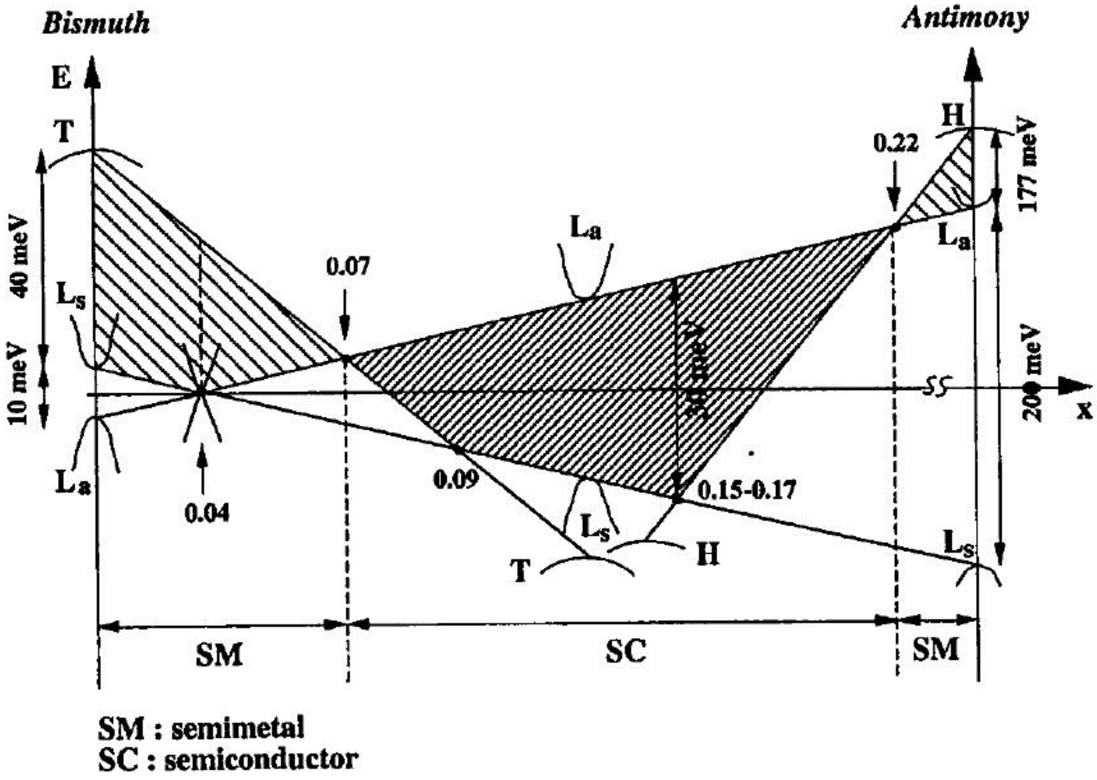

Figure 1-9: Schematic Diagram of Band Edge Configuration of $Bi_{1-x}Sb_x$ Alloys

Fig. 1-9 shows the band structure variations for $Bi_{1-x}Sb_x$ alloys as a function of Sb contents at low temperature (4.2K) [67]. These results were obtained from powerful quantum oscillatory effects such as magnetoreflection or cyclotron resonance. It can be seen that there are three band parameters affected by the alloying: (1) The overlap between L and T bands (2) The indirect engergy gap E_g (3) The energy of the top of the H bands.

The two ends of x-axis of Fig. 1-9 represent pure bismuth and antimony. The overlaps between conduction band L_s and valence band T shows clear semi-metal band structure of pure bismuth. The same structure also appears at x=1 for conduction band L_a and valence band H of pure antimony. However, it is important to note that the band position orders are inverted for bismuth and antimony. Therefore, when adding antimony atoms into bismuth, the bands start to move due to the alloying effect called the band inversion. In the range of $0 < x < 0.04$, the band order is still the same as in pure bismuth, but the overlap and the band gap keeps decreasing with x. At $x \approx 0.04$ a gapless state appears [73]. After this point, the bonding L_s band and antibonding L_a band are inverted and the gap increases with antimony concentration. At $x \approx 0.07$, the overlap between the conduction band L and valence band T disappears, the alloy lost its semimetallic attributes and becomes a semiconductor [74]. This semiconducting behavior will prevail with increasing Sb content up to $x \approx 0.22$, where the H band passes L band again restoring the semimetallic behabior [75]. Overall, between 7% to 22% antimony content, Bi-Sb alloys are narrow gap semiconductors with the maximum gap at around 15% Sb.

Since the gap is so small ($20meV$), it is not surprising that all the parameters that associated with energy band will have a strong temperature dependence. That is also one of the reasons why Bi-Sb could stand out at low temperature as a good thermoelectric material.

1.4.4 Phase diagram and segregation effect

Although bismuth and antimony share the same crystal structure and form solid solution together, their melting points are differed by hundreds of degrees, and there is a large gap between the liquidus and the solidus line for Bi-Sb alloy. Fig. 1-10 shows the phase diagram of Bi-Sb alloys [76]. The three phases: Liquid, Solid, Liquid + Solid are separated by the liquidus and solidus lines.

One could melt bismuth and antimony together into the liquid at composition **A**, and then starts to cool down to get solid Bi-Sb phase. However, based on the phase diagram, the composition could start varying in the Liquid + Solid. Due to the different solidification temperature, at 450°C, the liquid already starts solidification at composition **B**. This solid phase with higher antimony content will change the

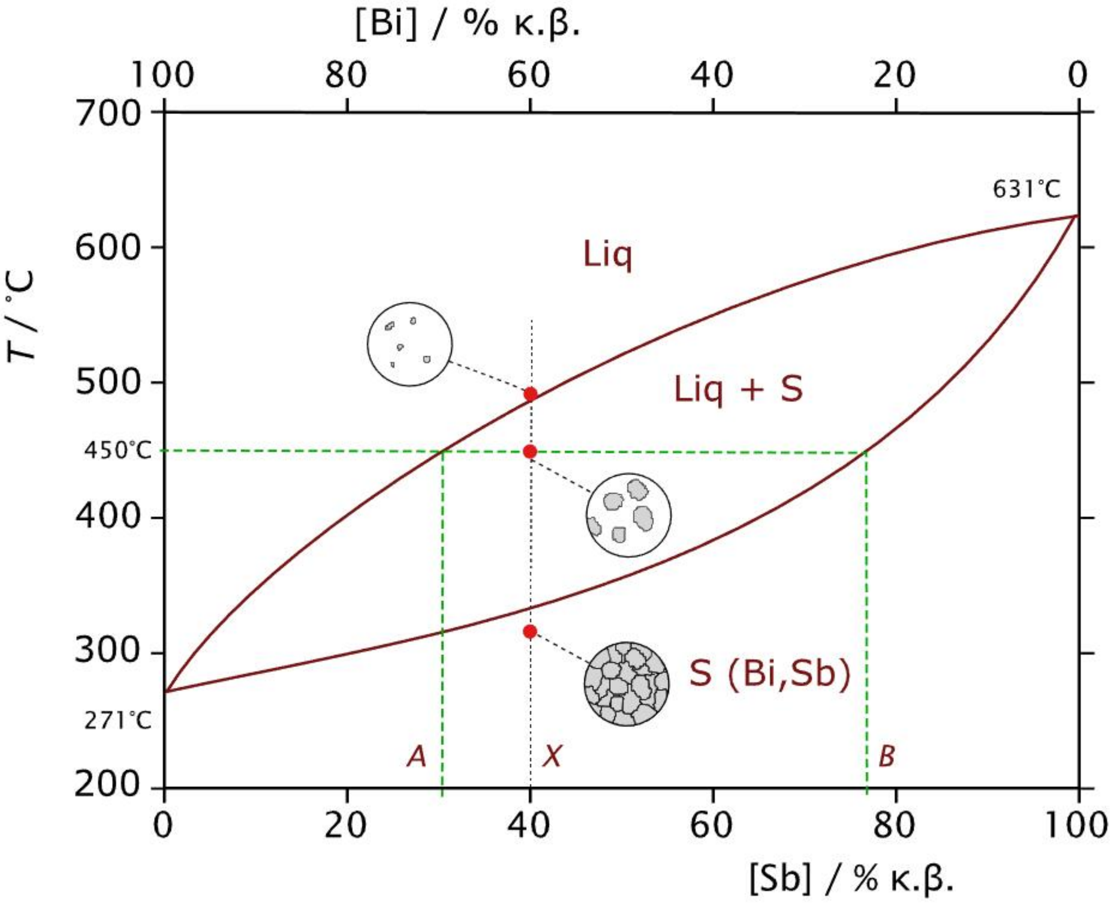

Figure 1-10: Phase Diagram of Bi-Sb Alloys

antimony concentration in the remaining liquid phase. As the temperature keeps decreasing, the system will follow the solidus line from composition **B** all the way down to very low antimony concentration. In the end, there will be a wide range of antimony concentration in the Bi-Sb solid solution. This is called the **segregation effect**. Based on Fig. 1-9, the energy gap is quite sensitive to Bi-Sb composition. Therefore, reducing the segregation effect to achieve homogeneous material is crucial in pursuing reproducible Bi-Sb alloys with high thermoelectric performance. One way to prepare a homogeneous sample is to maintain a constant composition through the synthesis process, such as rapid rate cooling or mechanical alloying. The other possible method is to apply additional procedures to homogenize the solid phase afterward, such as high temperature annealing. More details will be given in the experimental chapter.

1.4.5 Previous studies on Bi-Sb alloys

There have been several studies of thermoelectric properties on single crystal Bi-Sb since the 1960s [65, 66, 77–81]. In particular, Yim and Amith [79] investigated the temperature dependent properties of different single crystal Bi-Sb compositions along two crystalline axes (trigonal and binary/bisectrix axes in a rhombohedral A_7 structure of the space group $R_{\bar{3}m}$ as shown in Fig. 1-7. In its undoped state, Bi-Sb is an n-type semiconductor. Yim and Amith also investigated the magneto-thermoelectric effects which gave rise to enhancement of the Seebeck coefficient in magnetic fields. The effects were explained on the basis of the transverse-transverse thermo-galvanomagnetic effects which are the results of co-action between Hall effect, Nernst effect and Righi-Leduc effect. They reported ZT $\sim$ 0.55 along the trigonal axis of Bi-Sb in the absence of a magnetic field around 80K but only $\sim$ 0.44 along the binary/bisectrix axis peaked at 150K. By applying an external magnetic field of 3 kOe, ZT could increase to $\sim$ 1 along the trigonal axis. On the other hand, magneto-TE effect along the binary/bisectrix directions was not reported. After more than four decades, this high ZT remains the highest among cryogenic TE materials studied to date.

There are technical hurdles to overcome before the Bi-Sb alloy can be utilized as a practical material for cooling applications. A well-known drawback of a single crystal is its poor mechanical properties. In order to pursue more robust alloys, there were also efforts on synthesizing polycrystalline Bi-Sb [61, 82–85], Fig. 1-11 shows a simplified demonstration of polycrystalline materials, blocks represent the poly-grains with different crystal orientations. T, B1, B2 stands for Trigonal, Bisectrix, Binary, respectively. Due to the large temperature gap between the solidus and liquidus lines in the Bi-Sb phase diagram, significant phase segregation always occurs under normal cooling conditions, preventing the formation of a homogeneous alloy ingot upon cooling down from the liquid mixture phase. To overcome this issue, mechanical alloying was preferentially used by most researchers in improving the compositional

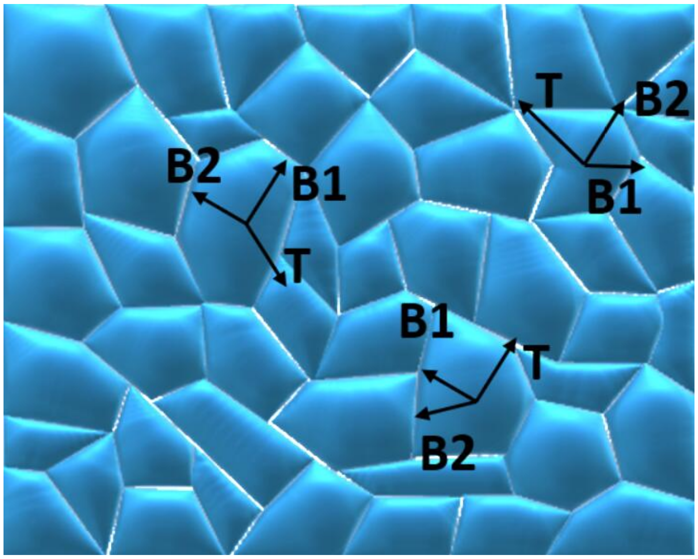

Figure 1-11: Schematic demonstration of polycrystalline Bi-Sb material

homogeneity of the samples [83, 84]. However, longtime high energy ball milling is prone to contamination, which could have adverse effects on the TE properties. Other attempts to accelerate the cooling process such as liquid-nitrogen quenching was also reported. However, the quenched ingots still required a time-consuming furnace annealing to homogenize afterward [82]. One group reported using melt-spinning for a higher cooling rate which showed unclear dependence on the synthesis condition, indicating that the TE properties might not be optimized [61].

Some groups also investigated doped p-type Bi-Sb alloys. Jin et al. studied the band structure of single crystal Bi-Sb, and proposed to help dope Sn into the H bands by increasing the Sb concentration in the Bi-Sb matrix [86]. In the end, ZT ∼ 0.13 was achieved at 250K with single crystal $Bi_{77.1}Sb_{22.9}Sn_{0.75}$ sample. On the other hand, Chen et al. prepared Pb doped polycrystalline $Bi_{84}Sb_{15}Pb_1$ using a mechanical alloying method and achieved ZT ∼ 0.12 at 190K [87]. After all, the TE properties of p-type Bi-Sb were still not competitive enough with the n-type counterparts.

Chapter 2

Experimental synthesis and characterization of Bi-Sb alloy

2.1 Overview: goals and difficulties

Based on the discussions in the first chapter, the key features of a better Bi-Sb alloy was rather clear. First of all is a high figure of merit ZT, which would require accurate manipulations on each thermoelectric parameters to optimize the properties. This requirement leads to the demand of controllable and reproducible sample preparation. Knowing the composition sensitivity of the energy gap from Fig. 1-9, it is important to be able to make a homogeneous sample with least composition fluctuations. However, from Fig. 1-10, the severe segregation effect became a significant obstacle in pursuing a uniform sample. Some experiments treatment have been applied to overcome this issue, each of them has its advantages and also shortages. Further details will be provided in the following sections of this chapter.

On the other hand, many previous works revealed the good thermoelectric properties of single crystal Bi-Sb alloys, especially along trigonal 33 direction. However, when it comes to the real industrial applications, there are technical hurdles to overcome before the Bi-Sb alloy can be utilized as a practical material for cooling applications. A well-known drawback of a single crystal is its poor mechanical properties. Therefore, the studies of polycrystalline bulk materials seem to be a more practical

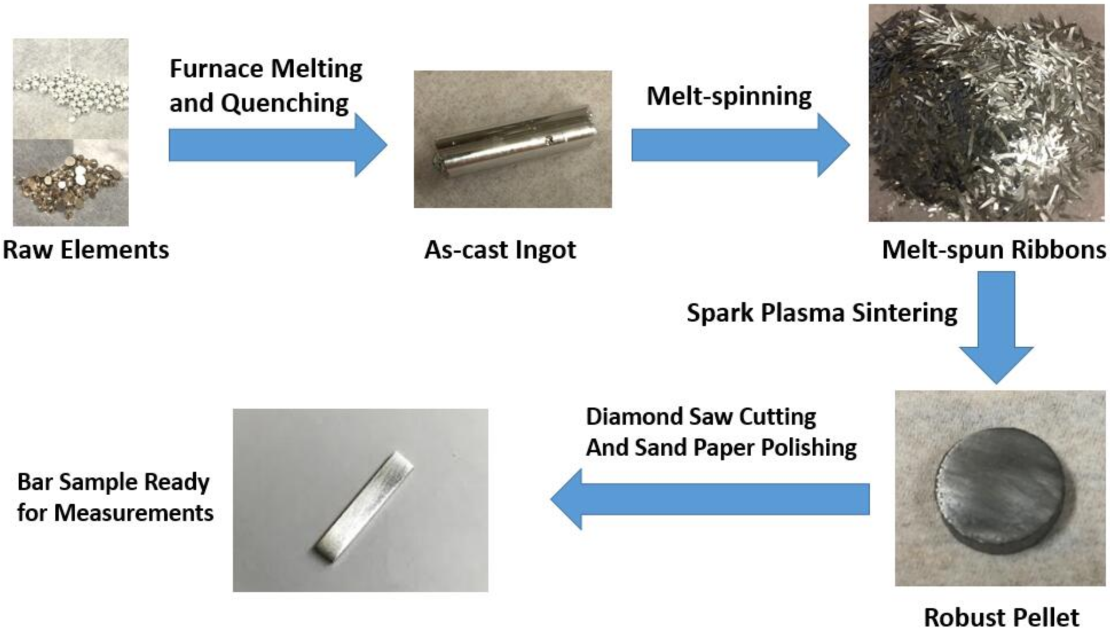

Figure 2-1: Experimental Synthesis of Bi-Sb Alloys

choice for the application, which also facilitate using different tools during synthesis for avoiding segregation effects.

Upon the polycrystalline preparation, the benefits of nanostructure cannot be neglect, which is also a hot topic for recent years. A good nano-structure has the potential to decrease the lattice thermal conductivity without damaging the original thermoelectric properties, which is precisely what we are looking for. Overall, achieving a high figure of merit ZT of homogeneous polycrystalline Bi-Sb alloys with robust mechanical properties is our final goal. There are several experimental techniques can be used to approach it. We also need to overcome the possible difficulties in front of us first.

Fig 2-1 showed all the procedures of the preparation of a Bi-Sb alloy sample. Each experimental step will be discussed in details in the following sections.

2.2 Vacuum systems

Both bismuth and antimony are easy to be oxidized forming bismuth oxides and antimony oxides, which are ceramic materials losing almost all the electrical transport abilities. So it is essential to minimize the oxidization during the whole preparation process. Bismuth and antimony oxidize slowly in the air at room temperature, and we can quickly burn out the oxygen attached to the material by melting the material at high temperature(> 1000°C) to break the chemical bonds. However, in the temperature range between 200°C to 800°C, where is just the region we will be focusing on to prepare the alloy, the oxidization could be quite severe. Therefore, it is very crucial to have all the heating and melting process happen under suitable vacuum environments.

The vacuum systems are applied for almost all the devices involved in the preparation and measurements of Bi-Sb alloys. Including the sealed quartz tube for mixed bismuth and antimony chunks, the melt-spinning(MS) chamber, the ball-milling(BM) jar, the spark plasma sintering(SPS) chamber, the glove box, the ZEM system chamber, the Versalabs and Physical Properties Measurements System(PPMS) chamber, every vacuum system is enclosed by compact walls with a lid at the entrance. There is usually an O-ring between the lid and the chamber with vacuum gel on the surface to fully minimize the chance of oxygen sneaking in. The creation of a vacuum system was usually fulfilled by a mechanical pump, which can pump the system down to under 10 mTorr. Fig. 2-2 shows a typical mechanical pump used in our vacuum systems, which pumps out the gas in the system relying on a high-speed rotary vane.

To further lower down the oxygen concentration in the environments, it requires an advanced pump with different mechanisms. Our quartz tube sealing system has a diffusion pump installed, which use a high-speed jet of oil vapor to direct gas molecules in the pump throat down into the bottom of the pump and out the exhaust, as shown in Fig. 2-3 [88]. The diffusion pump could effectively lower the pressure down to under 10^{-4} mTorr. Another type of pump used for low-temperature vacuum chamber is the cryopump, which traps gases and vapors by condensing them on a cold surface.

Figure 2-2: Typical Mechanical Pump Used in Our Lab

The cryopumps provided fast and clean pumping down to 1 to 10^{-6} mTorr using compressed helium in the Versalab and PPMS chamber.

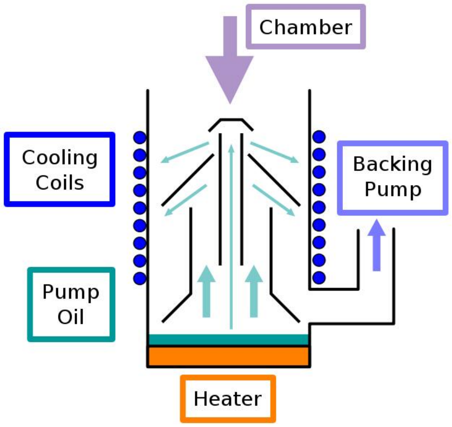

Figure 2-3: Demonstration of Diffusion Pump

2.3 Furnace melting and quenching

The Bi-Sb alloys synthesis starts with fresh elements pieces with the purity of 99.999%. Fig. 2-4 shows the most commonly used elements pieces bought from the vendor(Sigma Aldrich and Alfa Aesar), Ge, Sn and Pb here were used as p-type dopants, which will be discussed later. For n-type Bi-Sb alloys, randomly mixed bismuth and antimony pieces were sealed into a vacuum quartz tube and placed carefully in a heating furnace. The furnace has a digital temperature control that provides accurate and slow temperature adjustment up to 1100°C. The heating was performed by a couple of resistor coils around the chamber, and temperatures were monitored by a thermal couple sitting at the center of the chamber. One end of the quartz tube was about 2 cm higher than the other, leads to an angle of about 10° to 15° to the horizontal direction. This set-up allowed all the liquid to flow to one end of the quartz tube and react there without losing materials. Usually, the randomly mixed bismuth and antimony pieces were melted at 800°C for 1 hour. To ensure a uniform liquid, there were also 2 to 3 times of twisting and shaking of the quartz tube at 800°C by holding one end with the clamp. When having dopants with higher melting point such as Ge or Ni in the quartz tube, the process temperature would be increased to 875°C and heating time might extend to 3 hours.

After the 1 hour annealing at 800°C in the liquid phase, the quartz tube was quenched into liquid nitrogen for fast cooling, which is one of the key factors to reduce the segregation effect discussed in the last chapter. Once the uniform solution was cooled from liquid state rapidly, the atoms did not have enough time to diffuse out and segregate, therefore the homogeneous status will be captured into the solid phase. Experiments showed that using iced water as a quenching bath could provide similar results as using liquid nitrogen. Even though the temperature difference was larger using liquid nitrogen, but the formation of nitrogen gas layer between the hot quartz tube and liquid nitrogen bath reduced the quenching efficiency, resulted in about 100-200 °C/s rate for the temperature change. And once the quenching is finished, the as-cast ingot of Bi-Sb alloy was obtained.

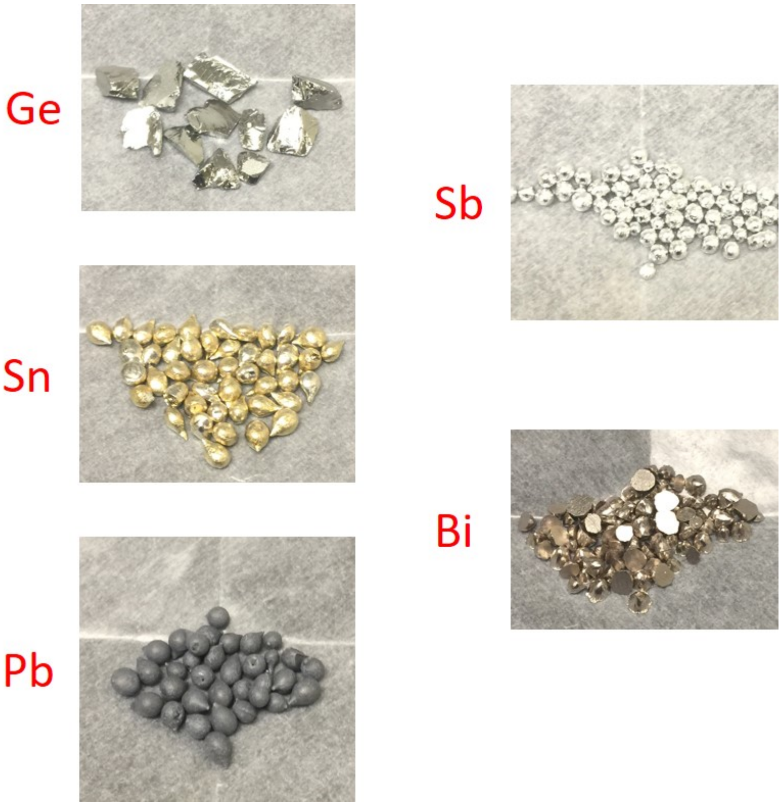

Figure 2-4: Photos of Fresh Elements Pieces

2.4 Melt-spinning system

In the early stages of this project, we had been directly pulverizing the as-quenched Bi-Sb ingot into small pieces, then re-compress into a robust disk by spark plasma sintering system. Later on, to further improve the sample properties, the melt-spinning system was introduced. Melt-spinning is a technique used to provide rapid cooling for liquid metals. The cooling rate achievable by melt-spinning is on the order of 10^4âĂŞ10^7 kelvins per second [89]. The process was demonstrated in Fig. 2-5 [90].

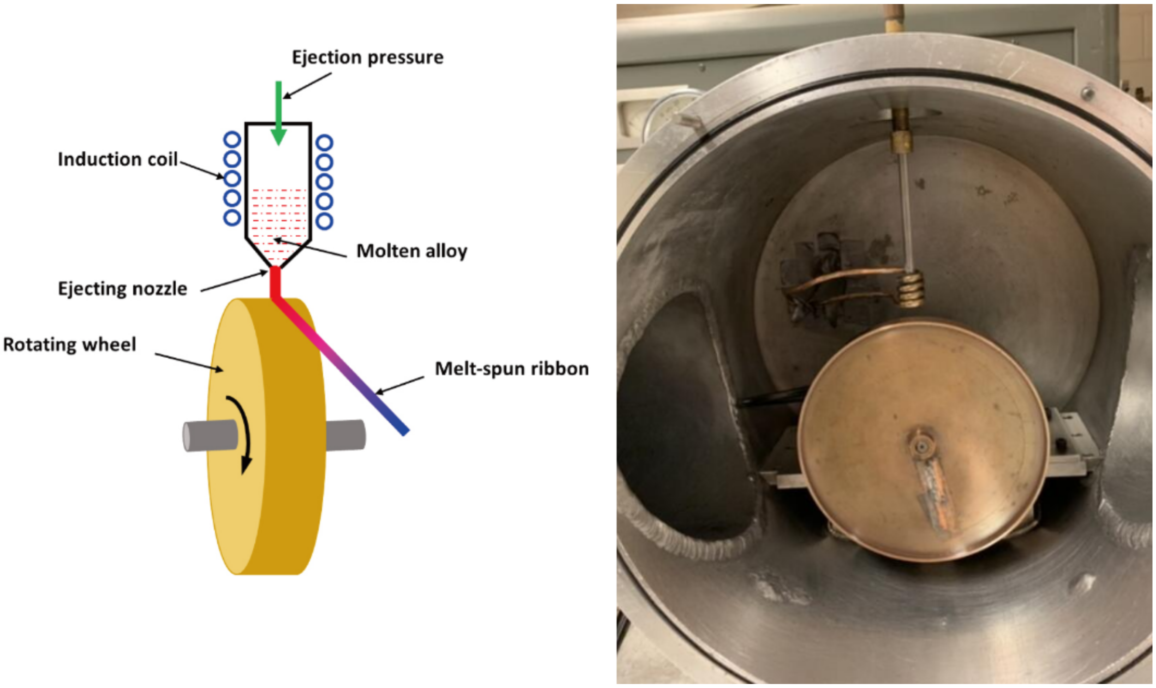

Figure 2-5: Melt-Spinning Process

Metal pieces were placed in a quartz tube fixed inside an induction coil, there is a small ejecting nozzle at the bottom of the quartz tube pointing to a big copper wheel which is usually internally cooled by water. The whole system was placed in a vacuum chamber to prevent oxidization. Once the process began, the copper wheel would start to spin at 1500 to 4000 revolutions per minute (rpm). There would be a high-frequency alternating current go through the induction coil to activate an alternating electromagnetic field in the metal pieces, which lead to large Eddy currents that melted the metal pieces inside the quartz tube. Once all the metals became liquid, an ejection pressure generated by an argon gas flow would be applied from the top of the liquid. Therefore the metal liquid would shoot out from the nozzle onto the rotating copper wheel. Due to the high thermal conductivity of copper, the metal liquid would be solidified as long as it touched the wheel and then thrown out along the wheel surface due to the high-speed rotation. In the end, long and thin melt-spun ribbons were formed, as shown in Fig. 2-6.

By using the melt-spinning technique, the solidification process happened in milliseconds, which gave almost no time for the Bi-Sb liquid segregate in the liquid + solid phase, immediately freeze down the uniform distribution in the liquid phase. At the same time, due to the short solidification time, the growth of the Bi-Sb crystal grain was also limited. This resulted in the formation of nano-grain structure leading to a lower lattice thermal conductivity from the increased phonon scattering. In the end, the thermoelectric figure of merit ZT was benefited.

Figure 2-6: Melt-Spun Ribbons from Melt-Spinning Process

2.5 Ball-milling system

Besides the melt-spinning technique, another method to create nano-structure and avoid segregation effect is the ball-milling method. Ball-milling is a kind of mechanical alloying, that relies on the high energy collisions between balls and materials in a sealed jar, as shown in Fig. 2-7 [91]. Typical jar and balls are usually made of stainless steel, which is also what we have been using in our experiments. There are also ones made of tungsten carbide or agate stones to satisfy a higher hardness demand and also avoid the iron contamination.

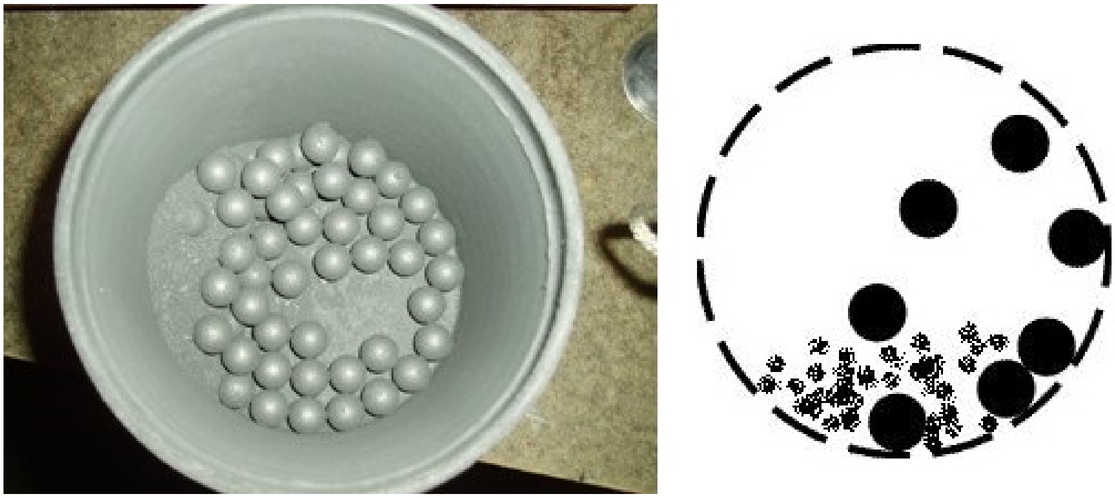

Figure 2-7: Jar and Balls for Ball-Milling

Figure 2-8: Ball-Milling Machine

The balls and materials usually were sealed with argon in the jar by operating in the glove box to reduce the oxidization. Later on, the sealed jar will be placed in a ball-mill machine which can provide high speed shaking with thousands of revolutions per minute shown in Fig. 2-8. During this process, the balls would keep hitting the materials with high energy, which kept breaking the grains into a smaller size. At the same time, the energies could also be used to build chemical bonds, which made it possible to obtain Bi-Sb alloys without going through the liquid-solid phase transition. In the case, the segregation effects could be avoided from the origin.

However, in real experiments with Bi-Sb systems, the results were not as good as we discussed for the ideal cases. First of all both bismuth and antimony are soft materials that showed ductile behavior under forces. Therefore it was not easy to break them into nano-grains by simple collisions. On the other hand, with the limitation of glove box vacuum condition and stainless steel container, it was not easy to eliminate the contaminations of iron and oxygen. Both references and our results showed negative effects on the thermoelectric properties of Bi-Sb systems. Above are the reasons why we chose the melt-spinning process for our preparation of Bi-Sb nanobulk, but the ball-milling technique still had its successes in many different material applications.

2.6 Spark plasma sintering system

In the old days, the preparation of a robust disk for cutting and measurements usually relied on cold press at room temperature followed by longtime annealing in the furnace. In recent years, as the spark plasma sintering (SPS) system being invented, the whole process became much more simplified and effective. With SPS system it is possible to apply internal heat and external pressure at the same time. Someone claimed the mechanism of the spark plasma sintering is still unclear therefore the process name pulsed electric current sintering (PECS) should be considered as more correct [92]. However commercially the name SPS (spark plasma sintering) is more common. Anyways, it is a sintering technique utilizing uniaxial force and a pulsed (on-off) direct electrical current (DC) under low atmospheric pressure to perform high-speed consolidation of the powder, as shown in Fig. 2-9 [93].

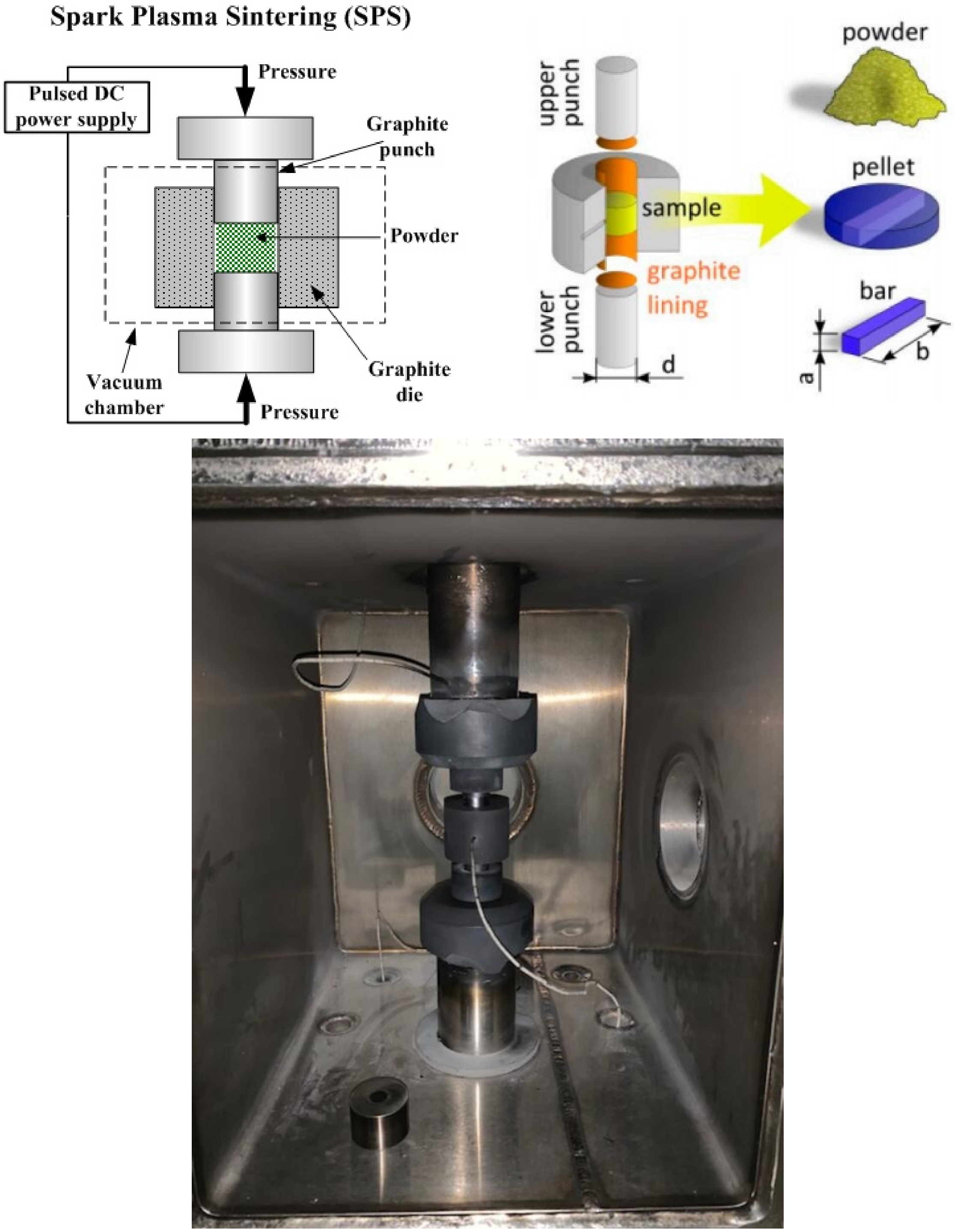

Figure 2-9: Spark Plasma Sintering (SPS) System

The powders of target materials were placed in a graphite(or tungsten carbide for high-pressure treatments) die with two punches pressing from both top and bottom.

The device allows us to design time-dependent programs for the applied temperature and pressures up to thousands of °C and 1 GPa. Once the program started, a massive current up to thousands of amperes would direct went through the powder inside the die. The spark plasma sintering process proceeds through three stages: Plasma heating, Joule heating and Plastic deformation. Each stage further improved the connection and diffusion between particles, and increased the density of the system by combining powders into a solid pellet. SPS system could provide fast sintering process with low particle growth, which made it possible to retain nano-structure while homogenizing the system.

The experiments conditions might be varied for different runs, a typical program for undoped n-type Bi-Sb sample is applying 50MPa at 240°C for 15 mins. A pre-high-pressure low-temperature method was also invented to help incorporate dopants like Pb, Ge with very low solubility, this method used a program as following: 500MPa pre-compress for 10 mins at room temperature, then followed by 50MPa compress at lower temperature 150°C for 5mins, marked as Pre HP-LT. The idea was as following: For example, the Ge dopants were melted with Bi-Sb together, if the system was cooled down slowly, then almost all the Ge will be separated out from Bi-Sb due to the 0 solubility. In our experiments, the rapid cooling rate in the melt-spinning process made it possible to capture all the Ge atoms into the melt-spun ribbons before they were rejected. However, if the same 240°C annealing temperature was still used in the SPS process, then part of the Ge atoms would still diffuse out. The reason could be the high atom activity since it was close to the melting point of this system(275°C). Therefore, using 150 °C as the annealing temperature could significantly reduce the diffusion movement of Ge atoms, and 500MPa pre-compress made it possible to obtain a robust disk at that low temperature.

The labels in the legends for SPS conditions used in the experiments are listed in Table. 2.1:

Table 2.1: Labels for SPS Conditions Used in the Experiments

Legend Labels	**SPS Conditions**
SPS (No special notes)	240°C 50MPa for 15 mins
SPS Pre HP-LT	RT 500MPa for 10 mins then 150°C 50MPa 5 mins
SPS Post HP	240°C 50MPa for 15 mins then RT 500MPa 2 hours
SPS HP Deformed	240°C 50MPa for 15 mins then RT 600MPa 30 mins without constrain on sides

2.7 Cutting and polishing

The SPSed disk was in a cylinder shape and surrounded by graphite foils. In order to perform different types of characterizations and measurements, the disk usually needed to be cut and polished into a cuboid bar.

The cutting process was done by a slow diamond saw, as shown in Fig. 2-10. The sample was mounted on a flat surface of a steel bar with super glue, then the steel bar would be fixed above the diamond saw. The cutting positions were precisely determined by a micrometer, and the different rotation speeds and weights could provide different cutting solutions. Once the cutting was done, the sample will be cleaned using ultra-sound wave in acetone.

The last step before measurements is polishing. The polish was performed with sandpapers of different grit levels. Low-level rough sandpapers were always used first, and then slowly increase the grit level of sandpapers one by one, up to 4000 grit. Since Bi-Sb alloys are very soft, therefore it is possible to even reshape the sample by just using hand and rough sandpapers. In the end, the bar sample will have metallic luster on the smoothed surfaces. A typical sample dimension for PPMS thermoelectric measurements is 1.2mm x 2.5mm x 12mm.

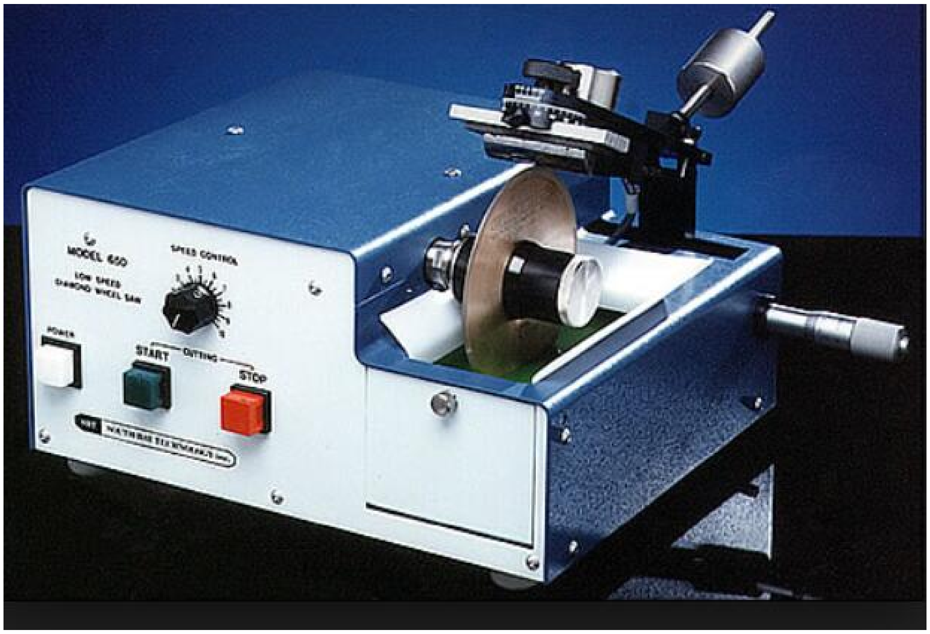

Figure 2-10: Typical Slow Diamond Saw

2.8 Physical properties measurement system

Physical properties measurement system (PPMS) from Quantum Design, is one of the most standard measurement systems for low-temperature thermal transport measurements. This system also has various modules than can be installed to perform many different measurements, such as electrical transport option (ETO), vibrating sample magnetometer (VSM) etc. In our case, we mainly used the thermal transport option (TTO) for resistivity and Seebeck coefficient measurements. It can also provide measurements for thermal conductivity, but considering the heat loss issue due to the large metal contacts thermal capacity in the usual thermal conductivity measurements, we chose a better method called the hot disk method, which will be discussed in the thermal conductivity section. Fig. 2-11 showed the appearance of the PPMS in our lab.

The system contains a large cylinder chamber with all the sensors and a superconductive magnet inside. The control panels are stored in a separate cabinet and connected to a computer. This system requires liquid helium in the chamber to

Figure 2-11: Physical Properties Measurement System

cool down the temperature and active the superconductive magnet and cryopump. Samples will be placed in a sample puck and insert into the chamber from the top entrance.

2.8.1 Contacts preparation

As shown in Fig. 2-12, the measurements require three copper leads on the sample. One lead at the very end of the sample was connected to the heater, and two more copper leads were placed in the middle connected to the thermometers to measure both voltage and temperature. The temperatures were read by comparing the resistance of the thermistor of on the thermometer with a pre-calibrated curve. There was silver epoxy in between of the copper leads and sample, to ensure a good electrical and thermal contact between the sensor and the sample. There was no copper lead on the other end, the sample was directly inserted into the clamp on the puck, having good contact with the cold sink. Since the space on the puck was limited, therefore there was a restriction of the sample dimensions.

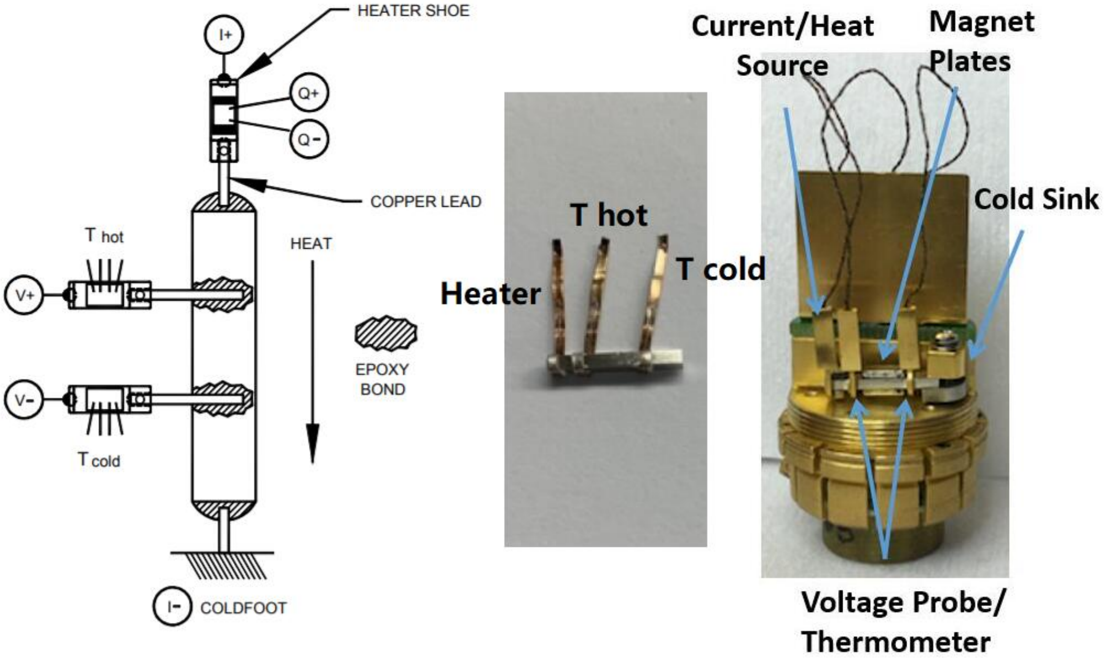

Figure 2-12: Samples with Contacts Leads for PPMS Measurements

2.8.2 Thermoelectric measurements

The **resistivity** measurements were finished using a four-point method. The system drives current from one end through the whole sample to the other end. The voltage and temperature was read by the two thermometers in the middle. With the large resistors on the thermometers, there will be almost no current split into the middle lead, therefore the effect from the contact resistance could be minimized. This method could be used to precisely measure very small resistance.

The **Seebeck coefficient** was measured using the same leads. The system drives a current through the resistor on the heater to raise the temperature of one end of the sample, which the other end was having good contact with the cold sink. Therefore, a uniform thermal gradient was formed across the whole sample. By reading the voltages and temperature difference simultaneously from the two leads in the middle, the Seebeck coefficient could be calculated based on the definition.

The resistivity and Seebeck coefficient measurements were calibrated and checked by the standard Ni sample to make sure there is no significant system errors involved

Figure 2-13: Versalab System

either from the contact resistance or additional heat capacitance of the copper leads. Independent measurements were also performed on the Versalab system and ZEM system which all had different type of contacts. The results from the different system on the same sample showed good agreements which indicates that the effects from different types of contacts were negligible.

2.9 Versalab system

Versalab system is another low-temperature measurement system from Quantum Design, as shown in Fig. 2-13. It is very similar to PPMS, but with an air compressor installed. Therefore the helium used in the system could be recycled by the compressor, no refilling of liquid helium required. It also has many different modules, which could be used for electrical transport, thermal transport and magnetic properties measurements. In our project, the Versalab was mainly used to perform low-temperature measurements of resistivity and Hall coefficient measurements.

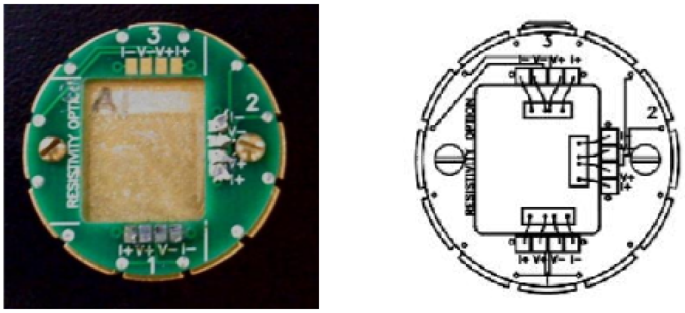

Figure 2-14: Sample Puck of Versalab System

2.9.1 Contacts preparation

Fig. 2-14 shows the sample puck of Versalab system. There are three channels on each puck that can provide measurements for three samples at the same time. Each channel has four electrodes connected to the sample by fine indium wires. The four electrodes are in the order of current(-), voltage(-), voltage(+), current(+). The sample needs to be fixed on the flat surface by insulating double-sided tape. The sample should be narrow, thin and long to reduce the measurement uncertainty caused by the geometry.

2.9.2 Electrical transport measurements

The **resistivity** measurements were performed in a similar four points method as in PPMS. The pre-set current came in from the current(+) lead and went through the sample and left from the current(-) lead. The two votalge leads read the voltage without affecting the current flow in the sample. Therefore, an accurate resistivity measurement could be finished on low resistance system.

The **Hall coefficient** measurements were performed using Van der pauw method. Therefore the samples were cut and polished into very thin square plates($< 0.3mm$), and the four leads will be connected to each corner, as shown in Fig. 2-15. An perpendicular strong magnetic field was applied across the sample plane, deflected the current to form a Hall voltage.

Based on a single band approximation, the Hall voltages could be related to the

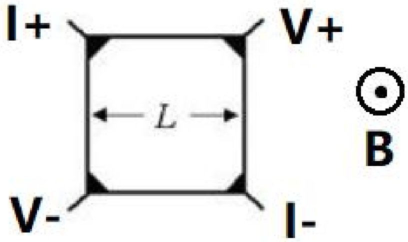

Figure 2-15: Van der Pauw method

carrier concentration by the following equation:

$$V_H = \frac{IB}{qnt} \tag{2.1}$$

where V_H is the Hall voltage, I is the driven current, B is the strength of the magnetic field, q is the unit charge, n is the carrier concentration and t is the thickness of the sample plate.

It is worth noticing that the Hall voltage is independent of the side length of the sample plates.

Chapter 3

Measurements results and discussion

3.1 Phases and micro-structure

3.1.1 X-ray diffraction

X-ray diffraction patterns were checked for both n-type Bi-Sb alloys and doped p-type Bi-Sb alloys. All the samples showed a single rhombohedral A_7 structure of space group $R_{\bar{3}}m$, including the doped p-type Bi-Sb alloys. In the followings are some selected XRD patterns:

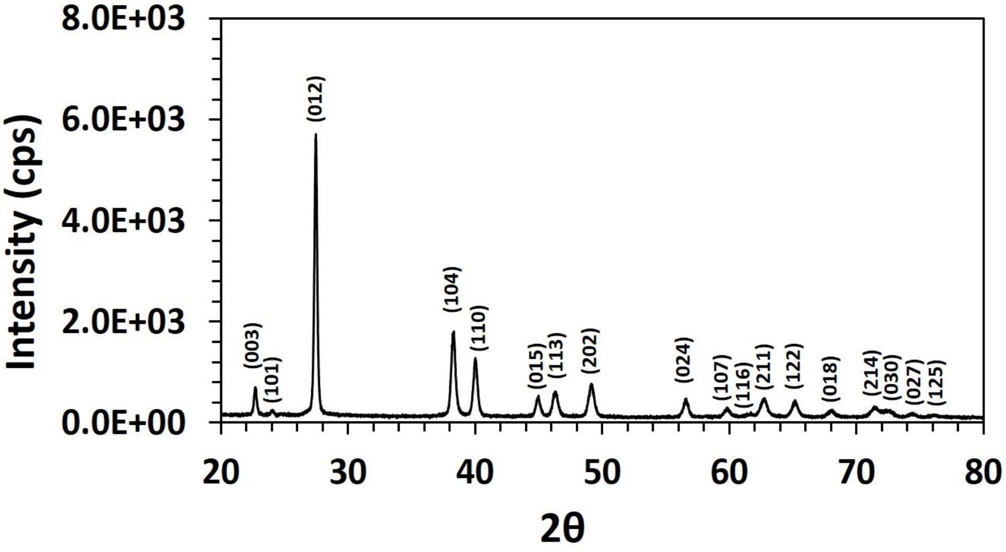

Figure 3-1: X-Ray Diffraction Pattern of Undoped $Bi_{85}Sb_{15}$ As-Quenched + SPS

Fig. 3-1 showed the X-ray diffraction pattern of undoped $Bi_{85}Sb_{15}$ SPS disk made with as-quenched ingots, which means there was no melt-spinning process involved. If there is no extra note, then it means the SPS conidtion was 240°C, 50MPa for 15mins.

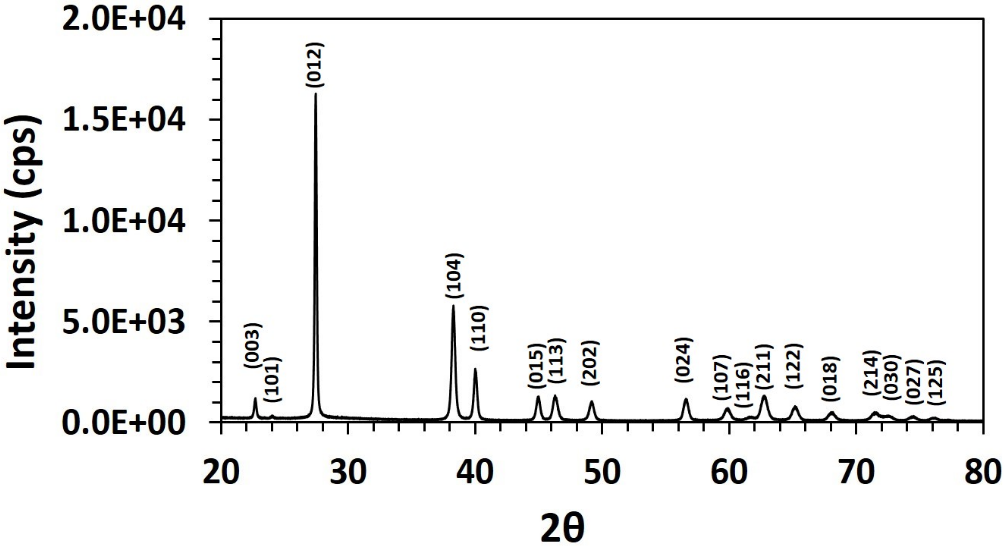

Figure 3-2: X-Ray Diffraction Pattern of Undoped $Bi_{85}Sb_{15}$ MS + SPS

Fig. 3-2 showed the X-ray diffraction pattern of undoped $Bi_{85}Sb_{15}$ SPS disk made thorugh melting and quenching + melt-spinning + SPS, which is the most common procedure used in this projects.

Fig. 3-3 showed the X-ray diffraction pattern of n-type doped $Bi_{85}Sb_{15}Pt_1$ SPS disk made thorugh melting and quenching + melt-spinning + SPS. Also showed pure single phase, no peaks of Pt detected.

Fig. 3-4 showed the X-ray diffraction pattern of p-type $Bi_{85}Sb_{15}Ge_{10}$, as discussed before, we used the pre-high-pressure low-temperature SPS program to incorporate the Ge atom into the Bi-Sb solid solution, marked as SPS Pre HP-LT. The condition was 500MPa pre-compress for 10 mins at room temperature, then followed by 50MPa compress at 150°C for 5mins.

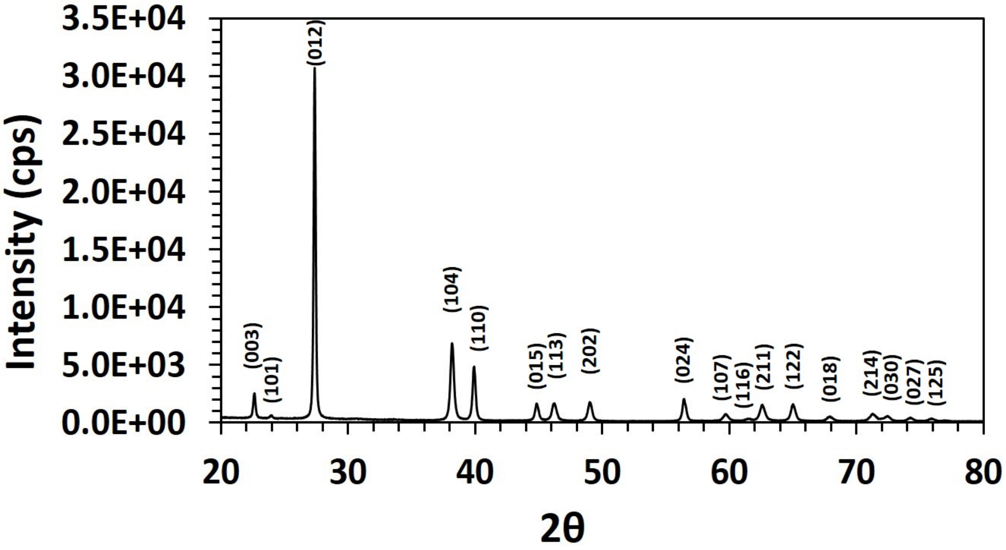

Figure 3-3: X-Ray Diffraction Pattern of Undoped $Bi_{85}Sb_{15}Pt_1$ MS + SPS

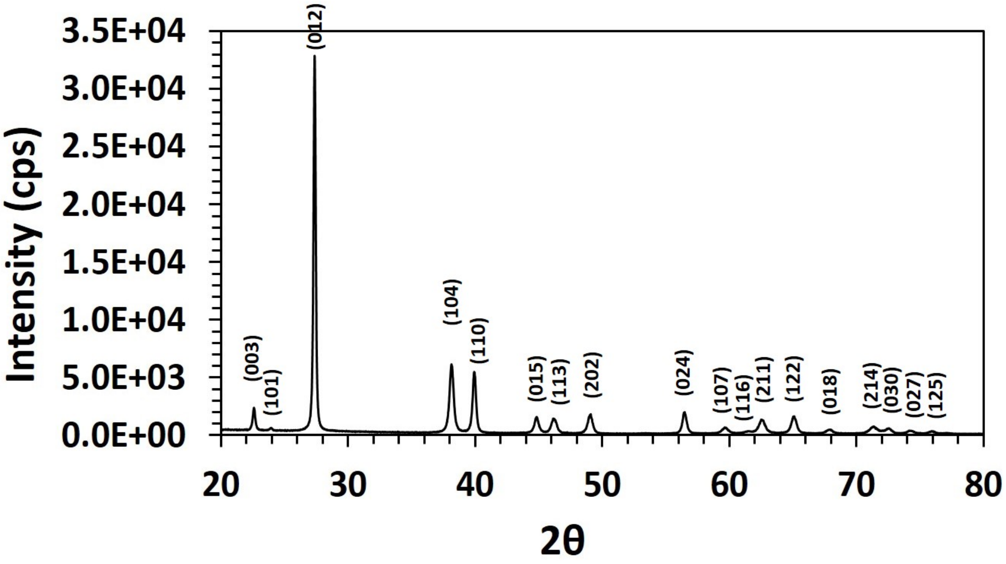

Figure 3-4: X-Ray Diffraction Pattern of Undoped $Bi_{85}Sb_{15}Ge_{10}$ MS + SPS Pre HP-LT

3.1.2 Scan electronic microscope

Scan electronic microscope (SEM) was used to observe the micro structure inside the Bi-Sb samples, the images were taken at the broken intersection of SPSed disks. Both samples made from as-cast ingots and melt-spun ribbons were investigated to show the difference after melt-spinning process.

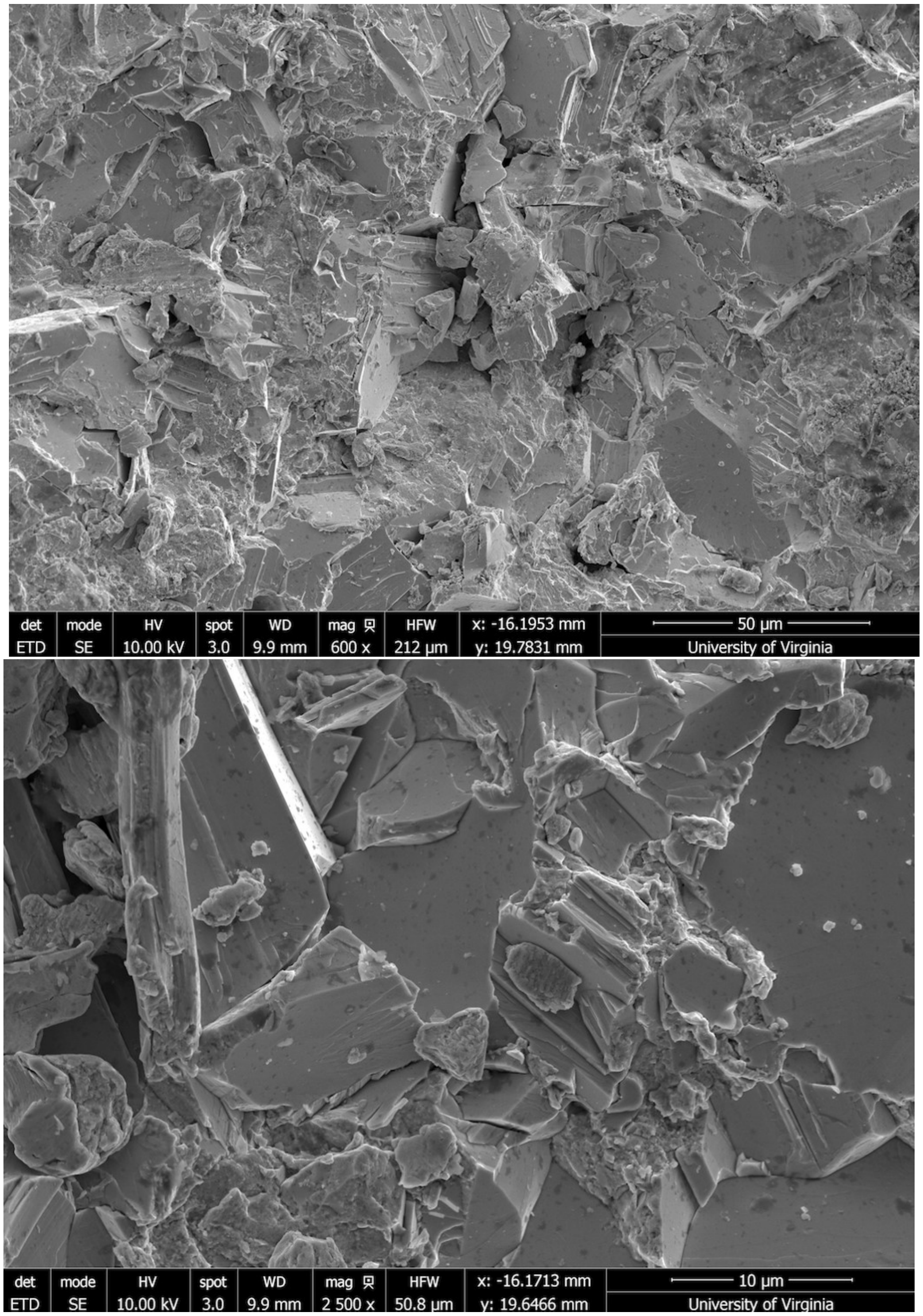

Figure 3-5: SEM Image of Undoped $Bi_{85}Sb_{15}$ As-Quenched + SPS

Fig. 3-5 showed the SEM images of undoped $Bi_{85}Sb_{15}$ made from as-cast ingots in different scales. Larger grains with layer structure can be observed, the grain size for these larger grains is around tens to hundreds microns. Several small grains might be created from the liquid nitrogen quenching also can be found.

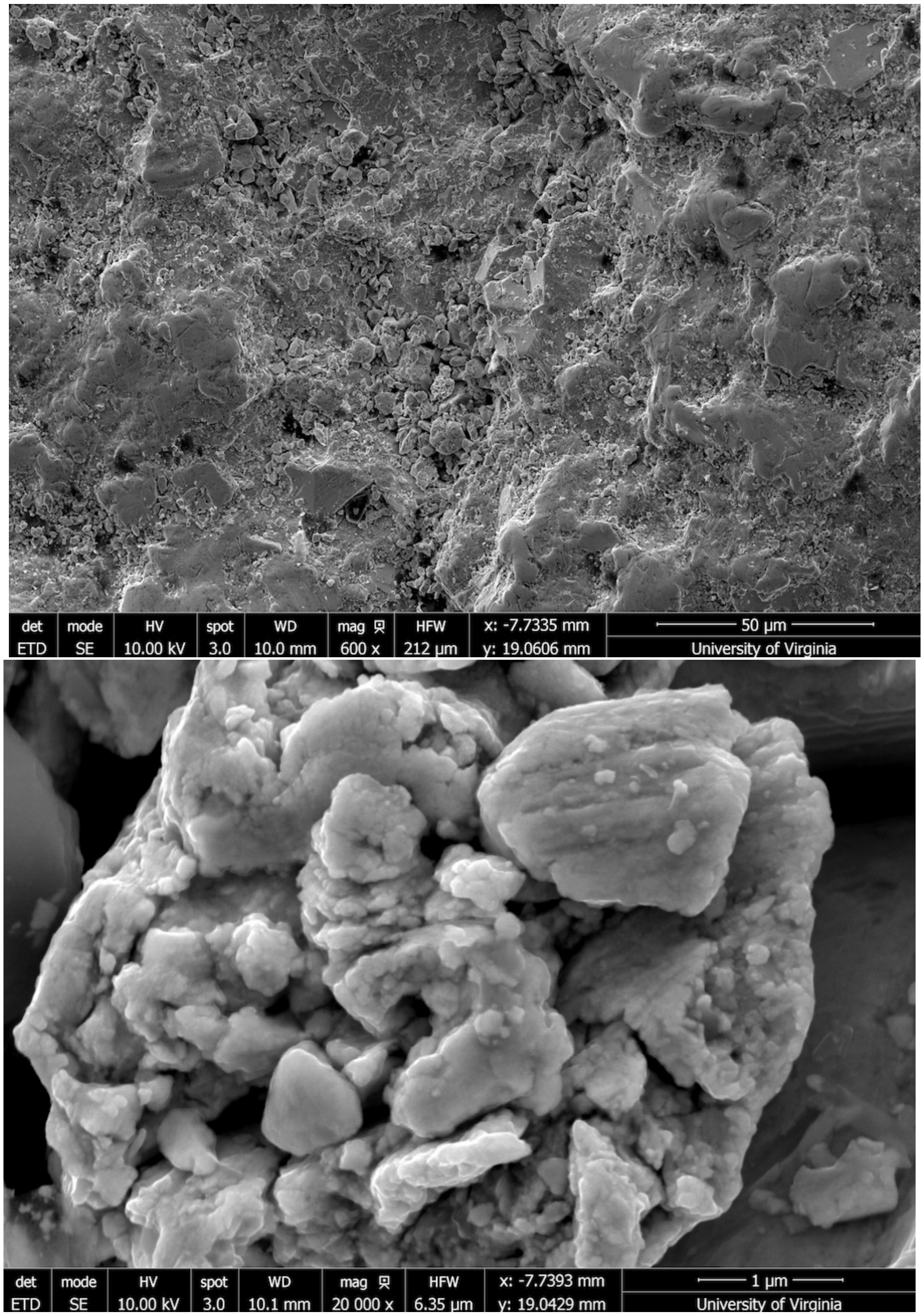

Figure 3-6: SEM Image of Undoped $Bi_{85}Sb_{15}$ As-Quenched + MS + SPS

Fig. 3-6 showed the SEM images of undoped $Bi_{85}Sb_{15}$ made from melt-spun ribbons in different scales. Finer structure with smaller grains can be seen compared with the as-cast sample in Fig. 3-5. By zooming in to the fractured surface, nano-size grain can be found inside the particles. A statistical method was used to determine the grain szie.

Areas with clear view of grains were selected from Fig. 3-6 (b), and processed by the image software to reveal the size of the grain, example was shown in Fig. 3-7

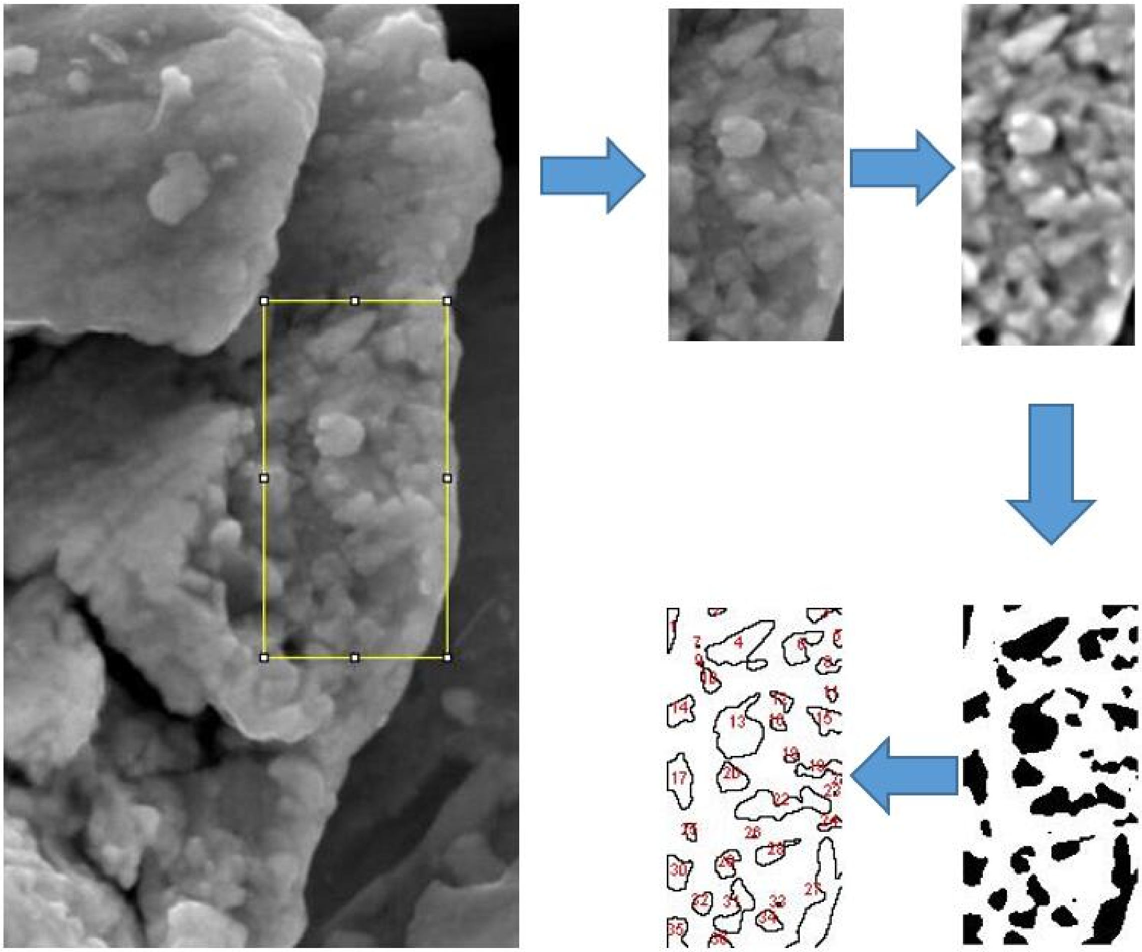

Figure 3-7: Grain Size Determination Process of $Bi_{85}Sb_{15}$ As-Quenched + MS + SPS

There were 10 different areas were studied using this method, and the grain size histogram plot was given in Fig. 3-8, the coordinates of the x axis represents the interval that less than each number and larger than the left number. For example, 80 nm with around 16% means that there were around 16% grain sizes within the range of 60nm to 80nm. As we can see, most grains sizes are within 10 to 100 nm. The

average grain size of all the grains studied through this process is **68.8 nm**.

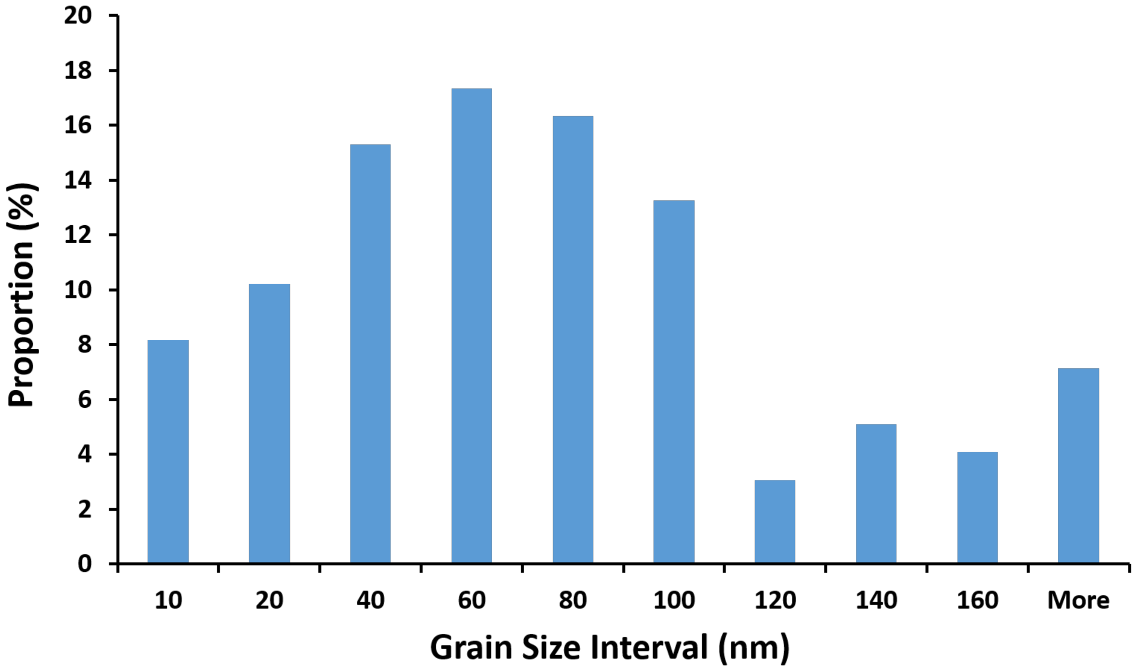

Figure 3-8: Grain Size Distribution of $Bi_{85}Sb_{15}$ As-Quenched + MS + SPS

Rapid solidification significantly impeded the grain growth, resulting in the nanobulk system. Some grains were seen to cluster together possibly due to the particle coarsening effect during high-temperature sintering. The high density of grain boundaries can effectively scatter the phonons that dramatically reduced the lattice thermal conductivity as observed.

3.1.3 EDS

SEM based Energy-dispersive X-ray spectroscopy (EDS) was used to check the homogeneity of the samples. Atoms density mapping of different elements were produced for both n-type and p-type samples, the density of the colored dots in a certain area represented the density of the atoms in this area for the corresponding elements. Therefore, a uniform distribution of Bi or Sb atoms density mapping indicated a homogeneous sample.

Fig. 3-9 showed the comparison for Sb EDS mapping of undoped $Bi_{85}Sb_{15}$ between (1)As-quenched ingot (2)Solid disk after further melt-spinning and spark plasma sintering. Brighter areas with more green dots indicated a higher concentration of antimony content in that area. Concentrations at different randomly selected spots were measured: points A-G correspond to 30%, 3%, 15%, 8%, 14.6%, 15.5%, 15% Sb respectively. In Fig. 3-9 (1), the as-quenched ingot was measured, obvious inhomogeneous distribution was found even after a liquid nitrogen quenching which means serious phase segregation could occur in seconds, causing a large concentration difference up to nearly 30% at different spots. Fig. 3-9 (2) shows the Sb concentration distribution for the final sample after melt-spinning and spark plasma sintering. A much smaller range of Sb concentration variation, under 1 at.% Sb, was observed, indicating an effective homogenization was achieved through rapid cooling by melt-spinning.

Another important point that worth addressing is the oxygen content in the sample. Fig. 3-10 shows the oxygen percentage of $Bi_{85}Sb_{15}$ without the MS process. Around 5% of oxygen was reported in different areas. However, it is worth mentioning that our EDS equipment has an oxygen background signal, so there could always be a 3-5% oxygen background detected in the measurements, and the number showed in Fig. 3-10 may not be accurate. Anyways it can be said that the oxygen content will not exceed the given value.

Fig. 3-11 showed the oxygen contents in melt-spun + SPS samples. As shown in the figure, after more processes involved, slightly more oxygen contents were introduced into the system. This can be expected considering the vacuum used in the experiments were around 10 mTorrs and the processing temperatures are relatively high. Higher level pumps may be required to provide better vacuum environments for reducing the oxygen contents.

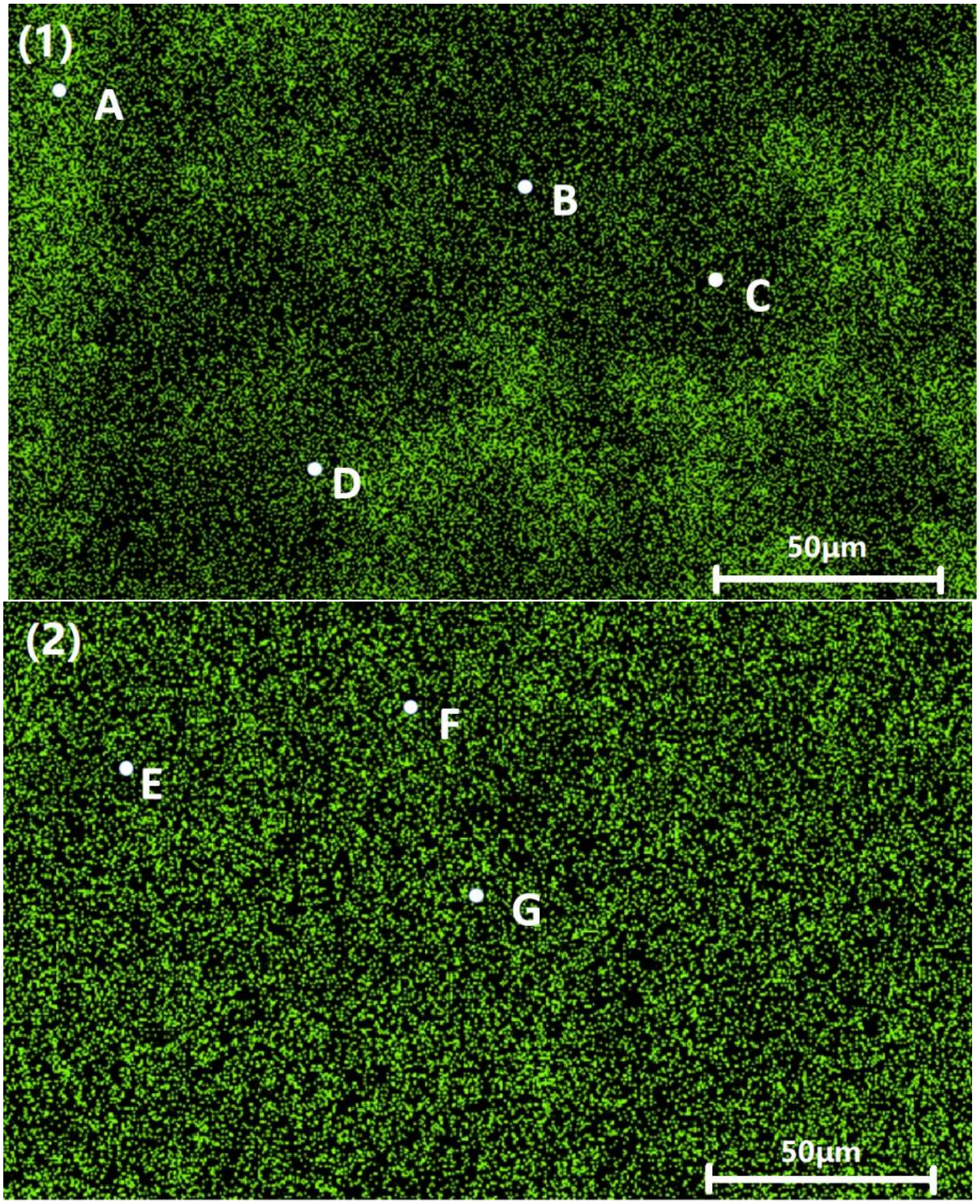

Figure 3-9: Antimony EDS Mapping of Undoped $Bi_{85}Sb_{15}$

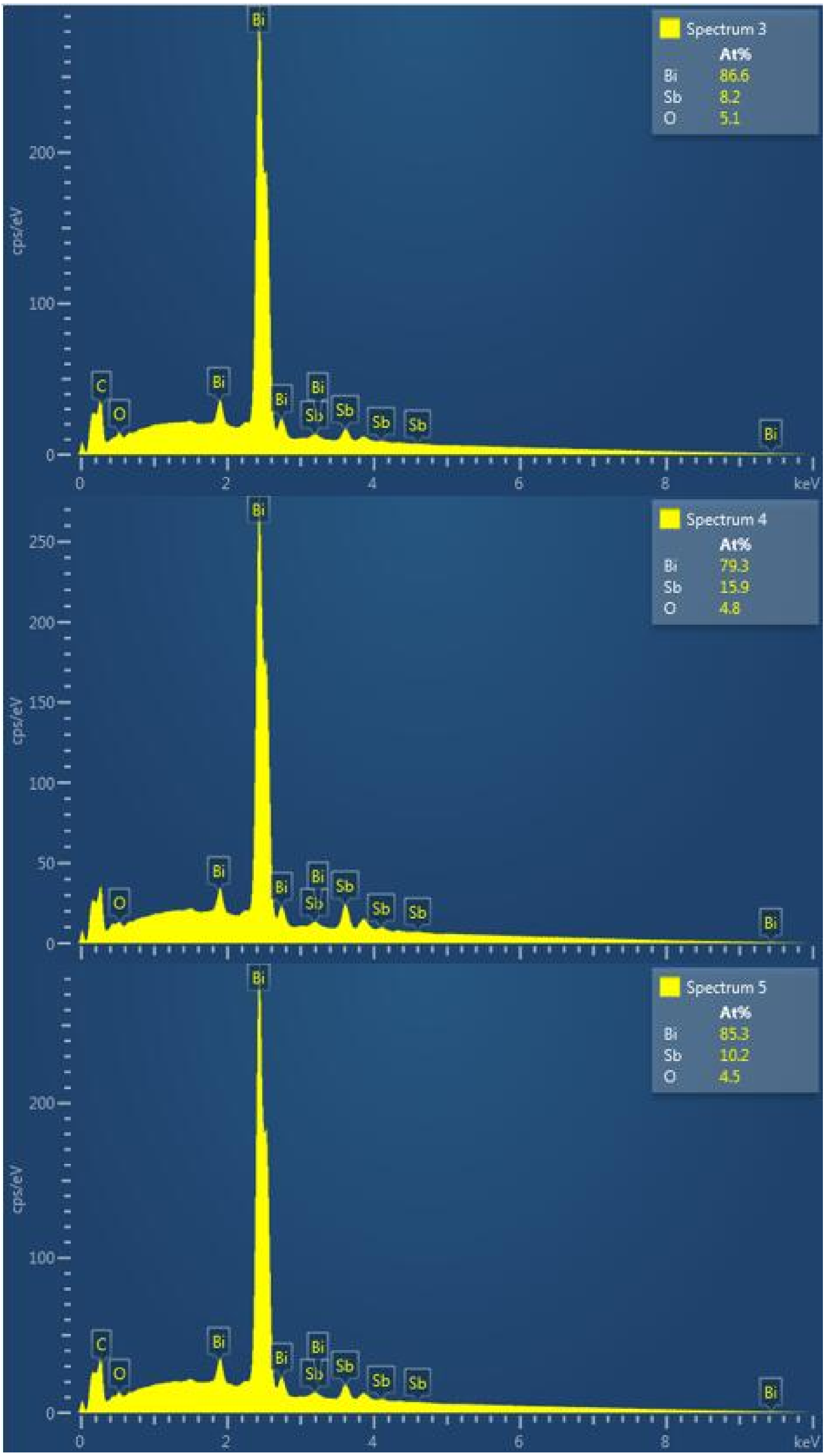

Figure 3-10: Oxygen Content in As-cast $Bi_{85}Sb_{15}$

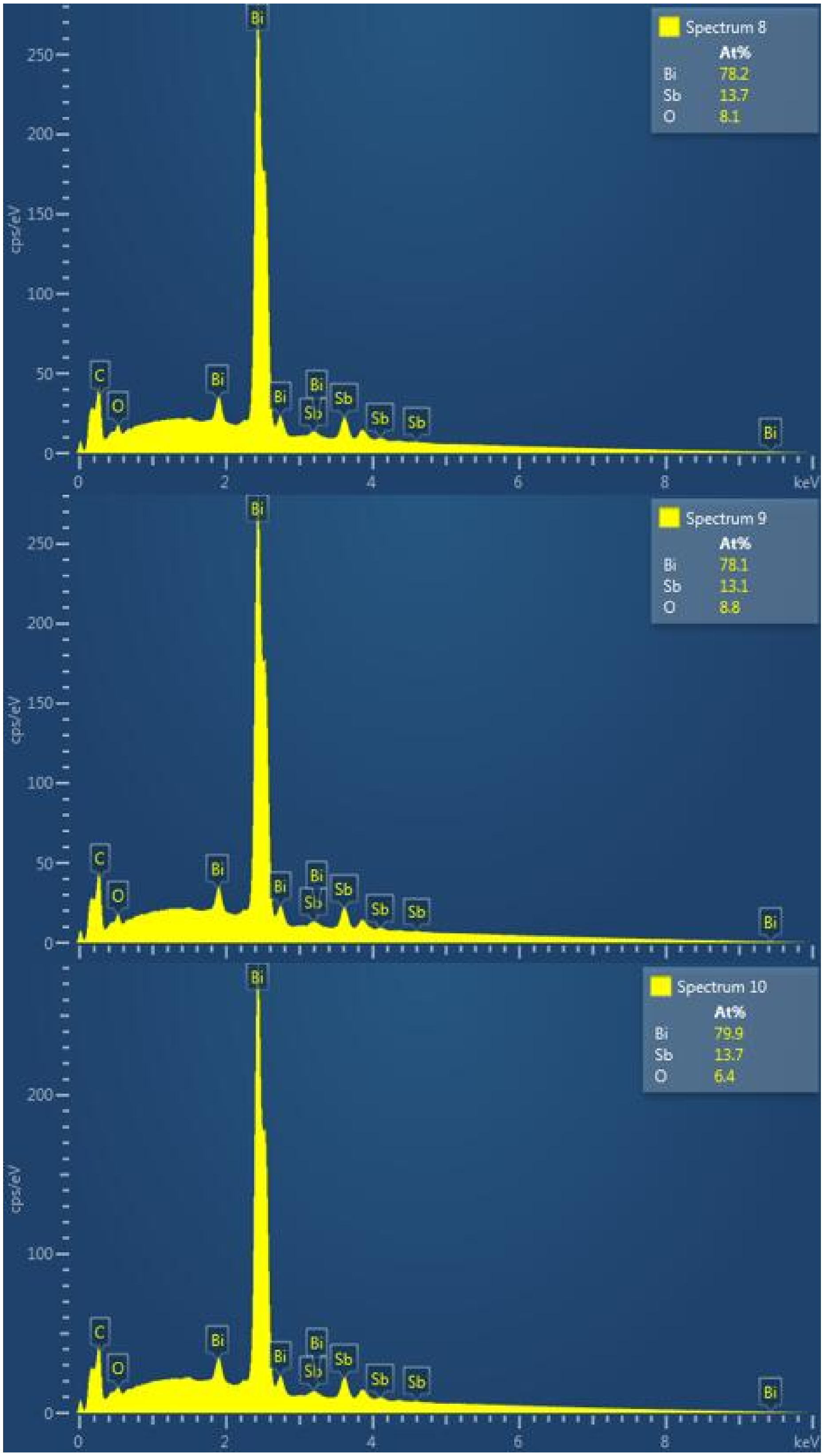

Figure 3-11: Oxygen Content in $Bi_{85}Sb_{15}$ MS + SPS

Fig. 3-12 Showed the EDS mappings for all the four elements Bi, Sb, Ni, Pb separately for p-type doped $Bi_{85}Sb_{15}Ni_1Pb_{0.5}$ sample. This sample was made through the melt-spinning method and used pre-high-pressure low-temperature (Pre HP-LT) method to be compressed in SPS. All the elements showed uniform distribution, no segregation or clustering detected, indicating all the dopants, Ni and Pb, were fully incorporated into Bi-Sb system.

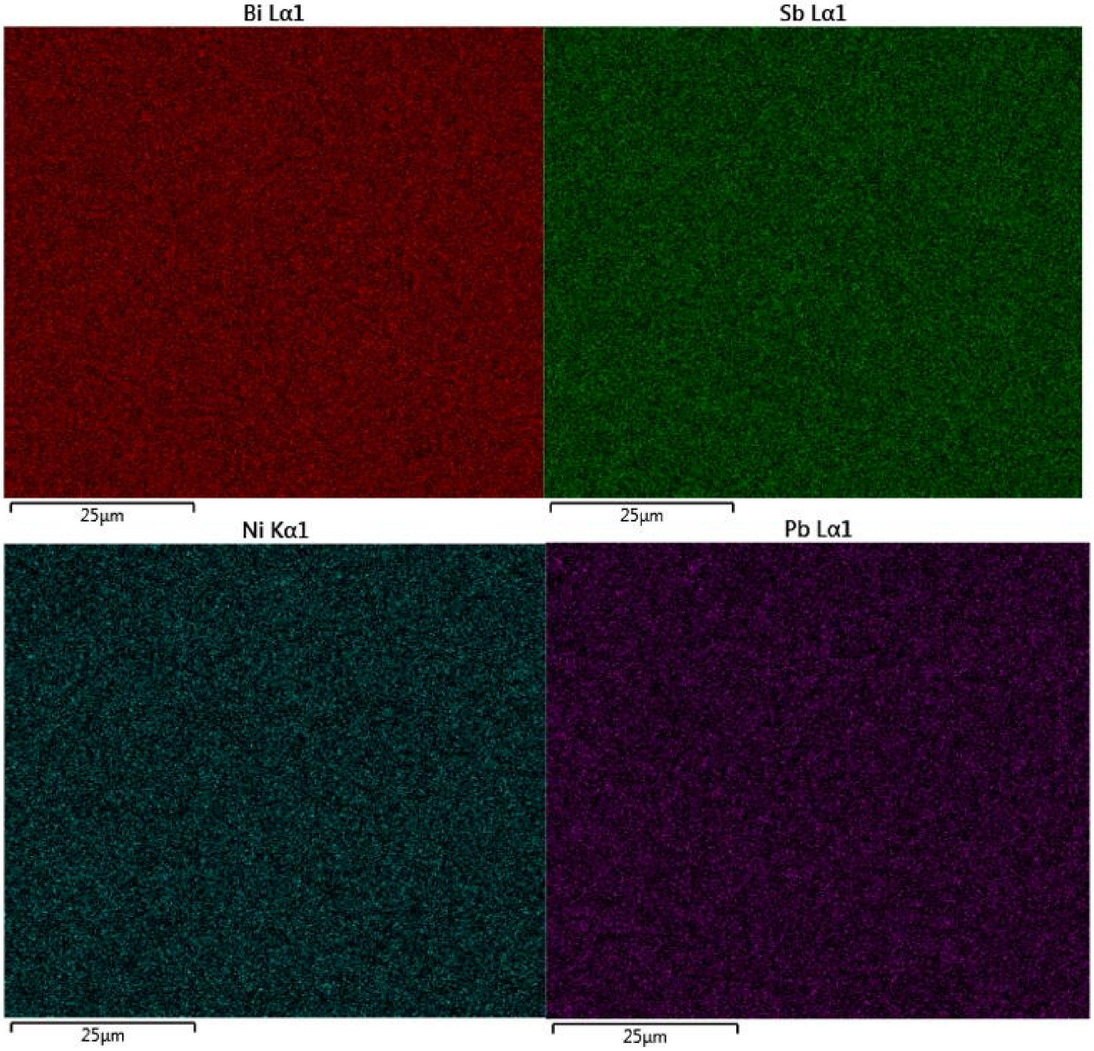

Figure 3-12: EDS Mappings of P-type $Bi_{85}Sb_{15}Ni_1Pb_{0.5}$ MS + SPS Pre HP-LT

Fig. 3-13 Showed the EDS mappings for Bi, Sb and Ge separately for p-type doped $Bi_{85}Sb_{15}Ge_{15}$ sample. This sample was made through the melt-spinning method and used Pre HP-LT method to be compressed in SPS. All the elements showed uniform distribution, no segregation or clustering detected. Knowing that Ge would not dissolve in Bi or Sb at all, it is quite impressive to be able to uniformly alloy up to 13% Ge into Bi-Sb system without affecting the crystal structure. This could be seen as a proof of the effectiveness of using MS + SPS Pre HP-LT on heavy doping of insoluble dopants.

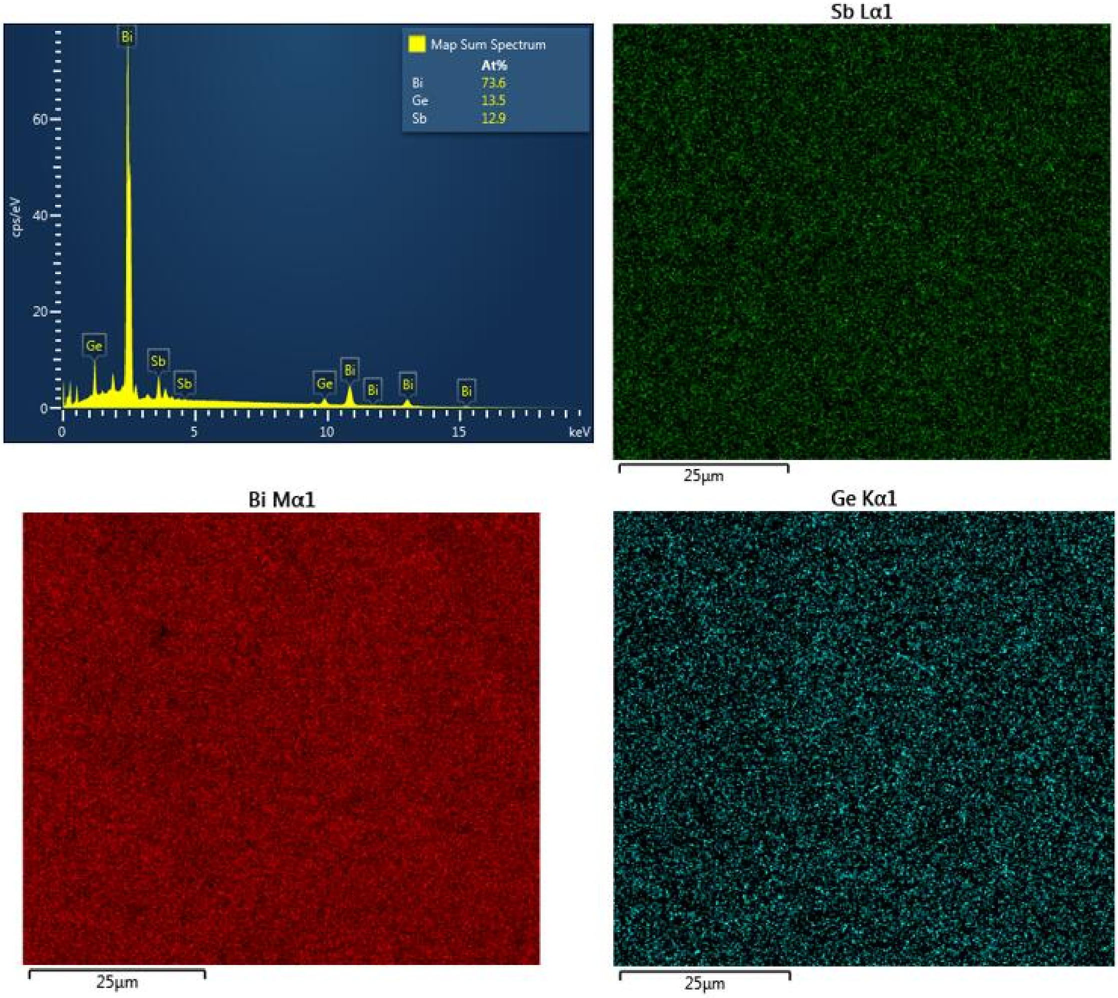

Figure 3-13: EDS Mappings of P-type $Bi_{85}Sb_{15}Ge_{15}$ MS + SPS Pre HP-LT

3.2 Thermoelectric measurements of n-type Bi-Sb alloys

The thermoelectric measurements include measurements of the resistivity, the Seebeck coefficient, and the thermal conductivity. Due to the complexity of thermal conductivity measurement, it will be discussed in a separate section later on. In this section, we will mainly focus on the n-type Bi-Sb alloys. The results will be split into different groups based on different features for both resistivity and Seebeck coefficient in the following subsections. The labels in the legends for SPS conditions used in the experiments were listed in Table. 3.1:

Table 3.1: Labels for SPS Conditions Used in the Experiments

Legend Labels	**SPS Conditions**
SPS (No special notes)	240°C 50MPa for 15 mins
SPS Pre HP-LT	RT 500MPa for 10 mins then 150°C 50MPa 5 mins
SPS Post HP	240°C 50MPa for 15 mins then RT 500MPa 2 hours
SPS HP Deformed	240°C 50MPa for 15 mins then RT 600MPa 30 mins without constrain on sides

3.2.1 Hall measurements

Hall coefficient measurements were performed on n-type Bi-Sb alloys using the Versalab system. With Eq. 3.1, the measured hall coefficients were converted into carrier concentrations under a single channel approximation, as shown in Fig. 3-14.

$$R_H = \frac{V_H t}{IB} = -\frac{1}{ne} \tag{3.1}$$

where R_H is the Hall coefficient, V_H is the Hall voltage and n is the carrier concentration.

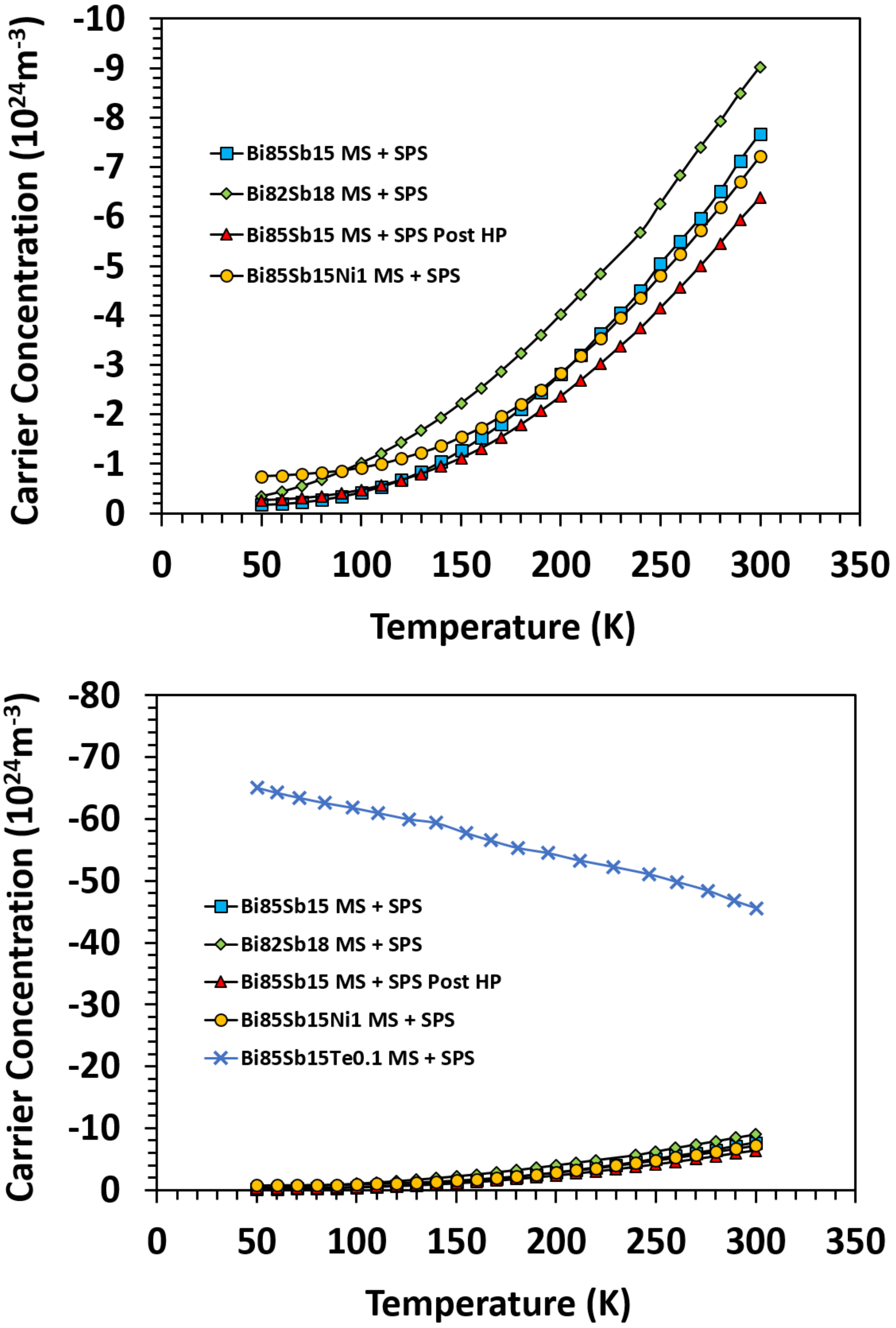

Figure 3-14: Carrier Concentrations of Different N-type Bi-Sb alloys

From the carrier concentration plots, we could see a relatively low carrier concentration with the magnitude of 10^{24} for undoped n-type $Bi^{85}Sb^{15}$ MS + SPS sample, which is about 10^2 to 10^4 times smaller than a typical value in metals. This indicates the low resistivity found in Bi-Sb system is contributed by the unusually high carrier mobilities. The $Bi^{82}Sb^{18}$ MS + SPS sample showed faster increasing of carrier concentration with temperature, indicating a smaller energy gap so that the electrons are easier to be activated. It is consistent with the band structure discussed before in Fig. 1-9. On the other hand, the post HP sample showed the opposite result, which may due to a band gap increase from the strain generated in high-pressure treatments.

The 1% Ni-doped sample showed slightly increased carrier concentration under 100K, where the intrinsic excitation was very small and the impurity carrier concentrations dominated. Considering the total amount of electrons that 1% Ni could donate, this small increase in carrier concentration also indicated the Ni was no an effective dopant. However, in the second plot, with only 0.1% Te doped, a very significant increase in carrier concentration was found, this more than 10 times change revealed the strong doping effectiveness of Te in Bi-Sb system.

3.2.2 Variation of compositions

Fig. 3-15 showed the thermoelectric properties of $Bi_{100-x}Sb_x$ with different compositions. This was a study finished at the early stage of this research project, therefore the sample was prepared using the as-cast + SPS method (hand grind the quenched ingots and then SPS), no melt-spinning was involved. Based on the energy gap plot Fig. 1-9, Sb 7% and Sb 21% would lead to a much smaller band gap compared with 12% and 15%. This will result in a more metallic behavior since the electrons are easier to be excited into the conduction band. In Fig. **??** 7% Sb and 21% Sb showed a lower resistivity and Seebeck coefficient as expected. The reason why they still have a decent Seebeck coefficient with almost 0 gap is the composition uncertainty due to the inhomogeneous sample without MS, there would be a distribution of compositions, and the 7% Sb and 21%Sb are average concentrations. On the other hand, the 15% Sb and 12% Sb showed quite similar results, which indicated a similar band structure around this Sb % range. They are both more semiconducting than the 7% Sb and 21%Sb, which is consistent with the band gag picture.

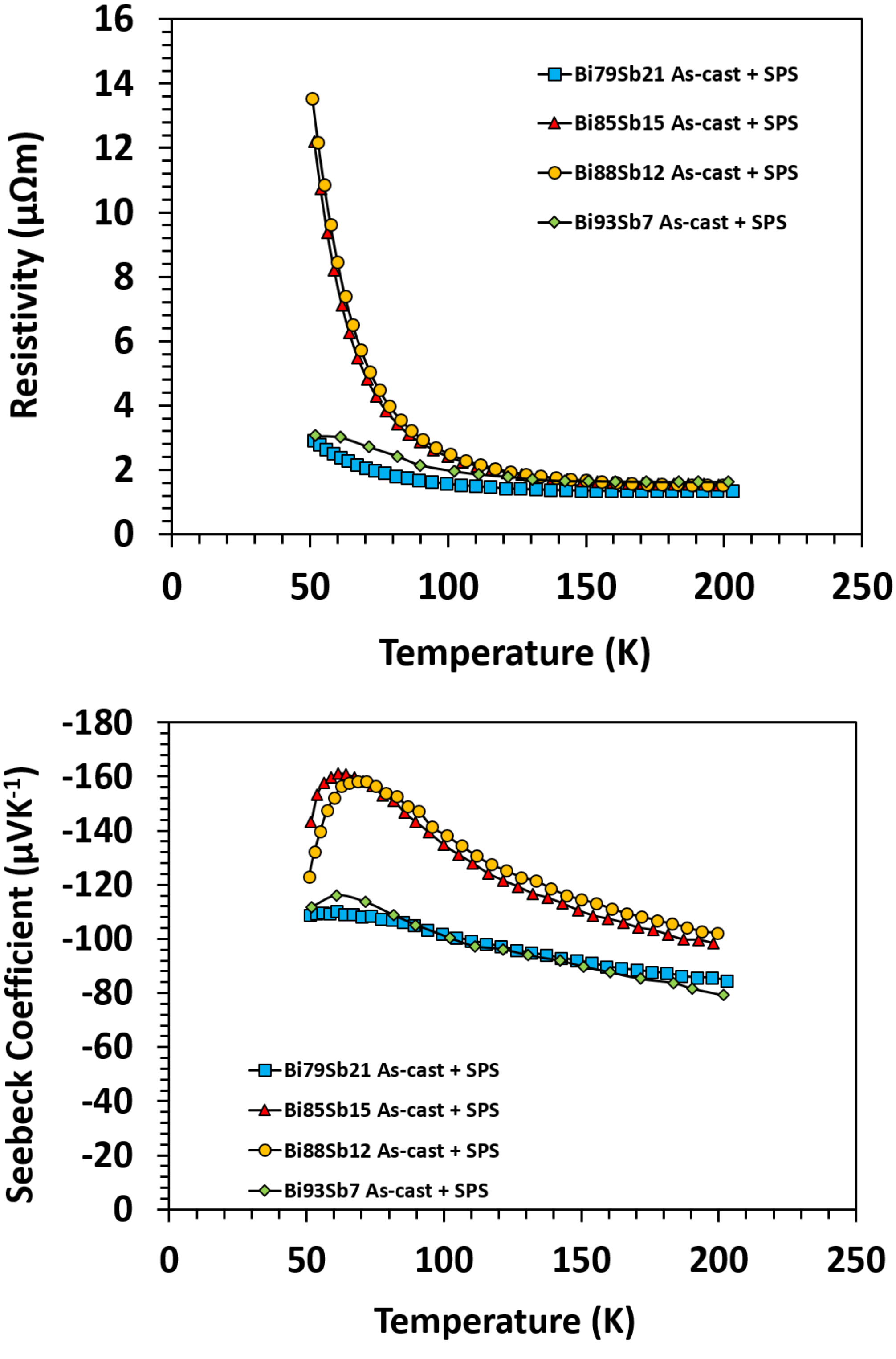

Figure 3-15: TE properties of $Bi_{100-x}Sb_x$ with Different Sb Concentration

3.2.3 As-casted, ball-milled and melt-spun samples

Fig. 3-16 showed the thermoelectric properties of $Bi_{85}Sb_{15}$ with different synthesis procedures.

The lower resistivity and Seebeck coefficient of the as-cast sample were mainly due to the composition variation(knowing 12% - 15% Sb would give a higher resistivity and Seebeck coefficient) and lack of grain boundary scattering.

The BM samples were made by ball milling the ingots in an argon atmosphere for different processing time. Comparing with the as-cast sample, the 7 minutes ball milled sample showed increased resistivity and Seebeck coefficient at a lower temperature, indicating a larger energy gap from a more uniform sample, and possibly an extra scattering involved due to smaller grain size. The 30 minutes ball milled sample followed the increasing trend and showed a much stronger effect compared with the 7 minutes ball milled sample. However, the massive increase in resistivity did not lead to a significant increase in the Seebeck coefficient. On the contrary, the Seebeck coefficient even dropped at the lower temperature end, which indicated a possible deterioration from the oxidation or iron contamination during the longtime high energy ball milling. Considering the limitation with our current glove box equipment, the argon environments may not be good enough. Therefore, oxygen is more likely to be the key factor that changed the TE properties by forming localized states at low temperatures which would lead to higher resistivity.

After all, the melt-spin + SPS sample showed the highest Seebeck coefficient with a decent resistivity. Therefore, the MS + SPS method was selected as a major preparation method.

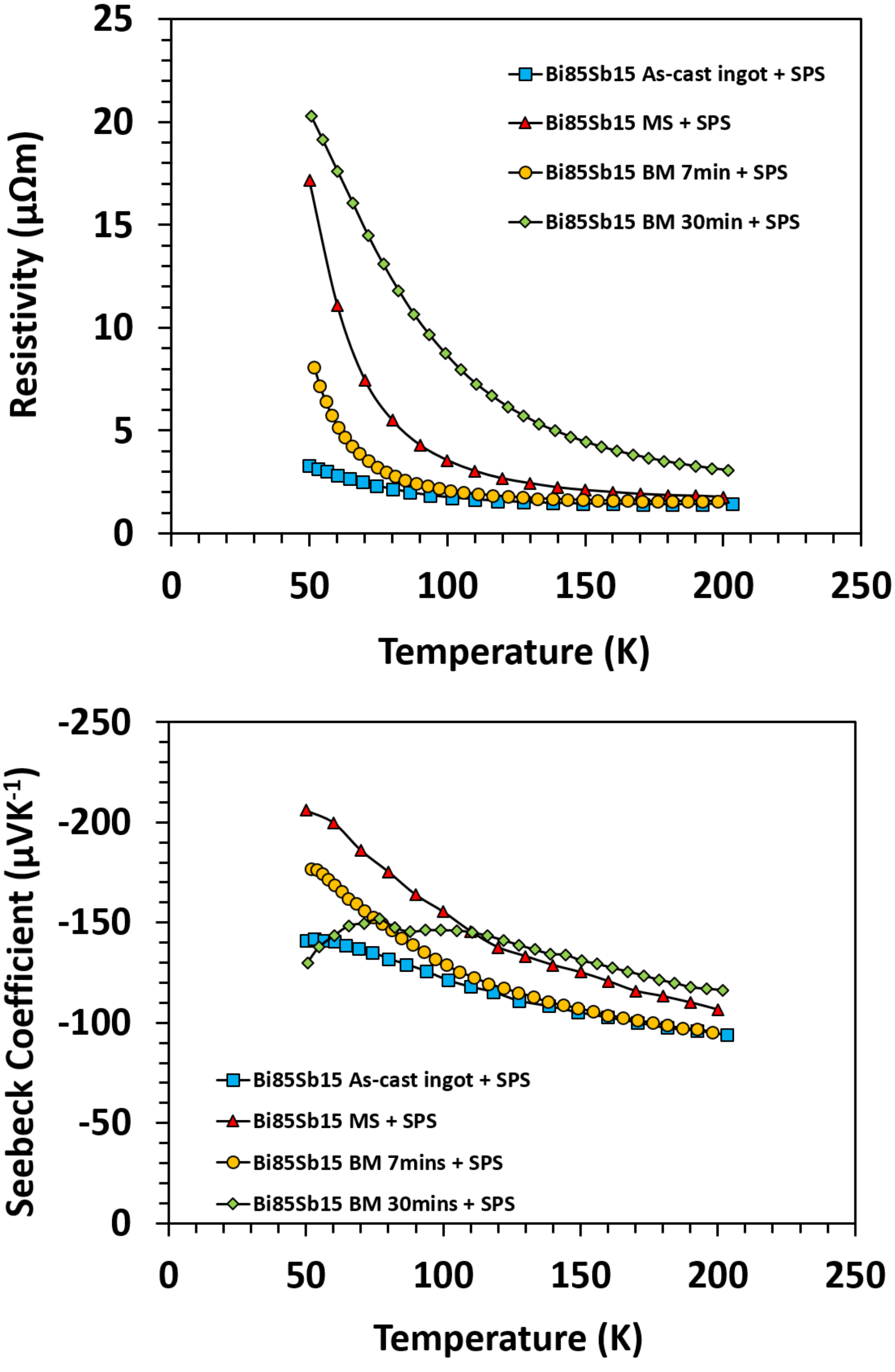

Figure 3-16: TE properties of $Bi_{85}Sb_{15}$ with Different Synthesis Procedures

3.2.4 High pressurized samples

Fig. 3-17 showed the TE properties of melt-spun $Bi_{85}Sb_{15}$ under different high-pressure treatments, the detailed conditions were listed in Table. 3.1.

Pre He-LT sample showed almost no difference from the regular MS + SPS sample, it means this method could preserve the TE properties of the Bi-Sb matrix, which is an important feature when applying to the p-type systems later on.

The post HP sample was made by applying high pressure along vertical direction while keeping the sides of the sample restricted. Therefore, there might be strain generated and stored inside the lattice due to the change of lattice constants. This could also lead to an increase in the energy gap, which resulted in a peak shift to the high-temperature side for resistivity and Seebeck coefficient as we have seen.

The SPS HP Deformed sample was high pressure compressed in a larger die under a non-constrain condition. A plastical deformation happened and the original disk was expanded by 30% in radius. The results showed much stronger effects on TE properties from this deformation, which indicated a possible band movement. At the same time, it is also possible to have small internal cracks inside the sample because of the plastical deformation, and these cracks might contribute to the increase of the resistivity as well.

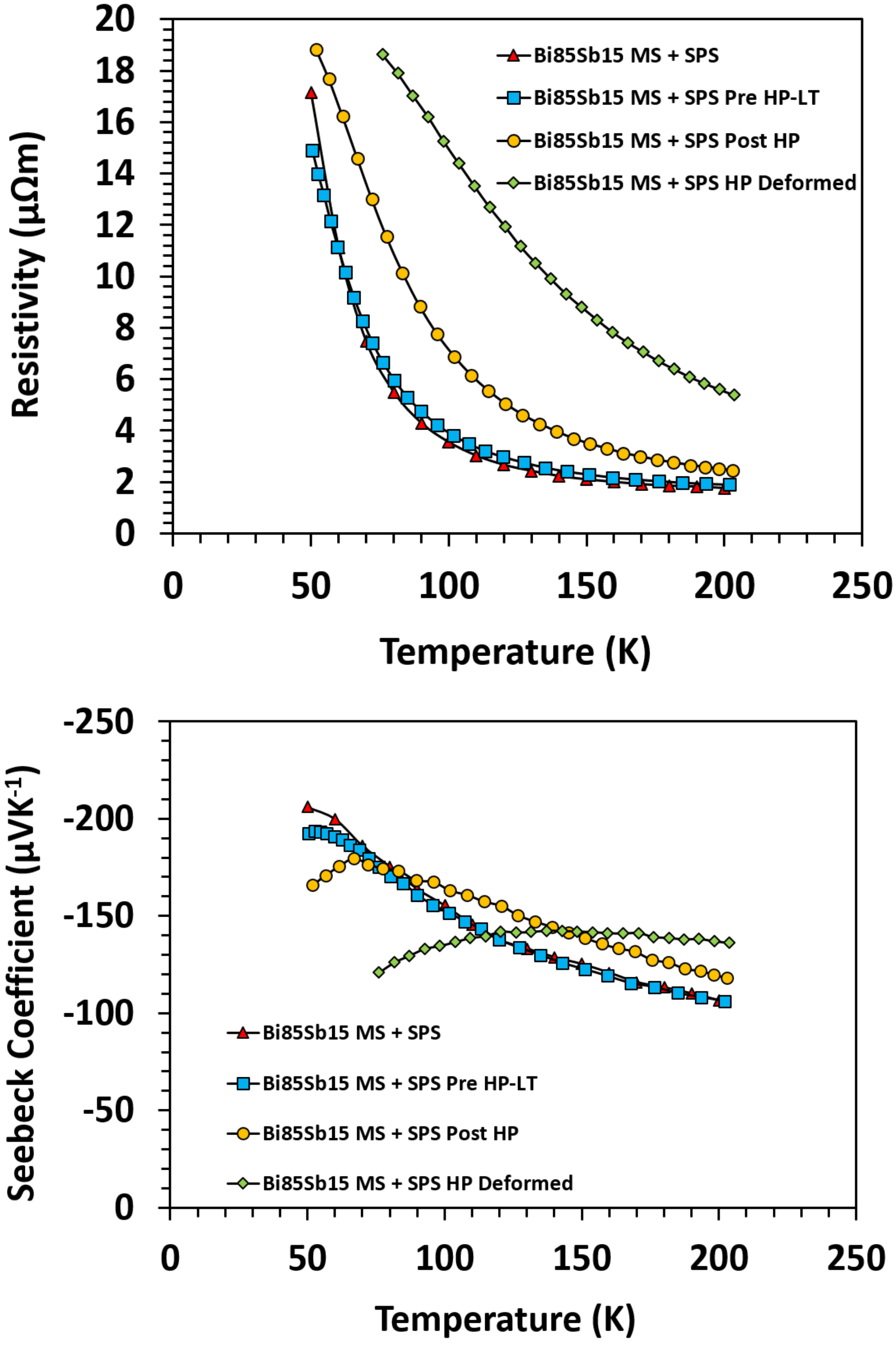

Figure 3-17: TE properties of $Bi_{85}Sb_{15}$ MS + SPS with High Pressure Treatments

3.2.5 N-type doping effect

Fig. 4-1 showed the resistivity of n-typed doped Bi-Sb alloys. This study was processed by measuring resistivity on Versalab fist, so only selected samples were measured for the Seebeck coefficient. The results showed the n-type dopants could be approximately divided into two groups:

(1) The transition metals, which significantly increased the resistivity. Based on the Hall measurements, it was known that the transition metals would introduce a few more electron carriers into the system. Therefore, the increase of resistivity indicated a dramatical drop of electron mobility, which may be due to the extra scattering between the electron carriers and the introduced dopants.

(2) Te and Se. Only 0.1% Te or Se was already enough to turn the semiconducting Bi-Sb alloys back into semimetals. The reason was the introducing of the massive amount of carriers, which was ten times more than the original concentration in undoped, as shown in the Hall measurements.

These studies may not lead to a higher figure of merit ZT for n-type Bi-Sb alloys. However, the idea of being able to modify the electron mobilities was the reward of this work, which would play a role in improving the p-type Bi-Sb alloys later on.

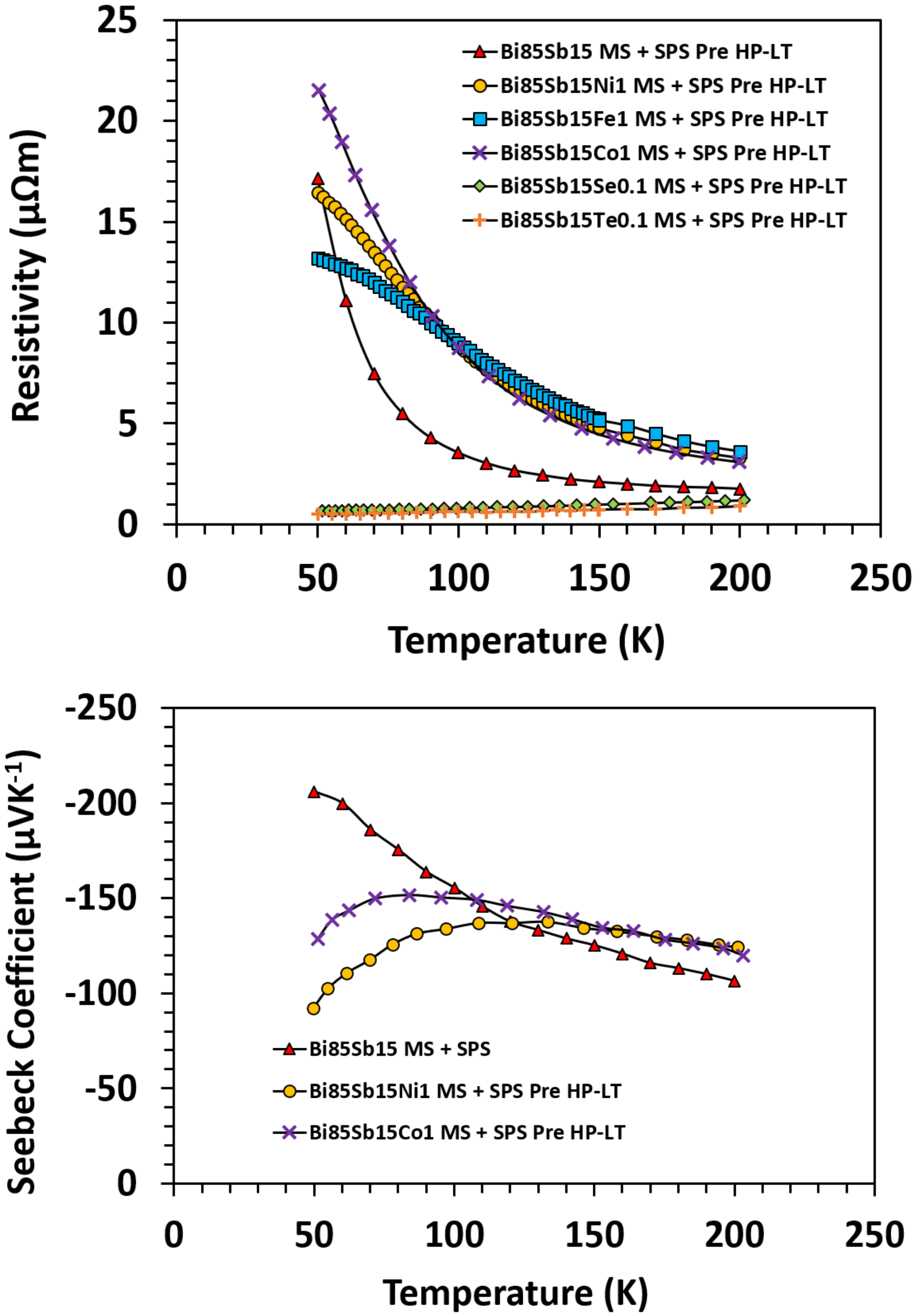

Figure 3-18: TE properties of N-type doped $Bi_{85}Sb_{15}$ MS + SPS Pre HP-LT

3.2.6 Measurements in magnetic fields

Bi-Sb single crystals were known to exhibit high magneto-thermoelectric effect whereby the thermopower measured along the trigonal axis increased when a magnetic field (B) was applied along the binary and bisectrix directions [65, 79]. In Fig. 3-20, magneto-resistance and magneto-TE properties in magnetic fields up to 4 kOe were shown for our Bi85Sb15 nanobulk sample. A consistent increase in ρ with B was observed for all temperature ranges. At the same time, enhancement in the Seebeck coefficient was also found above 50K. This magneto-TE effect could be explained on the basis of the transverse-transverse thermo-galvanomagnetic effects [65, 79], which are the results of co-action between the Hall effect, Nernst effect and Righi-Leduc effect. Fig. 3-19 shows the four different types of magneto-thermoelectric effects, the current and heat flows could generate electrical voltage or thermal gradient by interacting with magnetic fields.

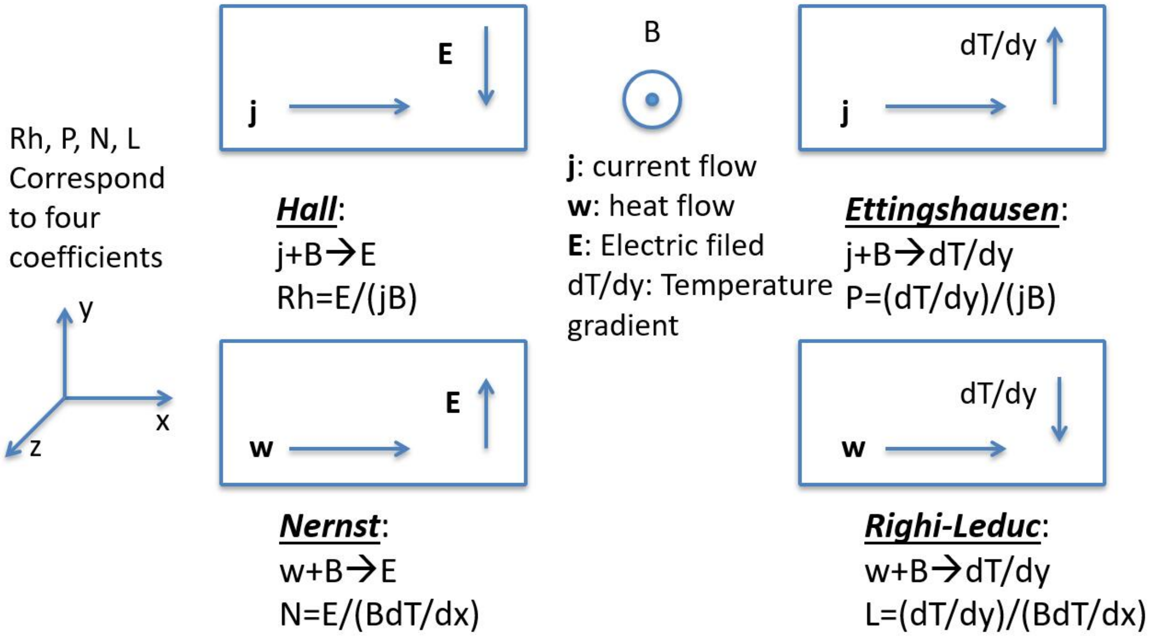

Figure 3-19: Basic Magneto-thermoelectric Effects

For a simplified discussion, considering orthogonal heat flow and uniform magnetic field in an isotropic polycrystalline Bi-Sb alloy, the thermopower enhancement has a quadratic dependence on the applied magnetic field given by :

$$\Delta S = B^2 \left(N R_H \sigma + L_R N \right) \tag{3.2}$$

where N is the Nernst coefficient, R_H is the Hall coefficient, L_R is the Righi-Leduc coefficient, σ is the electrical conductivity and ΔS is the change of measured adiabatic Seebeck coefficient in a magnetic field B. For the Bi-Sb system, $L_R << R_H \sigma$, therefore the second term could be neglected and only the Nernst and Hall effects need be considered [79]. Eq. 3.2 could be understood as the electrical current density activated by a heat flow in the Nernst effect was further interacted with magnetic field in a Hall effect, resulting in an enhancement of voltage back to the same direction of the original heat flow. In the weak field limit, $\Delta \mathrm{S} \sim -\mu\sigma B^2$ and $\Delta p \sim \mu B^2$, the extremely high electron mobility led to a high Nernst coefficient in Bi-Sb alloys, bringing about the appreciable increase in thermopower. Meanwhile, the magnetoresistance also increased due to high mobility. In lieu of measurement of thermal conductivity in a magnetic field, we can only estimate the optimal ZT, which occurs around 3 kOe.

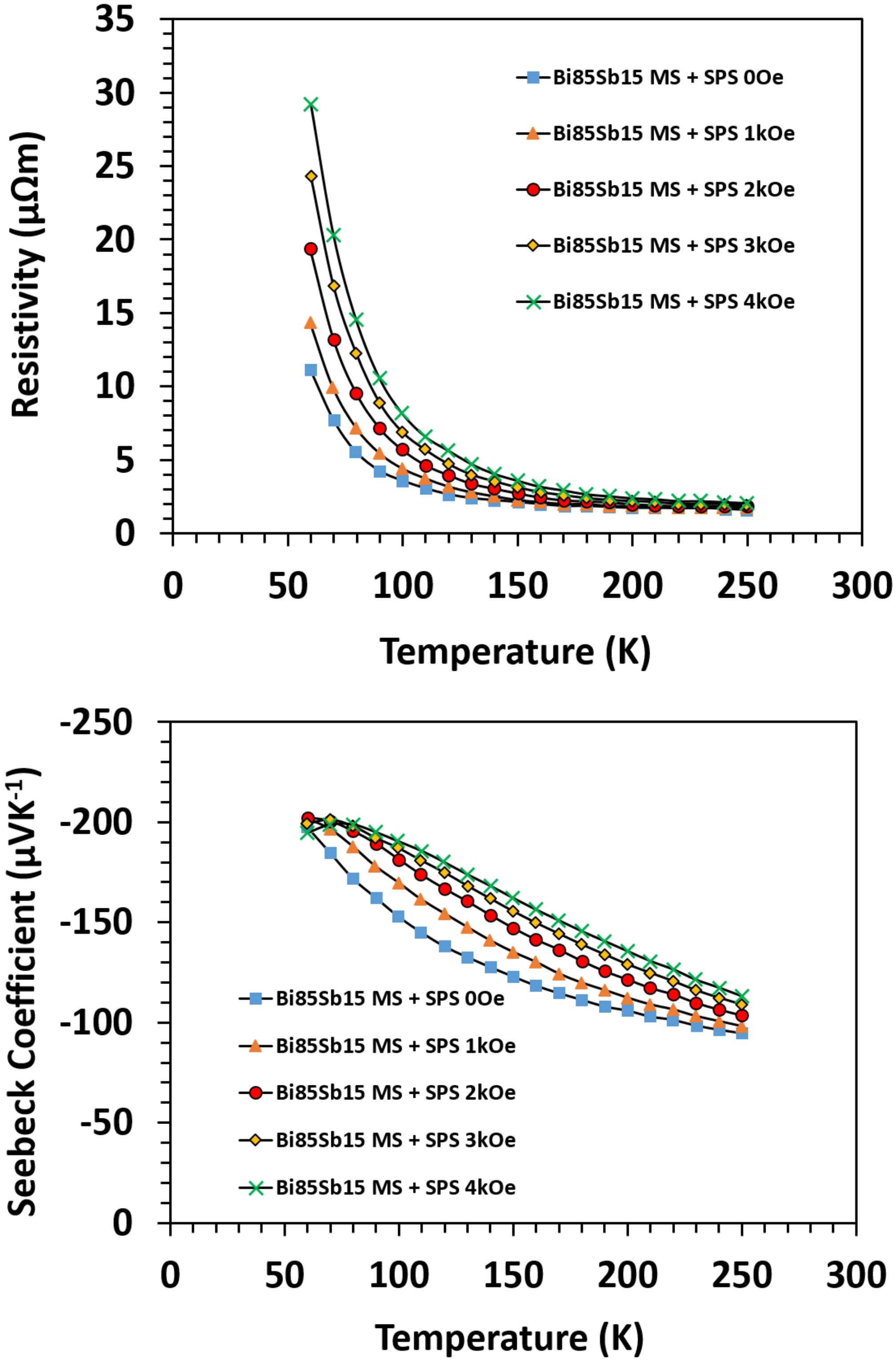

Figure 3-20: TE properties of $Bi_{85}Sb_{15}$ MS + SPS in Different Magnetic Fields

3.2.7 Realization in portable magnetic field

In order to exploit the observed magneto-TE effect in a portable thermoelectric cooling device, the device must necessarily be physically compact. For the present Bi-Sb alloys, it is possible to generate a moderate magnetic field near 3 kOe in the TE sample with a pair of âĂIJtoyâĂİ level NdFeB magnet plates. As shown in Fig. 3-21, two NdFeB magnet plates of 0.8mm thickness with magnetization near 1.3 T were configured parallel to each other with the 2-mm wide Bi-Sb sample sandwiched in between. The simulated magnetic field profile inside the sample showed a rather uniform magnetic field distribution in the range 3 âĂŞ 3.3 kOe, except for the small areas near the edges.

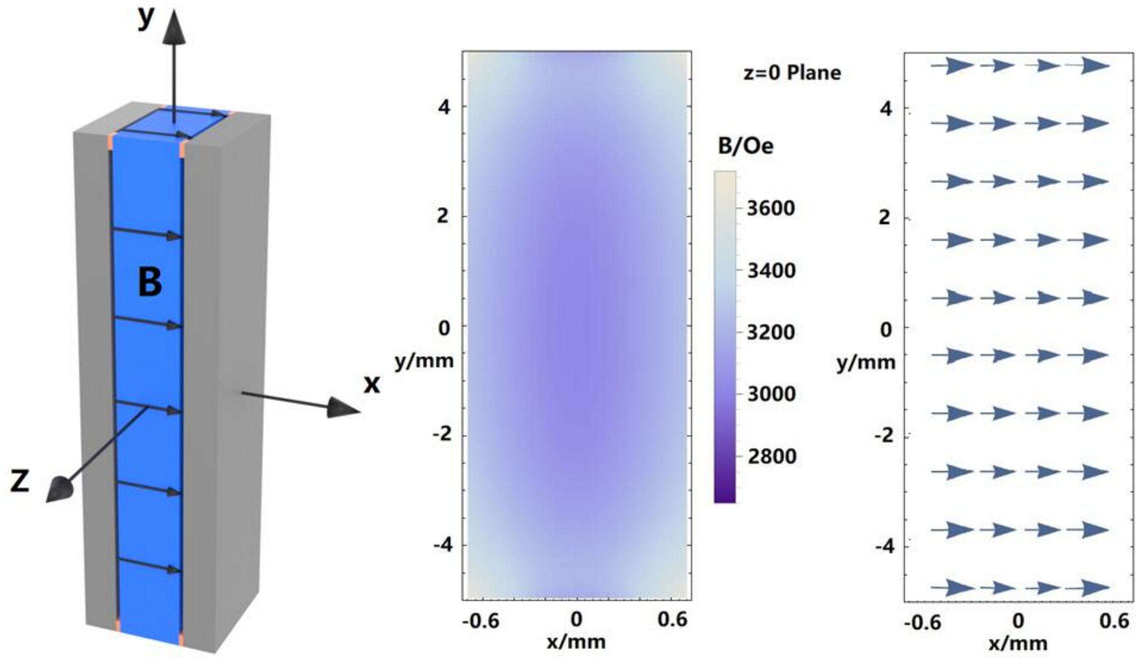

Figure 3-21: BiSb Sample (blue) and NdFeB Magnet Plates (grey) Setup and Simulated Magnetic Field Profile. The Origin O is located at the center of the sample. The strength and direction distributions of the magnetic field in z=0 plane are shown in the center and right illustrations, respectively.

In our thermoelectric measurements using PPMS, part of the surface area of the sample was occupied by thermal and electrical contacts made of copper rings. Therefore, only the middle half of the sample was covered by a pair of magnet plates, as shown in Fig. 3-22. The magnet plates were fixed to the sample with four narrow strip of double-sided insulating tapes. Thus, a thin gap was left in between each magnet plate and the sample to minimize the heat loss in the Seebeck coefficient measurement. The TE properties were measured for the sample segment between the two thermometers attached to copper rings C_1 and C_2. The sample segment can be divided into three parts connecting in series: (1) Middle part in magnetic field, with length L_{M}. (2) Two separated parts in near-zero field, with length L_0. Therefore, the thermoelectric properties of the middle part between the pair of magnet plates could be calculated based on the measurement.

The results of the estimated thermoelectric properties between the 3kOe magnet plates are shown in Fig. 3-23. It shows good agreements with the data in uniform 3 kOe fields obtained using PPMS.

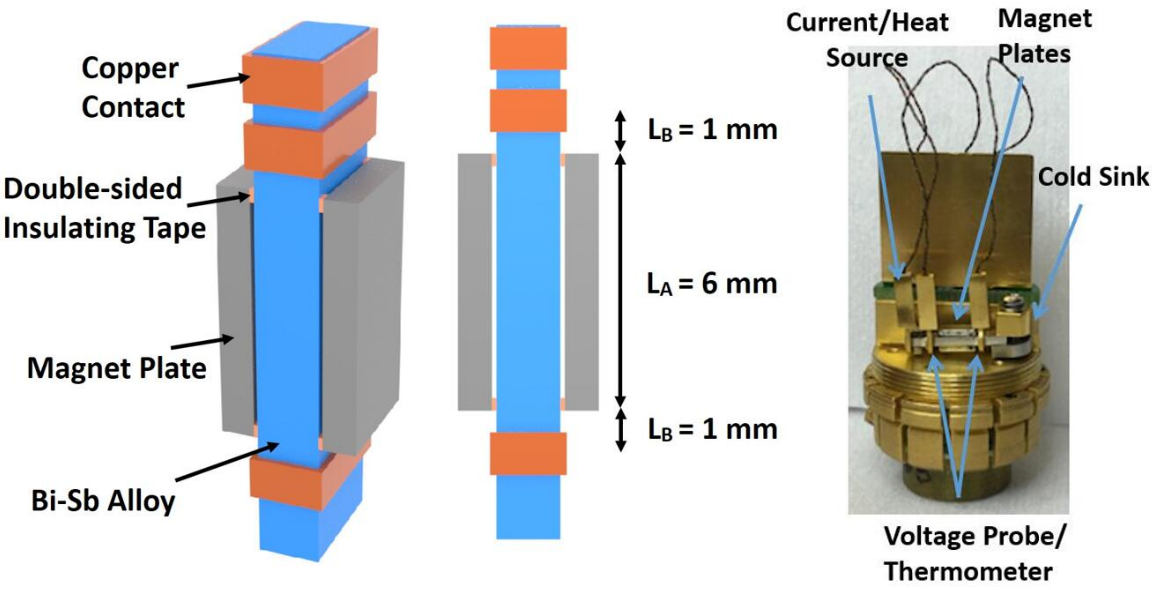

Figure 3-22: Demonstration of Thermoelectric Measurements Using PPMS with a pair of Magnet Plates on the Sample.

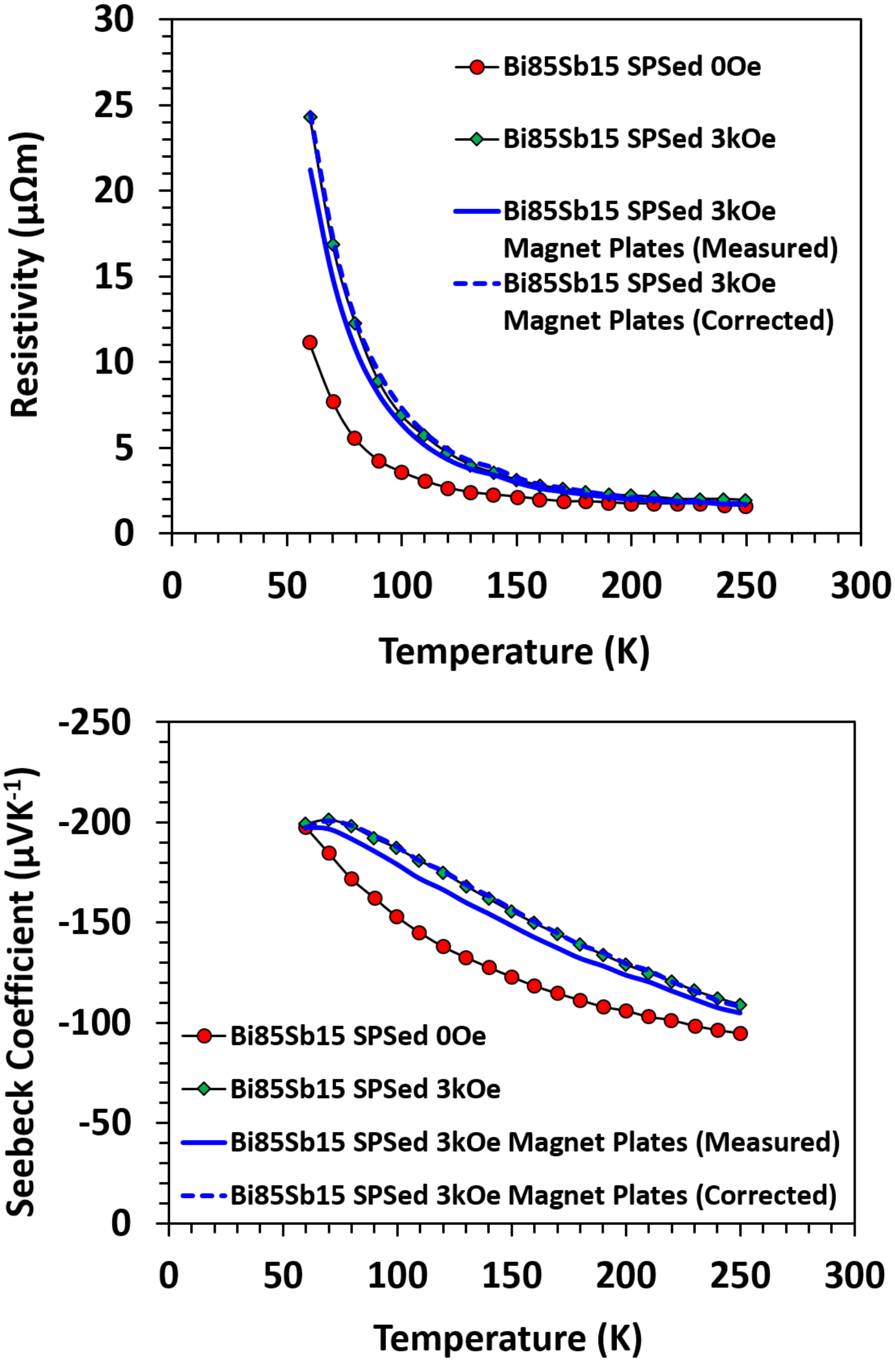

Figure 3-23: Magneto-resistance and Magneto-Seebeck Coefficient of $Bi_{85}Sb_{15}$ MS + SPS with Portable Magnet Plates

3.3 Thermoelectric measurements of p-type Bi-Sb alloys

The biggest difficulty in the synthesis of p-type Bi-Sb alloys is the incorporation of p-type dopants. Experiments showed possible dopants that can be used in the p-type Bi-Sb system are Sn, Pb and Ge. However, except for Sn having a small solubility in Bi, both Pb and Ge will not be able to dissolve in Bi or Sb at all. Using rapid cooling rate through the melt-spinning process helped freeze the dopants into Bi-Sb solid solution, made it possible to keep the dopants in the ribbons. However, in the SPS process at 240C, the higher atoms activities might lead to a rejection of dopants again. Therefore, as we discussed in chapter 2.6, a pre-high-pressure low-temperature SPS process was used on the p-type Bi-Sb alloys, marked as "Pre HP-LT", the detailed SPS conditions can be found in Table. 3.1. This method was also proven to not changing the TE properties of n-type Bi-Sb from Fig. 3-17.

3.3.1 Hall measurements

Knowing undoped Bi-Sb is an n-type alloy, introducing p-type dopants will form a two channel system. Therefore the Hall coefficient will be contributed by both electrons and holes. However, at low temperature region ($<$100K), where the electrons are inactive, leads to a hole dominated extrinsic system. The net carrier concentration will nearly become constant, which could represent the concentration of the dopants. And the approximation for single band Hall coefficient will be valid again:

$$R_H = \frac{\left(p\mu_p^2 - n\mu_n^2\right)}{e\left(p\mu_p + n\mu_n\right)^2} \approx \frac{1}{ep} \tag{3.3}$$

where n and p are the electron and hole concentrations, μ_n and μ_p are the electron mobility and hole mobility, respectively, and e is the unit charge. So in this section, the results of Hall measurements of p-type Bi-Sb alloys will be presented in the 50K to 100K range.

Pre-high-pressure low-temperature SPS treatments

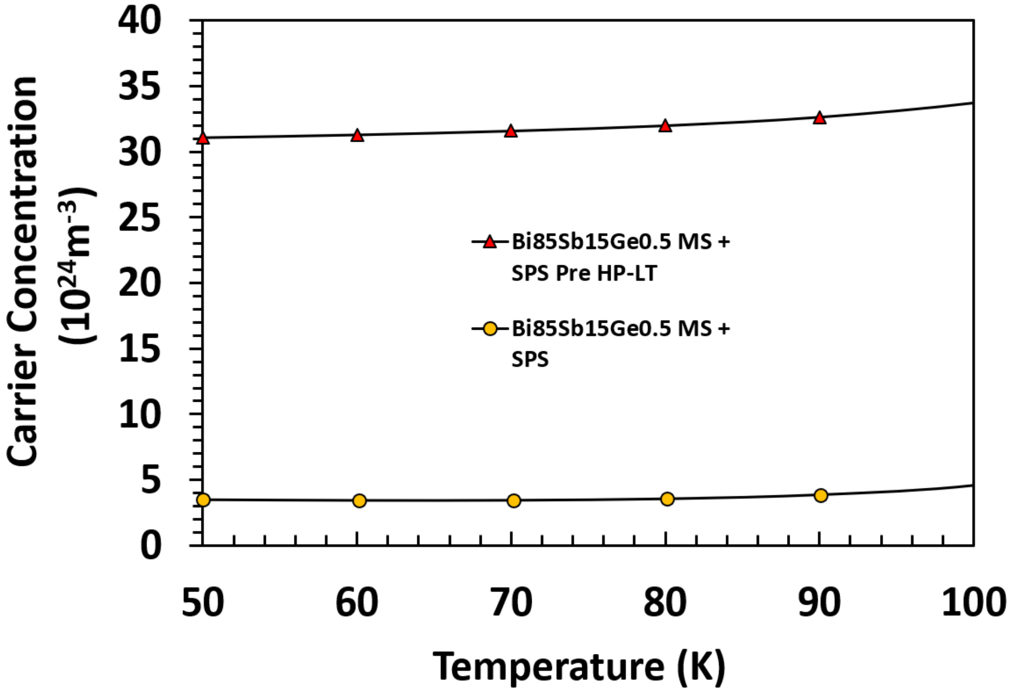

Figure 3-24: Carrier Concentrations of Different SPS Conidtions for P-Type Bi-Sb

Fig. 3-24 showed the difference in carrier concentration of different SPS conditions with the same composition. Using the Pre HP-LT SPS method increased the doping level by almost 10 times for Ge doping. This method has been proven as an effective way to incorporate dopants. Therefore, the Pre HP-LT method was considered as a primary SPS treatment for p-type samples.

Doping efficiency

To study the doping efficiency of Ge/Sn/Pb in $Bi_{85}Sb_{15}$, we investigated a set of samples that included $Bi_{85}Sb_{15}(Ge, Sn, Pb)_{0.1,0.5}$ and $Bi_{85}Sb_{15}(Ge, Sn)_5$, as shown in Fig. 3-25. Considerable difficulty was encountered in producing melt-spun ribbons of $Bi_{85}Sb_{15}Pb_5$ due to the viscosity of the molten alloy.

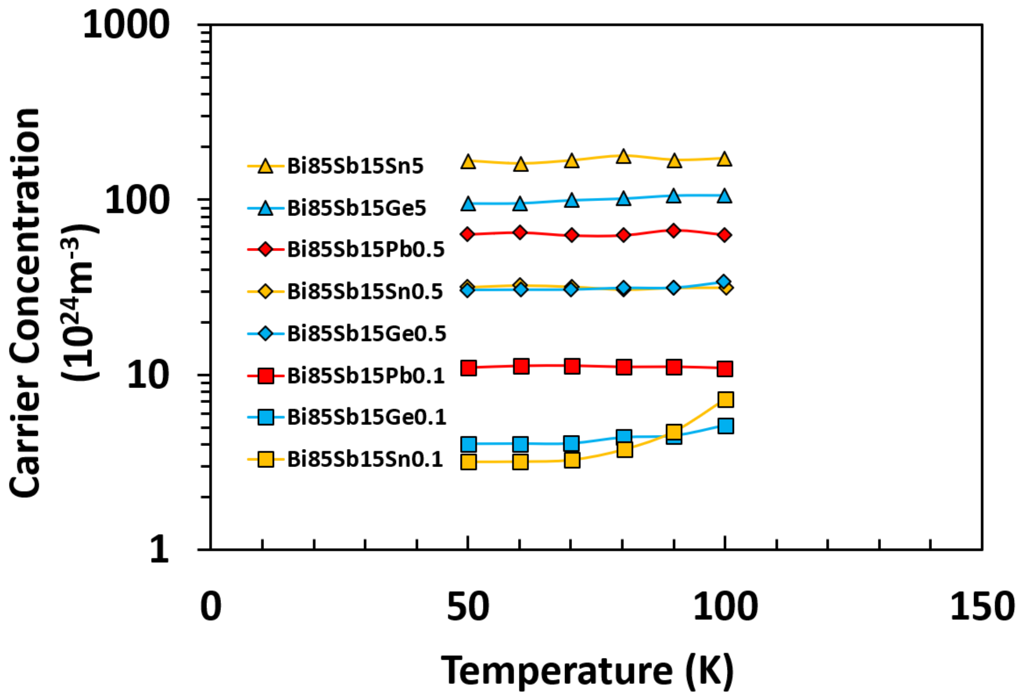

Figure 3-25: Carrier Concentrations of Different P-Type Bi-Sb Alloys

If all the dopants occupy substitutional sites in $Bi_{85}Sb_{15}$, and act as acceptors, the nominal hole concentration can be calculated since Ge/Sn/Pb atoms have valence 4 while the Bi and Sb atoms have valence 5. The result is shown in Table. 3.2. However, after analyzing the Hall coefficient data, we found that not all of the Ge/Sn/Pb atoms go into substitutional sites because the number of holes in experiments was much lower than the nominal values. A proportion of the Ge/Sn/Pb atoms might go to the interstitial sites in $Bi_{85}Sb_{15}$, and acted as interstitial donors [94].

Assuming that each Ge/Sn/Pb atom occupies a substitutional or interstitial site and acts as an acceptor or a donor in the system, we can derive the number of donor and acceptor sites and calculate the doping efficiency with the charge neutrality equation:

$$p + N_d^+ = n + N_a^- \tag{3.4}$$

where N_d^+ and N_a^- are the concentrations of donors and acceptors.

Here the doping efficiency is defined as the ratio of the hole concentration to the acceptor concentration [95]. The concentrations of donors N_d^+ and acceptors N_a^- and the doping efficiency of the doped samples are calculated (using the density of the samples as 9.32 g/cm^3). The obtained values are shown in Table. 3.2. We have also plotted N_a^- versus Ge/Sn/Pb doping levels in Fig. 3-26. Among Ge, Sn, and Pb, Pb has the highest doping efficiency (around 60%) in Bi-Sb. The atomic radii of Bi, Sb, Ge, Sn, and Pb are 156 pm, 140 pm, 122 pm, 140 pm, and 175 pm respectively. Because the atomic radius of Pb is larger than that of Bi and Sb, it is more likely for Pb atoms to occupy the substitutional sites rather than interstitial sites in the Bi-Sb matrix. As a result, there would be more substitutional acceptors in Pb-doped Bi-Sb than in Ge- or Sn- doped Bi-Sb given the same number of doping atoms. Ge and Sn shows comparable doping efficiencies. When the concentration of Ge/Sn is increased to 5% into Bi-Sb matrix, however, the doping efficiency decreases. At such high dopant concentration, the local (atomic scale) clustering of dopant atoms is unavoidable, which would diminish the effectiveness of the dopants as acceptors in the Bi-Sb host.

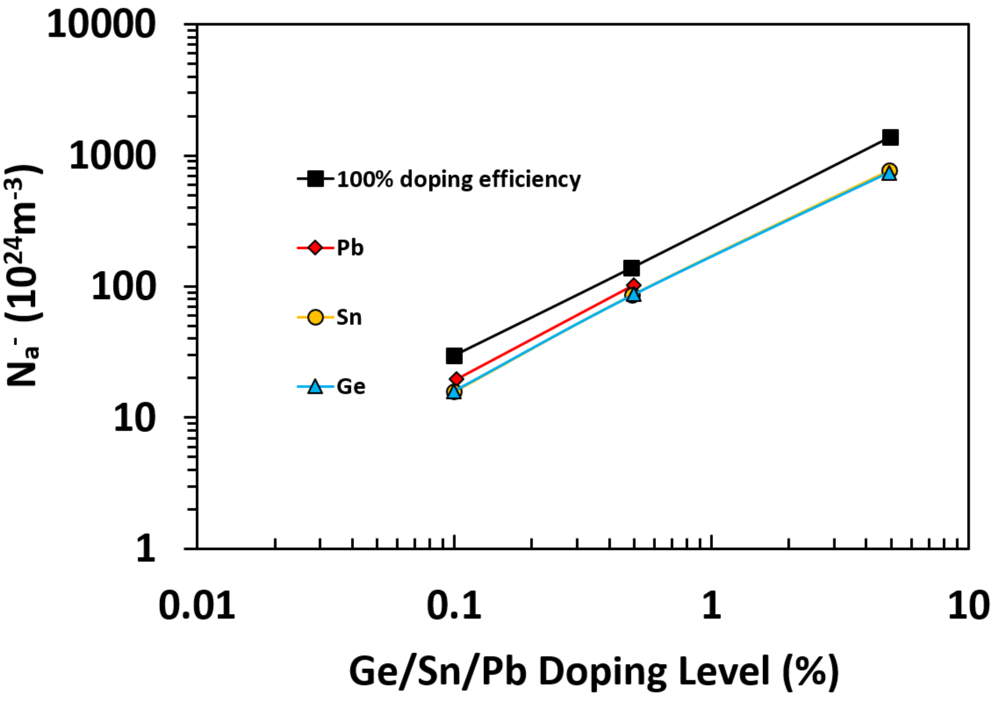

Figure 3-26: Carrier Concentrations of Different P-Type Bi-Sb Alloys

Table 3.2: Nominal hole concentration, N_d^+, N_a^- and the doping efficiency of the Ge/Sn/Pb doped $Bi_{85}Sb_{15}(Ge, Sn, Pb)_x$ samples

	0.1%Ge	0.5%Ge	5%Ge	0.1%Sn	0.5%Sn	5%Sn	0.1%Pb	0.5%Pb
Nominal hole concentration ($10^{25}m^{-3}$)	2.86	14.3	141	2.86	14.3	139	2.86	14.2
$N_d^+(10^{25}m^{-3})$	1.23	5.6	65.7	1.27	5.54	61.4	0.85	3.83
$N_a^-(10^{25}m^{-3})$	1.63	8.7	75.3	1.59	8.76	77.6	2.01	10.37
Doping efficiency (%)	24.7	35.7	12.7	20	36.7	21	57.7	63.1

3.3.2 Ge doped

Fig. 3-27 showed the TE properties of Ge doped $Bi_{85}Sb_{15}Ge_x$ alloys.

It was shown that with x=0.1 and 0.5, the systems have a very high resistivity(even higher than undoped n-type Bi-Sb), which indicates that part of the hole carriers was used to neutralize the electrons resulting in a low carrier concentration. The introduced carriers also increased the scattering that leads to lower carrier mobility. The system behaves as p-type dominated at low temperature but converts back to n-type around 120 to 200K as we could see in the Seebeck coefficient plot.

With the increase of the Ge doping level, the x=2 sample showed much lower resistivity and consistent increasing Seebeck up to room temperature, which means the additional dopants significantly increased the carrier concentrations.

On the contrary, the $Bi_{85}Sb_{15}Ge_x$ sample using the ordinary 240C SPS still showed high resistivity and negative Ge0.1 sample, indicating probably less 10% dopants was dissolved in the Bi-Sb matrix, which is consistent with the previous discussion of carrier concentrations obtained by Hall measurements.

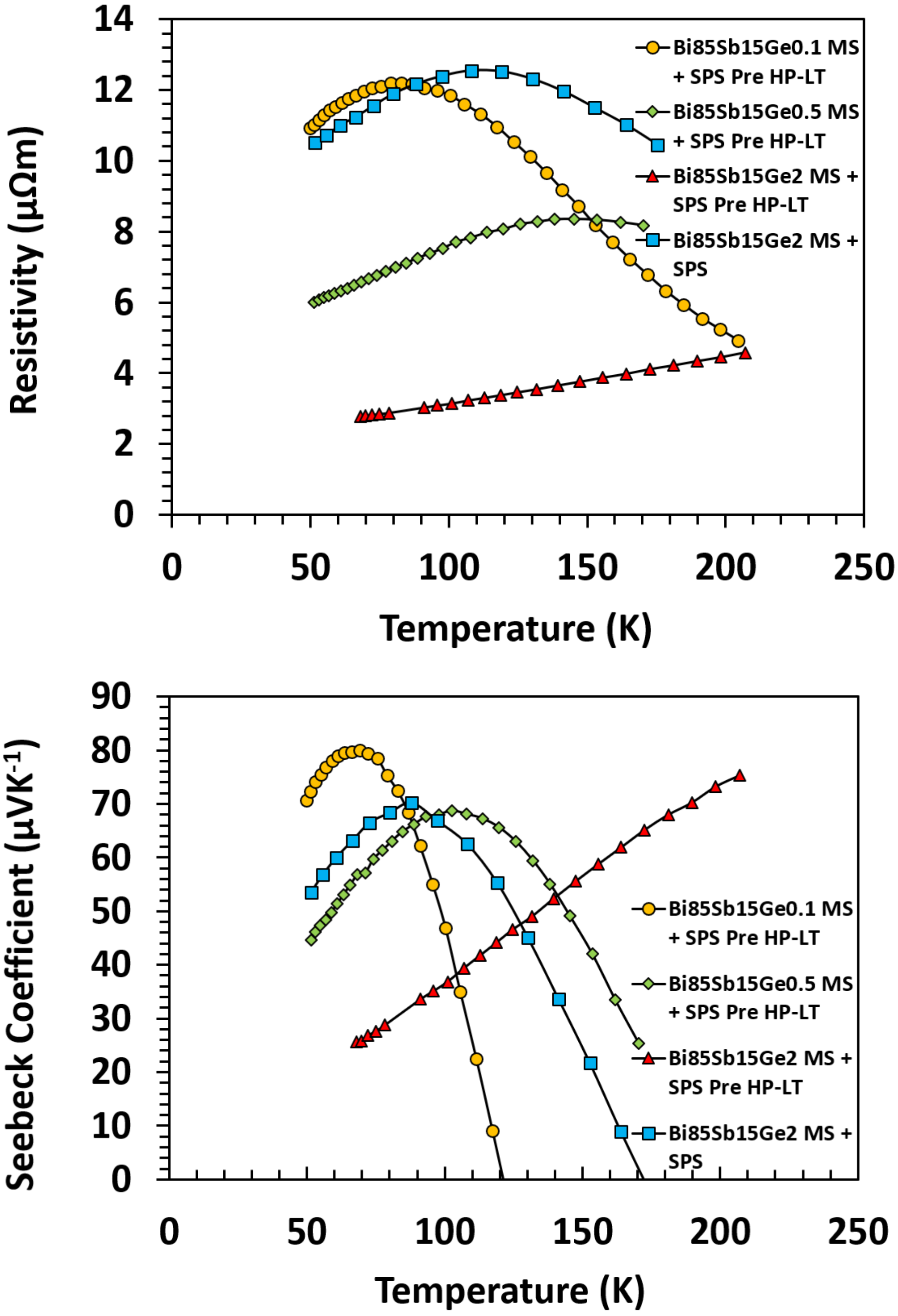

Figure 3-27: TE properties of $Bi_{85}Sb_{15}Ge_x$ MS + Different SPS

3.3.3 Sn, Pb doped

Fig. 3-28 showed the TE properties of $Bi_{85}Sb_{15}Sn(Pb)_x$ with x=0.1 and 0.5. The x=0.1 Sn doped sample showed a weakened n-type Seebeck coefficient and resistivity trend indicating the small amount of Sn dopants mostly went into interstitial sites instead of substitutional sites.

On the other hand, the x=0.1 Pb doped sample already showed p-type behavior, which means Pb is a more effective dopant than Sn. The reason could be due to Pb's larger atomic radius, which made Pb harder to sit in interstitial sites.

The x=0.5 samples showed similar behavior for both Sn and Pb, with a slightly higher Seebeck coefficient for Pb at higher temperatures. This means at a higher doping level, the effects from the amount of the initial interstitial sites atoms might be neglected.

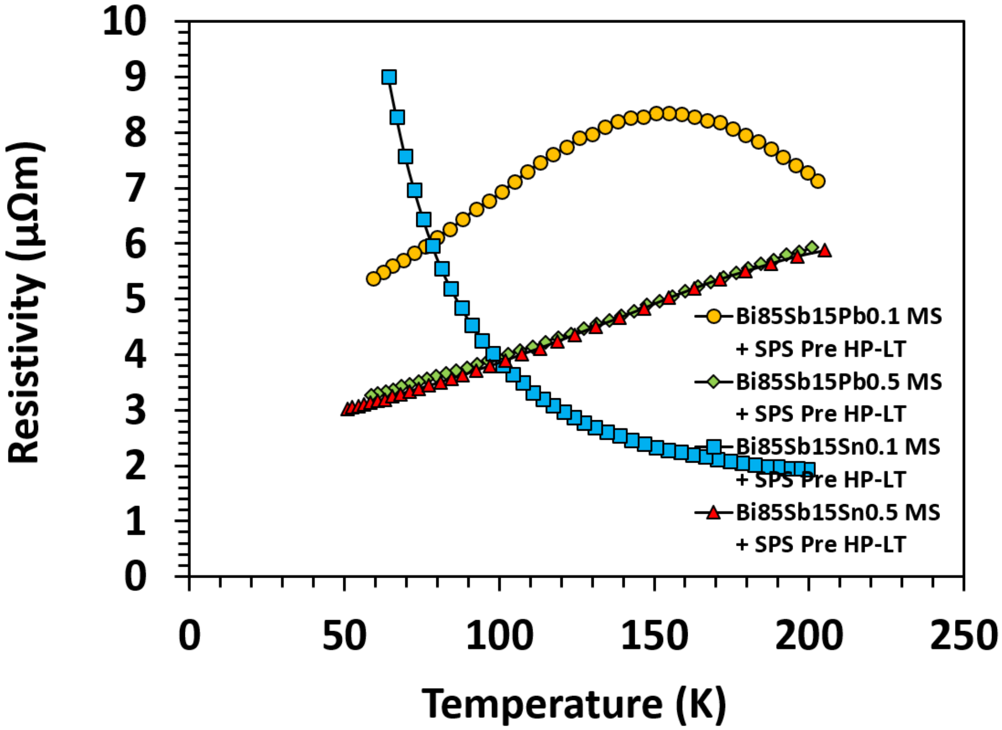

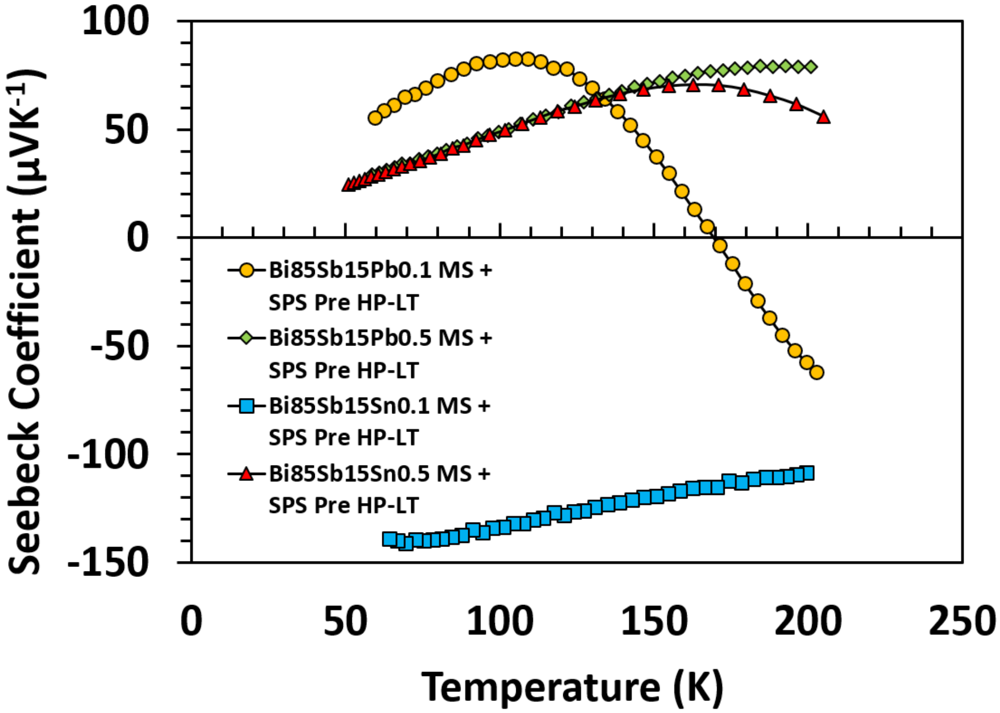

Figure 3-28: TE properties of $Bi_{85}Sb_{15}Sn(Pb)_x$ MS + SPS Pre HP-LT

3.3.4 Transition metals co-doped

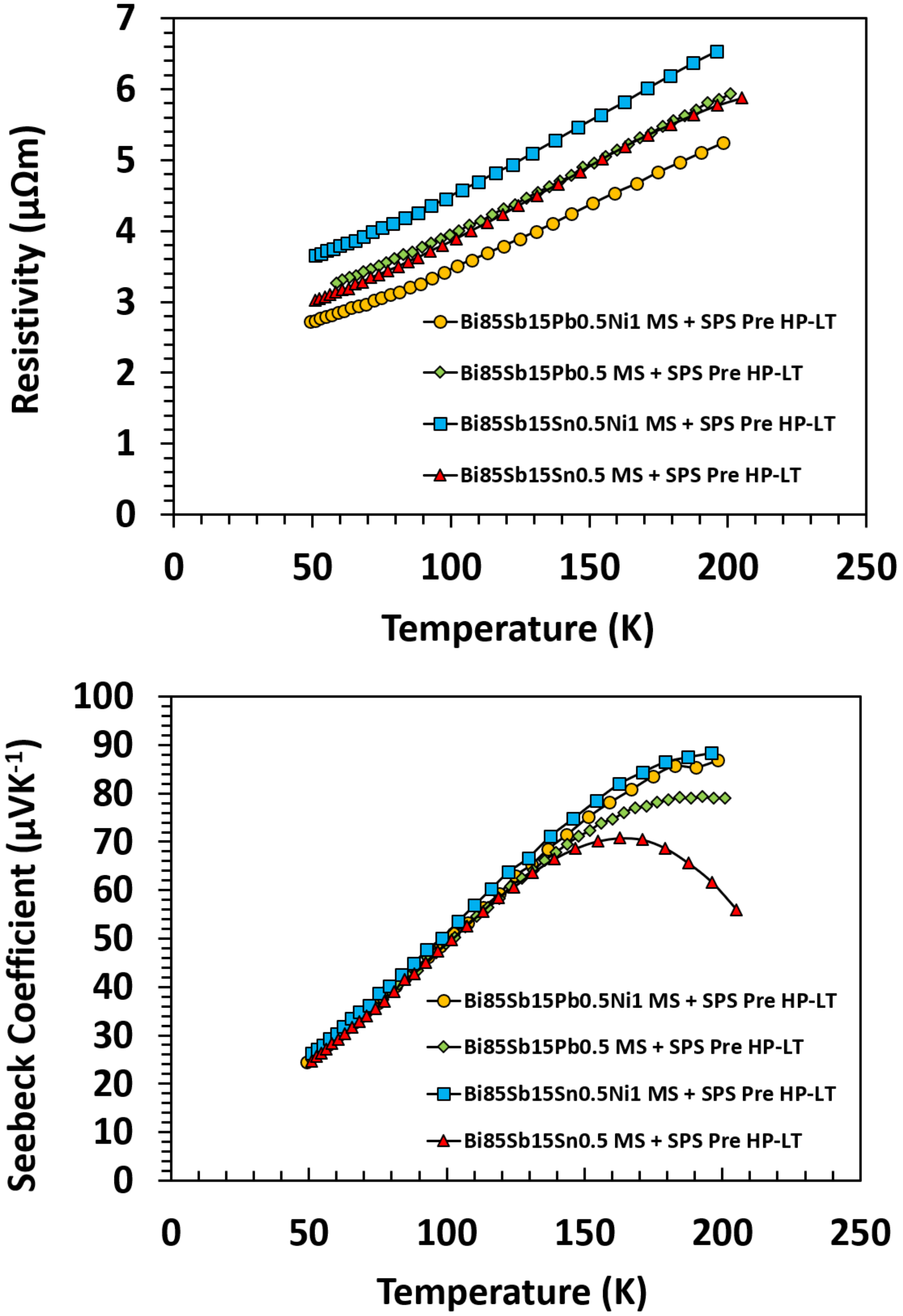

Figure 3-29: TE properties of $Bi_{85}Sb_{15}Sn(Pb)_{0.5}Ni_1$ MS + SPS Pre HP-LT

By studying the Seebeck coefficients of pure Ge, Sn and Pb doped Bi-Sb alloys, we noticed that a high doping level($0.5\% - 1\%$) might shift the peak to the room temperature end, which wouldn't benefit the properties at cryogenic temperature. With lower dopant concentrations (0.1%), we were able to achieve higher Seebeck coefficient at low temperatures, but the positive Seebeck coefficient might drop down to 0 very fast above 100K, and the resistivities were always very high. The reason could be the excitations of the electron. With the energy gap shrinking at higher temperatures for this narrow gap material, it was effortless to have high-mobility electrons activated and started to neutralize the holes. In the end, the electrons may overwhelm the holes and change the system back to n-type behavior.

One possible way to enhance the hole channel is to try to increase the hole mobility so that the holes could be stronger against the electrons. However, due to the complexity of the electronic structures, this was not easy to fulfill. Therefore, trying to weaken the electron channel become a natural choice.

N-type dopant Ni was used to co-dope with Sn and Pb, which was known to be able to effectively reduce the electron mobility as we have discussed in the n-type doping sections. The results were shown in Fig. 3-29. As expected, since the electrons were restricted, the p-type Seebeck coefficients at higher temperature were improved. What's more, for Ni-Pb co-doped sample, it could also help reduce the resistivity by increasing the effective carriers.

Besides Ni, other transition metals were also studied to co-dope with Pb. Fig. 3-30 showed the results of Fe and Mn. These transition metals also decreased the electron mobility that enhanced the Seebeck coefficient, but at the same time, the hole mobility was also reduced. Therefore, the overall resistivity was increased, which may not be as good as the Ni co-doped alloys.

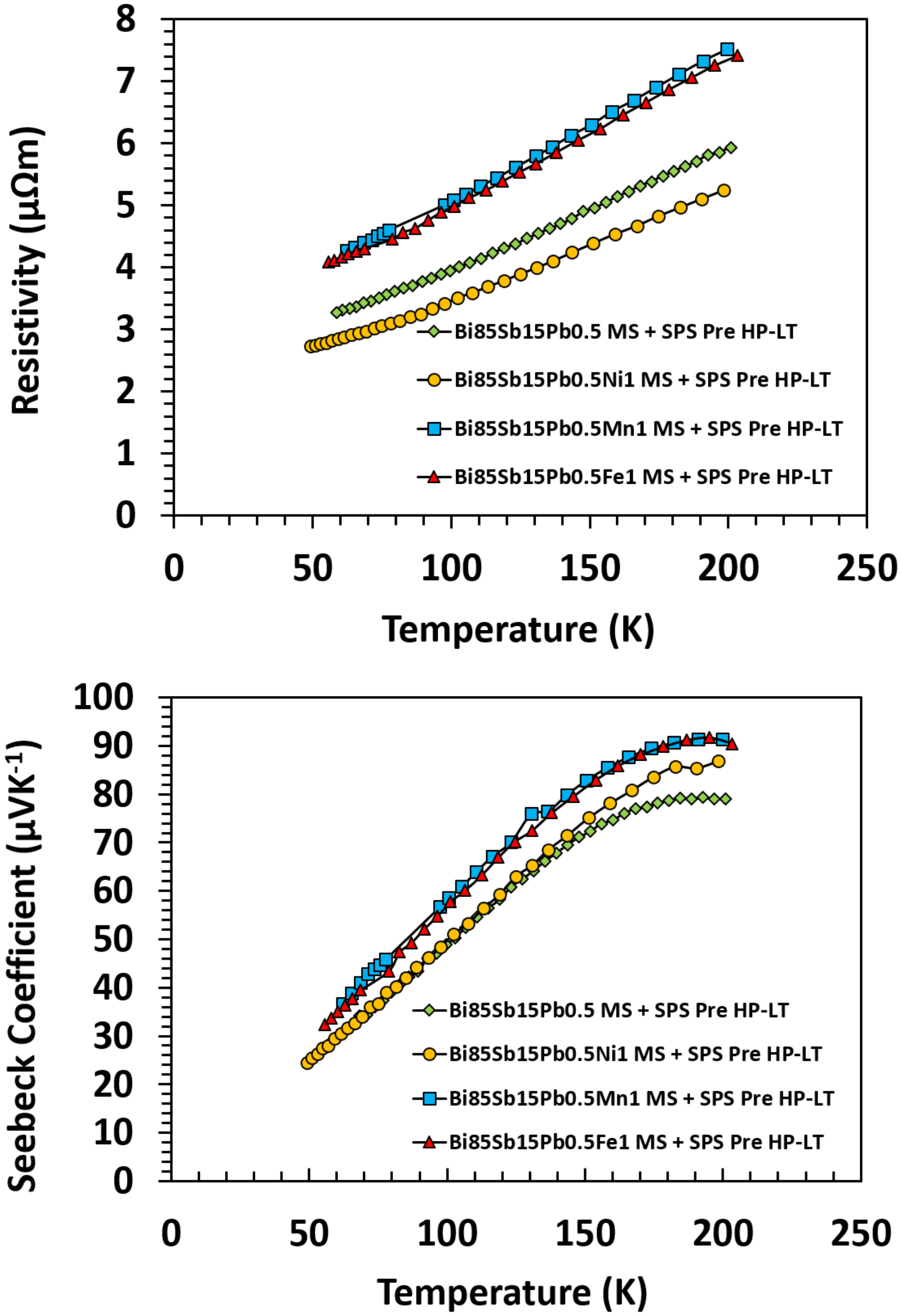

Figure 3-30: TE properties of $Bi_{85}Sb_{15}Pb_{0.5}Ni(Fe,Mn)_1$ MS + SPS Pre HP-LT

3.4 Thermal conductivity and Figure of merit ZT

3.4.1 Hot disk method

Among TE properties, thermal conductivity is usually the hardest one to measure accurately. Typical methods used in previous studies mostly relied on the heat flow across the whole sample with multiple high thermal conductivity metal contact leads on it. Unsystematic variations on thermal conductivity data have been observed in our measurements with PPMS using a similar technique, and previous studies by other groups relying on this type of measurement also reported a wide range of thermal conductivity [83, 96–98]. This indicated there could be a significant uncertainty on thermal conductivity measurements due to an inevitable heat loss during the heat transfer process or effects from metal contacts, especially for a low thermal conductivity system such as Bi-Sb. Therefore, an advanced thermal conductivity measurements method was used in this paper called the **hot disk** method. [99, 100]

The thermal conductivity of samples, down to 110K using a cold stage heat sunk to liquid nitrogen, were measured using a hot disk thermal constants analyzer. Hot disk, based on the commonly used transient plane source technique, uses an electrically conductive pattern encapsulated by an insulating material, in this case Kapton, to both source and sense an electrically generated heat source. Placing the sensor between two identical samples allows us to assume the heat source provided by the sensor is located in an infinite medium. The solution to the heat equation in this case yields an absolute measurement of the thermal conductivity of the sample. This is a key advantage over other thermal conductivity methods which often rely on measurements of thermal diffusivity or effusivity and calculate thermal conductivity by having a priori knowledge of the heat capacity of the material. This aspect of the measurement technique becomes increasingly important as we measure samples which do not have vetted literature values for heat capacity at room temperature or low temperatures investigated in this study.

3.4.2 N-type Bi-Sb

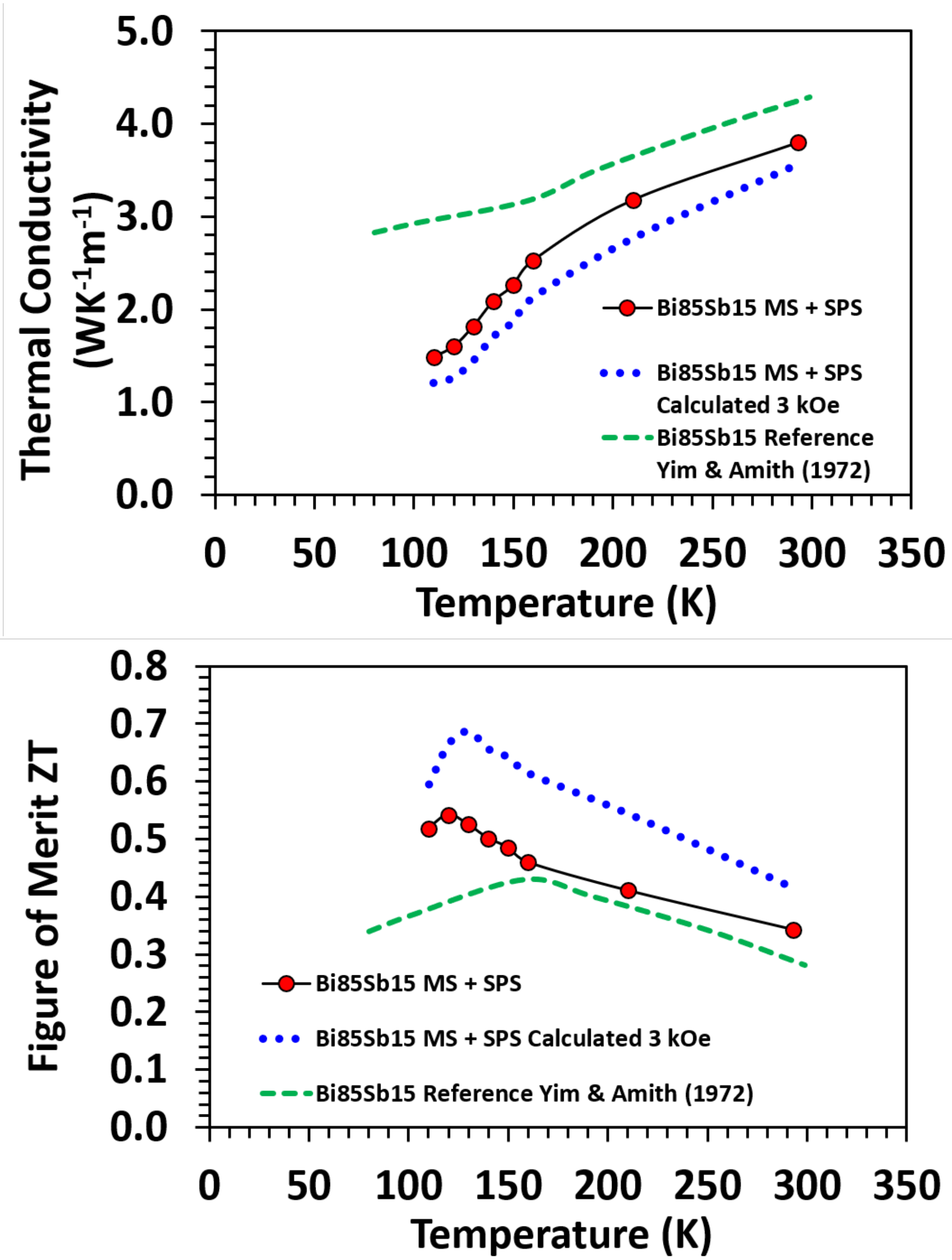

Figure 3-31: Thermal Conductivity and ZT of $Bi_{85}Sb_{15}$ MS + SPS

The sample with the best thermal power was selected to perform hot disk measurements. Temperature-dependent thermal conductivity data of $Bi_{85}Sb_{15}$ MS + SPS in 0 field measured using a hot disk method is presented in Fig. 3-31 together with the calculated dimensionless figure of merit ZT using the resistivity and Seebeck coefficient from Fig. 3-16. The results were compared with polycrystalline averaged reference data [79], where a direct average along three orthogonal axes (trigonal, binary and bisectrix axes) was taken for the single crystal. The thermal conductivity of $\sim 1.5WK^{-1}m^{-1}$ near 100 K is one of the lowest reported for an undoped Bi-Sb system [61, 79, 84, 85, 101].

The total thermal conductivity contained three different parts:

$$\kappa_{\text{total}} = \kappa_{\text{electronic}} + \kappa_{\text{lattice}} + \kappa_{\text{bipolar}} \tag{3.5}$$

Here reducing the κ_{lattice} played a key role in suppressing the $\kappa_{\text{ total}}$, which might be due to the extra boundary scattering introduced by a nano-scale fine structure. These potential barriers between nano-grains significantly limited the phonon mean free path, therefore dramatically reducing the κ_{lattice}.

The electronic part, $\kappa_{\text{electronic}}$, could be described using Wiedemann-Franz law:

$$\kappa_{\text{electronic}} = L\sigma T \tag{3.6}$$

where L is the Lorenz number.

At the low-temperature end (T <150K), where the bipolar term was relatively small and can be ignored in Eq. 3.5 8 due to the lack of hole carriers, the κ_{lattice} can then be estimated by subtracting $\kappa_{\text{electronic}}$ from $\kappa_{\text{ total}}$ It can be shown that our $Bi_{85}Sb_{15}$ MS + SPS has a $\kappa_{\text{lattice}} \sim 0.85WK^{-1}m^{-1}$ near 100K region, which is significantly lower than the value $\kappa_{\text{lattice}} \sim 1.5WK^{-1}m^{-1}$ for the polycrystalline averaged single crystal results of Yim & Amith [79] in the same temperature range. The Lorenz numbers used in the calculation were obtained from the Seebeck coefficient based on the empirical equation proposed by H. S. Kim etc. [102] ($L \sim 1.8 \times 10^{-8}W\Omega K^{-2}W$ for our sample and $L \sim 1.85 \times 10^{-8}W\Omega K^{-2}W$ for Yim & Amith's). This Lorenz number model showed good agreement with the values obtained from bands structure calculations with scattering assumptions. Even for the systems with multiple non-parabolic bands, the uncertainty was still within 20%. It can be regarded as a good approximation especially considering the typical measurement uncertainty for κ_{total} is already around 10%.

Even though our current hot disk method does not have the option of directly measuring thermal conductivity in a magnetic field, it is noted that the magnetic field dependence of κ is essentially determined by the magnetic field dependence of $\kappa_{\text{electronic}}$ [79]. As such, the Wiedemann-Franz law was used again to calculate the change in $\kappa_{\text{electronic}}$ for estimating the total thermal conductivity of our $Bi_{85}Sb_{15}$ MS + SPS in 3k Oe field. The figure of merit ZT in 3k Oe field was also calculated and presented in Fig. 3-31 together with the total thermal conductivity.

3.4.3 P-type Bi-Sb

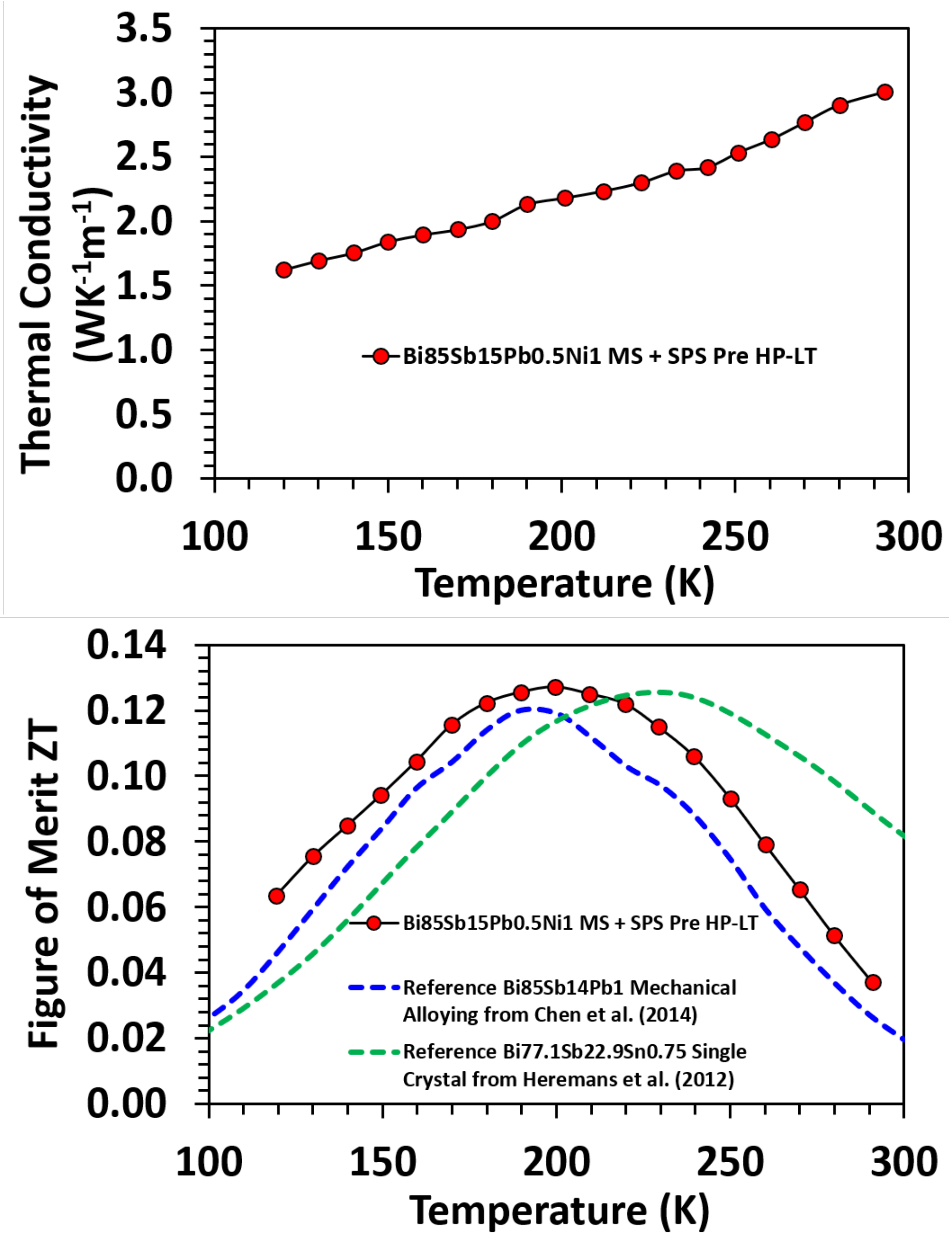

Figure 3-32: Thermal Conductivity and ZT of $Bi_{85}Sb_{15}Pb_{0.5}Ni_1$ MS + SPS Pre HP-LT

Fig. 3-32 showed the thermal conductivity and corresponding figure of merit ZT of selected p-type Bi-Sb alloys with best power factors. Two reference lines of the best p-type Bi-Sb alloys found in recent works were also plotted together for comparison [86,87]. Our sample showed an improved figure of merit ZT in the temperature range of 100K to 200K. It peaks at around 200K with a maximum ZT ~ 0.13, which is still far away from the ZT of the n-type Bi-Sb counterpart. This insufficient performance is probably due to the low hole mobility and the active electron channel. Our simulation indicated that there might be a band closure at higher temperatures for Bi-Sb alloys, which turned the system back to semi-metallic behavior, therefore limited the thermoelectric properties for p-type Bi-Sb alloys. Details will be discussed in the next chapter.

Chapter 4

Modeling and simulations

4.1 Two-band effective mass model analysis for Bi-Sb

4.1.1 Energy gap narrowing

To quantitatively understand the thermoelectric transport properties, resistivity and Seebeck coefficient of undoped $Bi_{85}Sb_{15}$ MS + SPS sample were simulated using a two-band effective mass model based on Boltzmann transport equation [103].

A parabolic band assumption was applied, and the L_a band was the conduction band while the H band was the valence band. The density of states can be written as:

$$D(E) = \frac{1}{2\pi^2}\left(\frac{2m_d^*}{\hbar^2}\right)^{\frac{3}{2}}\sqrt{E} \tag{4.1}$$

where m_d^* is the total density of states effective mass and E is the electron energy.

From the Boltzmann transport equations, we can get the expressions for the electrical conductivity and the Seebeck coefficient:

$$\sigma = -\frac{2e^2}{3m_c^*}\int_0^\infty \frac{\partial f}{\partial E} D(E) E \tau dE \tag{4.2}$$

$$S=\frac{1}{eT}\frac{\int_0^{\infty}\frac{\partial f}{\partial E}D(E)E\left(E-E_f\right)\tau dE}{\int_0^{\infty}\frac{\partial f}{\partial E}D(E)E\tau dE} \tag{4.3}$$

where e e is the unit charge, m_c^* is the conductivity effective mass, E_f is the chemical potential, τ is the scattering time and f is the Fermi-Dirac distribution function.

Within the two-channel transport model, we can write the resistivity ρ and Seebeck coefficient $S_{\text{ total }}$ as:

$$\frac{1}{\rho}=\sigma_{\text{total}}=\sigma_n+\sigma_p \tag{4.4}$$

$$S_{\text{total}}=\frac{\sigma_n S_n+\sigma_p S_p}{\sigma_n+\sigma_p} \tag{4.5}$$

where $\sigma_{n,p}$ and $S_{n,p}$ are the electrical conductivity and Seebeck coefficient components of the electron channel and hole channel, respectively.

The distance between the chemical potential and the bands will be affected if the band gap changes. The variation of the band gap could have effects on the TE transport properties. Details of the calculation and simulation parameters will be given in next section. In order to fully simulate the TE transport properties, it is necessary to allow a temperature dependent band gap. Results are shown in Fig. **??**. Band gap narrowing at increasing temperature is conceivable in the case of Bi-Sb alloys with a small band gap and robust semimetal-to-semiconductor crossovers. Furthermore, a lattice deformation that was observed near 150 K could also modify the bandgap [104].

4.1.2 Simulation method and parameters

In order to calculate the carrier concentrations (electron concentration n and hole concentration p), the charge neutrality equation was applied:

$$p+N_d^{+}=n+N_a^{-} \tag{4.6}$$

where N_d^{+}, N_a^{-} are the ionized donor and acceptor concentration, respectively.

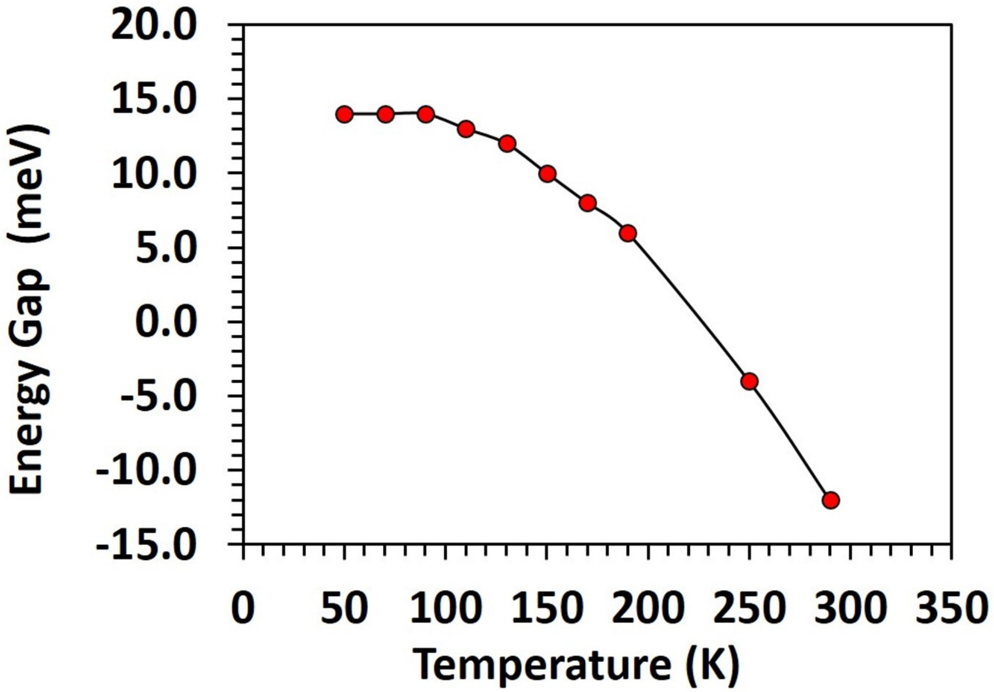

Figure 4-1: Energy Gap Fitted from Thermoelectric Properties Using a Two-band Effective Mass Model on $Bi_{85}Sb_{15}$ MS + SPS

For $Bi_{85}Sb_{15}$ MS + SPS, the Hall coefficient data at 50 K showed $|n-p| = \left|N_d^+ - N_a^-\right| \approx 1.6\times10^{23}m^{-3}$. . It was based on the assumption that the donors and acceptors were fully ionized above 50 K, and N_d^+, N_a^- would stay constant as the temperature changed.

The equations for the carrier concentrations were given by:

$$n = \int_{0(CBM)}^{\infty} f\cdot D_n(E)dE \tag{4.7}$$

$$p = \int_{-\infty}^{0(VBM)} f\cdot D_p(E)dE \tag{4.8}$$

where f is the Fermi-Dirac distribution function, $D_{n(p)}(E)$ is the density of states of the conduction (valence) band, CBM and VBM are the conduction band minimum and valence band maximum, respectively.

The Matthiessen's rule was used to calculate the scattering rate $\frac{1}{\tau_{\text{total}}}$ in the un-

Table 4.1: The parameters in the simulation of undoped $Bi_{85}Sb_{15}$ MS + SPS. The acoustic deformation potential ε_{ac} is around 20 eV.

Parameters	**Electrons**	**Holes**
$m_d^* \, (m_e)$	0.203	0.483
$m_c^* \, (m_e)$	0.025	0.084
N_v	3	6
$c_l \, (N/m^2)$	6.6×10^{10}	6.6×10^{10}

doped $Bi_{85}Sb_{15}$ MS + SPS.

$$\frac{1}{\tau_{\text{total}}} = \frac{1}{\tau_{\text{acoustic}}} + \frac{1}{\tau_{\text{impurity}}} \tag{4.9}$$

The first term $\frac{1}{\tau_{\text{acoustic}}}$ represents the acoustic deformation potential scattering (ADP) which is related to the electron-lattice interaction. The trend of the mobility caused by the ADP scattering is proportional to $T^{-1.5}$, The equation for $\frac{1}{\tau_{\text{acoustic}}}$ was given by [105]:

$$\frac{1}{\tau_{\text{acoustic}}} = \frac{\pi \varepsilon_{ac}^2 k_B T}{\hbar c_l} g(E) \tag{4.10}$$

where ε_{ac} is the acoustic deformation potential, c_l is the longitudinal elastic constant, $g(E) = \frac{1}{2\pi^2} \left(\frac{2m_b^*}{\hbar^2} \right)^{\frac{3}{2}} \sqrt{E}$ is the density of states effective mass of a single valley, $m_b^* = \frac{m_d^*}{N_v^{2/3}}$ and N_v is the number of valleys in the Fermi surfaces. The values for those parameters are listed in Table. 4.1.

The second term $\frac{1}{\tau_{impurity}}$ was coming from the ionized impurity scattering in this n-type material. It has the form $\tau_{\text{impurity}} = \tau_0 \left(E/k_B T \right)^{3/2}$, where τ_0 is constant [105]. The mobility trend will be proportional to $T^{1.5}$ if the ionized impurity scattering dominates. Following equation showed a simple exponential relationship between resistivity trend and energy gap:

$$\rho = \rho_0 \exp \left(E_g / 2 k_B T \right) \tag{4.11}$$

where ρ_0 is a constant and E_g is the band gap.

However, given the complexity of polycrystalline resistivity, instead of relying on Eq. 4.11 for using resistivity ρ data to determine the band gap at low temperature

($< 100K$), $E_g = 14$meV was chosen based on the data of single crystal Bi-Sb alloy [106]. The plots of the carrier concentration and mobility were shown in Fig. 4-2. It was shown that the rising of the resistivity of our $Bi_{85}Sb_{15}$ MS + SPS was not mainly caused by the carrier concentration related to the band gap. It was actually due to the ionized impurity scattering which significantly changed the mobility trend below 100K. Therefore, the thermal gap in the above resistivity expression Eq. 4.11 could not provide the real value of the band gap.

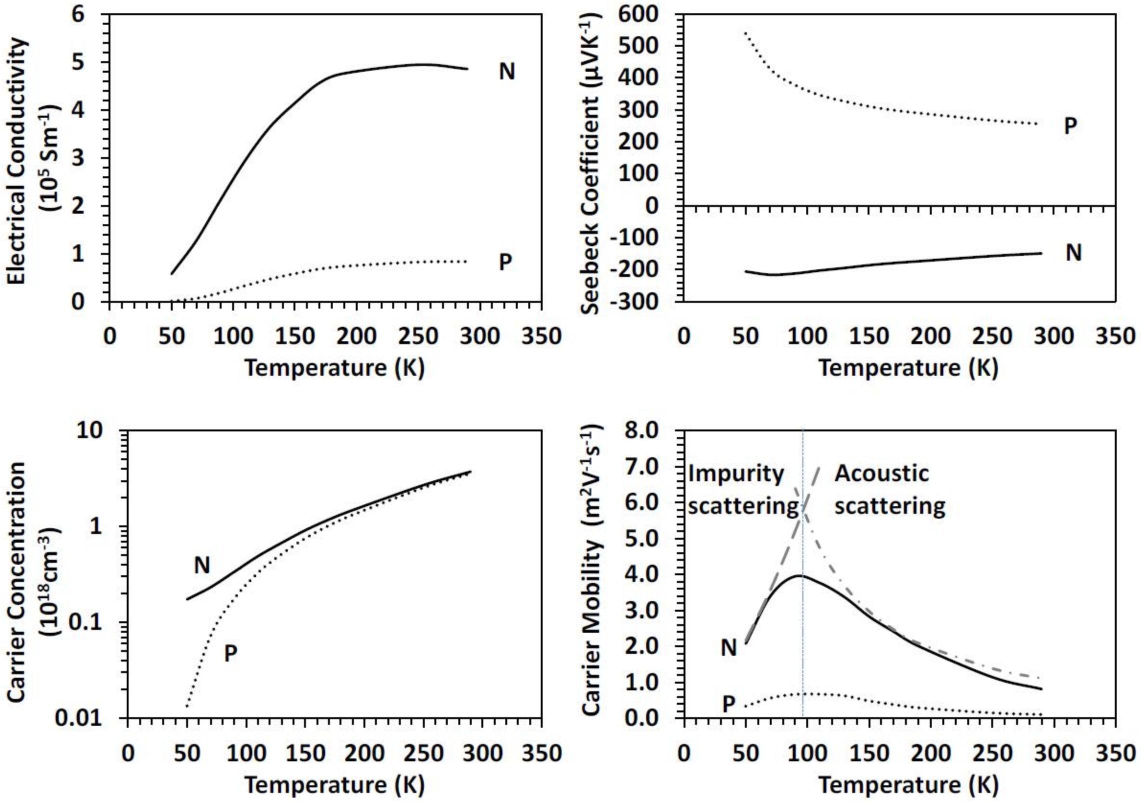

Figure 4-2: Simulation Results of Decoupled n, p Channel Transport Properties for $Bi_{85}Sb_{15}$ MS + SPS: Electrical conductivity, Seebeck coefficient, Carrier Concentration and Carrier mobility. (1) Solid lines: N-type electron carriers. (2) Dot lines: P-type hole carriers. (3) Dash line in mobility plot: ionized impurity scattering. (4) Dash dot line in mobility plot: acoustic deformation potential scattering.

4.1.3 Decoupling of electron and hole contributions to thermoelectric transport

According to bismuth's electronic structure, the quasi-ellipsoid centered at the L-point of Brillouin zone where electrons located are strongly elongated along a direction tilted by an angle ÏĘe out of the binary-bisectrix plane ($\phi_{\mathrm{e}} = 6 \pm 0.2^{\circ}$ at 4.2 K^3). This highly anisotropic shape led to unusually small effective masses along with two directions that resulted in a very high electron mobility [67], especially when compared with the hole mobility due to the much larger effective hole mass. Therefore, the undoped $Bi_{85}Sb_{15}$ system behaved as a strong n-type semiconductor dominated by electrons. By simulating the transport properties using a two-band effective mass model, we were able to decouple the contributions from electron and hole channels quantitatively. Results are shown in Fig. 4-2. The electrical conductivity and Seebeck coefficient components can be calculated using Eq.4.12 and Eq. 4.13. σ_n and S_n are the electrical conductivity component and Seebeck coefficient component of the electron channel, and σ_p and S_p are the electrical conductivity component and Seebeck coefficient component of the hole channel. m_c^* is the conductivity effective mass, the values can be found in Table. 4.1. μ is the chemical potential and E_g is the band gap. The same scattering mechanisms were used for electrons and holes to calculate the TE transport properties.

$$\sigma = \sigma_n + \sigma_p = -\frac{2e^2}{3m_{c,n}^*}\int_0^{\infty}\frac{\partial f_n}{\partial E}D_n(E)E\tau_n dE - \frac{2e^2}{3m_{c,p}^*}\int_0^{\infty}\frac{\partial f_p}{\partial E}D_p(E)E\tau_p dE \tag{4.12}$$

$$S = \frac{S_n\sigma_n + S_p\sigma_p}{\sigma_n + \sigma_p} = \frac{\frac{2e}{3Tm_{c,n}^*}\int_0^{\infty}\frac{\partial f_n}{\partial E}D_n(E)E(E-\mu)\tau_n dE - \frac{2e}{3Tm_{c,p}^*}\int_0^{\infty}\frac{\partial f_p}{\partial E}D_p(E)E\left(E+E_g+\mu\right)\tau_p dE}{-\frac{2e^2}{3m_{cp}^*}\int_0^{\infty}\frac{\partial f_n}{\partial E}D_n(E)E\tau_n dE - \frac{2e^2}{3m_{c,n}^*}\int_0^{\infty}\frac{\partial f_p}{\partial E}D_p(E)E\tau_p dE} \tag{4.13}$$

At low temperature, the alloy is extrinsic with electrons dominating the mobility, and ionized impurity scattering ($\sim T^{1.5}$) is the main scattering mechanism. While above 110K, the primary scattering mechanism becomes acoustic deformation potential scattering ($\sim T^{-1.5}$), which was shown in Fig. 4-2. There was a turning point for S_n at 70 K. This could be approximately explained using Mott's equation [107] for a single band:

$$S \sim m_d^* T \left(\frac{\pi}{3n}\right)^{2/3} \tag{4.14}$$

where m_d^* is the density of state effective mass, n is the carrier concentration. At low temperature, the system is n-type extrinsic, the number of electrons does not change dramatically with temperature. So, $|S_n|$ increases nearly linearly as the temperature increased. However, at higher temperatures, intrinsic excitation must be considered. The bipolar effect becomes increasingly important and the magnitude of the total Seebeck coefficient $|S_{\text{total}}| = \left|\frac{\sigma_n S_n + \sigma_p S_p}{\sigma_n + \sigma_p}\right|$decreases. It is worthy to note that S_p was found to have a relatively larger value compared with $|S_n|$ due to two main factors for hole carriers: (1) larger density of states effective mass than electrons; (2) lower carrier concentrations than electrons.

Chapter 5

Conclusion and future plan

5.0.1 Conclusion

In summary, the thermoelectric properties of nanobulk Bi-Sb have been investigated from different aspects for both n-type and p-type systems. The sample composition and experiments procedures were optimized.

For n-type Bi-Sb, a figure of merit ZT near 0.6 at $\sim$ 125K in zero magnetic field and up to 0.7 in a moderate in-situ magnetic field produced in compact BiSb/NdFeB sample. The ZT significantly exceeded that of polygrained BiSb reported to date. A low thermal conductivity benefited by the nanostructure created via rapid solidification was measured. A portable external magnet plates design was proposed, which made it possible to enhance TE properties by thermo-magnetic effects with a physical compact system. Therefore, the enhanced n-type Bi-Sb alloy could couple with a p-type cryogenic thermoelectric material in a cooling device.

On the other hand, the doping efficiency of Pb, Sn, Ge was studied for a better understanding of the doping mechanism in Bi-Sb system. The effect of transition metals as an n-type dopant was investigated, and used to weaken the electron mobility for better p-type TE properties. A figure of merit ZT $\sim$ 0.13 was achieved around 200K with Ni and Pb co-doped Bi-Sb alloy, which is one of the best performance in this temperature region for p-type Bi-Sb so far.

A two-band effective mass model was employed to simulate the thermoelectric transport properties, which uncovered a heretofore unreported narrowing of the indirect band gap with the increase of temperature. It partially explained the large difference in TE performance between n-type and p-type system.

5.0.2 Future plan

The future study on Bi-Sb alloys will include both n-type and p-type systems. For n-type Bi-Sb, one possible way to further decrease the thermal conductivity is using nano-composites. By introducing other nano-sized particles with decent thermoelectric properties into Bi-Sb system, it is possible to gain significant extra phonon scattering without damaging the current thermal powers. Bismuth oxides and bismuth telluride particles had been investigated before, but the dopping effects from oxygen and tellurium atoms decreased the Seebeck coefficient due to the sensitivity of the Bi-Sb system. Therefore, finding a more stable compound (Maybe still oxides) with decent TE properties could be the answer to get a good nano-composite.

Another pathway to improve n-type Bi-Sb is using doping effects. Even though we have studied a couple of different dopants, the investigation may not be complete. Putting dopants into the Bi-Sb system can modify the band structure, change the carrier concentration and mobilities. There could be one specific type of dopant that can provide optimal carrier environments which leads to a higher figure of merit ZT.

On the other hand, the study on p-type Bi-Sb alloy is more critical, considering a comparable p-type counterpart in the TE cooling device would significantly increase the energy conversion efficiency. However, the current picture of the energy gap narrowing sharply limited the performance of the p-type system. With the near 0 or even negative energy gap at higher temperatures for p-type Bi-Sb, the electrons were very easy to be activated against the hole carriers forming a two-channel system. One possible solution for this situation is to find some particular dopants that could support the energy gap, keep it from closing with the temperature. Alternatively, if there are some specific compositions or experiment treatments which could enhance the hole carrier mobilities to the same level as the electrons, then a higher p-type Seebeck coefficient may be achieved.

After all, these approaches will rely on a more in-depth understanding of the p-type electronic structures, therefore using density functional theory for more detailed analysis could be a good start.

Bibliography

[1] Thomas Johann Seebeck. *Magnetische polarisation der metalle und erze durch temperatur-differenz*. Number 70. W. Engelmann, 1895.

[2] Ling Bing Kong, Tao Li, Huey Hoon Hng, Freddy Boey, Tianshu Zhang, and Sean Li. Waste thermal energy harvesting (i): thermoelectric effect. In *Waste Energy Harvesting*, pages 263–403. Springer, 2014.

[3] Melvin Cutler and Nevill Francis Mott. Observation of anderson localization in an electron gas. *Physical Review*, 181(3):1336, 1969.

[4] Jean-Charles Peltier. Nouvelles expériences sur la caloricité des courants électrique. *Ann. Chim. Phys*, 56(371):371–386, 1834.

[5] Meng Chu Chen. The deep sea water and heat energy of thermoelectric generation study. In *Meeting Abstracts*, number 3, pages 706–706. The Electrochemical Society, 2015.

[6] N Adroja, Shruti B Mehta, and P Shah. Review of thermoelectricity to improve energy quality. *Int. J. Emerg. Technol. Innov. Res*, 2:847–850, 2015.

[7] Sun Jin Kim, Ju Hyung We, and Byung Jin Cho. A wearable thermoelectric generator fabricated on a glass fabric. *Energy & Environmental Science*, 7(6):1959, may 2014.

[8] Xiaolong Gou, Heng Xiao, and Suwen Yang. Modeling, experimental study and optimization on low-temperature waste heat thermoelectric generator system. *Applied Energy*, 87(10):3131–3136, oct 2010.

[9] Uttam Shyamalindu Ghoshal. Highly reliable thermoelectric cooling apparatus and method, July 31 2001. US Patent 6,266,962.

[10] Thermoelectric cooling from wikipedia. `https://en.wikipedia.org/wiki/Thermoelectric_cooling#cite_note-12`. Accessed: 2019-04-20.

[11] Long Chen, Xiaoyu Zeng, Terry M Tritt, and S Joseph Poon. Half-heusler alloys for efficient thermoelectric power conversion. *Journal of Electronic Materials*, 45(11):5554–5560, 2016.

[12] F Ioffe. Semiconductor thermoelements and thermoelectric refrigeration. *Infosearch, London*, page 39, 1957.

[13] Xiao Zhang and Li-Dong Zhao. Thermoelectric materials: Energy conversion between heat and electricity. *Journal of Materiomics*, 1(2):92–105, 2015.

[14] Jihui Yang and Thierry Caillat. Thermoelectric materials for space and automotive power generation. *MRS bulletin*, 31(3):224–229, 2006.

[15] Abram Fedorovich Ioffe. *Physics of semiconductors*. Infosearch, 1960.

[16] Zhi-Gang Chen, Guang Han, Lei Yang, Lina Cheng, and Jin Zou. Nanostructured thermoelectric materials: Current research and future challenge. *Progress in Natural Science: Materials International*, 22(6):535–549, 2012.

[17] G. JEFFREY SNYDER and ERIC S. TOBERER. Complex thermoelectric materials. In *Materials for Sustainable Energy*, pages 101–110. Co-Published with Macmillan Publishers Ltd, UK, oct 2010.

[18] Lei Yang, Zhi-Gang Chen, Matthew S. Dargusch, and Jin Zou. High Performance Thermoelectric Materials: Progress and Their Applications. *Advanced Energy Materials*, 8(6):1701797, feb 2018.

[19] Tiejun Zhu, Yintu Liu, Chenguang Fu, Joseph P Heremans, Jeffrey G Snyder, and Xinbing Zhao. Compromise and synergy in high-efficiency thermoelectric materials. *Advanced materials*, 29(14):1605884, 2017.

[20] Sang Il Kim, Kyu Hyoung Lee, Hyeon A Mun, Hyun Sik Kim, Sung Woo Hwang, Jong Wook Roh, Dae Jin Yang, Weon Ho Shin, Xiang Shu Li, Young Hee Lee, et al. Dense dislocation arrays embedded in grain boundaries for high-performance bulk thermoelectrics. *Science*, 348(6230):109–114, 2015.

[21] Kunling Peng, Xu Lu, Heng Zhan, Si Hui, Xiaodan Tang, Guiwen Wang, Jiyan Dai, Ctirad Uher, Guoyu Wang, and Xiaoyuan Zhou. Broad temperature plateau for high zt s in heavily doped p-type snse single crystals. *Energy & Environmental Science*, 9(2):454–460, 2016.

[22] Li-Dong Zhao, Gangjian Tan, Shiqiang Hao, Jiaqing He, Yanling Pei, Hang Chi, Heng Wang, Shengkai Gong, Huibin Xu, Vinayak P Dravid, et al. Ultrahigh power factor and thermoelectric performance in hole-doped single-crystal snse. *Science*, 351(6269):141–144, 2016.

[23] Heng Wang, Zachary M Gibbs, Yoshiki Takagiwa, and G Jeffrey Snyder. Tuning bands of pbse for better thermoelectric efficiency. *Energy & Environmental Science*, 7(2):804–811, 2014.

[24] Zhiwei Chen, Zhengzhong Jian, Wen Li, Yunjie Chang, Binghui Ge, Riley Hanus, Jiong Yang, Yue Chen, Mingxin Huang, Gerald Jeffrey Snyder, et al. Lattice dislocations enhancing thermoelectric pbte in addition to band convergence. *Advanced Materials*, 29(23):1606768, 2017.

[25] Yanling Pei, Gangjian Tan, Dan Feng, Lei Zheng, Qing Tan, Xiaobing Xie, Shengkai Gong, Yue Chen, Jing-Feng Li, Jiaqing He, et al. Integrating band structure engineering with all-scale hierarchical structuring for high thermoelectric performance in pbte system. *Advanced Energy Materials*, 7(3):1601450, 2017.

[26] Min-Seok Kim, Woo-Jin Lee, Ki-Hyun Cho, Jae-Pyoung Ahn, and Yun-Mo Sung. Spinodally decomposed pbse-pbte nanoparticles for high-performance thermoelectrics: enhanced phonon scattering and unusual transport behavior. *ACS nano*, 10(7):7197–7207, 2016.

[27] Sima Aminorroaya Yamini, David R. G. Mitchell, Zachary M. Gibbs, Rafael Santos, Vaughan Patterson, Sean Li, Yan Zhong Pei, Shi Xue Dou, and G. Jeffrey Snyder. Heterogeneous Distribution of Sodium for High Thermoelectric Performance of p-type Multiphase Lead-Chalcogenides. *Advanced Energy Materials*, 5(21):1501047, nov 2015.

[28] Di Wu, Li-Dong Zhao, Xiao Tong, Wei Li, Lijun Wu, Qing Tan, Yanling Pei, Li Huang, Jing-Feng Li, Yimei Zhu, et al. Superior thermoelectric performance in pbte–pbs pseudo-binary: extremely low thermal conductivity and modulated carrier concentration. *Energy & Environmental Science*, 8(7):2056–2068, 2015.

[29] HJ Wu, L-D Zhao, FS Zheng, D Wu, YL Pei, X Tong, Mercouri G Kanatzidis, and JQ He. Broad temperature plateau for thermoelectric figure of merit zt> 2 in phase-separated pbte 0.7 s 0.3. *Nature communications*, 5:4515, 2014.

[30] Zong-Yue Li and Jing-Feng Li. Fine-grained and nanostructured agpbmsbtem+ 2 alloys with high thermoelectric figure of merit at medium temperature. *Advanced Energy Materials*, 4(2):1300937, 2014.

[31] Rachel J Korkosz, Thomas C Chasapis, Shih-han Lo, Jeff W Doak, Yoon Jun Kim, Chun-I Wu, Euripidis Hatzikraniotis, Timothy P Hogan, David N Seidman, Chris Wolverton, et al. High zt in p-type (pbte) 1–2 x (pbse) x (pbs) x thermoelectric materials. *Journal of the American Chemical Society*, 136(8):3225–3237, 2014.

[32] Li-Dong Zhao, Shiqiang Hao, Shih-Han Lo, Chun-I Wu, Xiaoyuan Zhou, Yeseul Lee, Hao Li, Kanishka Biswas, Timothy P Hogan, Ctirad Uher, et al. High thermoelectric performance via hierarchical compositionally alloyed nanostructures. *Journal of the American Chemical Society*, 135(19):7364–7370, 2013.

[33] LD Zhao, HJ Wu, SQ Hao, Chun-I Wu, XY Zhou, Kanishka Biswas, JQ He, Timothy P Hogan, Ctirad Uher, Christopher Wolverton, et al. All-scale hierarchical thermoelectrics: Mgte in pbte facilitates valence band convergence and suppresses bipolar thermal transport for high performance. *Energy & Environmental Science*, 6(11):3346–3355, 2013.

[34] Qinyong Zhang, Hengzhi Wang, Qian Zhang, Weishu Liu, Bo Yu, Hui Wang, Dezhi Wang, George Ni, Gang Chen, and Zhifeng Ren. Effect of silicon and sodium on thermoelectric properties of thallium-doped lead telluride-based materials. *Nano letters*, 12(5):2324–2330, 2012.

[35] Qian Zhang, Feng Cao, Weishu Liu, Kevin Lukas, Bo Yu, Shuo Chen, Cyril Opeil, David Broido, Gang Chen, and Zhifeng Ren. Heavy doping and band engineering by potassium to improve the thermoelectric figure of merit in p-type pbte, pbse, and pbte1–y se y. *Journal of the American chemical society*, 134(24):10031–10038, 2012.

[36] Yanzhong Pei, Zachary M Gibbs, Andrei Gloskovskii, Benjamin Balke, Wolfgang G Zeier, and G Jeffrey Snyder. Optimum carrier concentration in n-type pbte thermoelectrics. *Advanced energy materials*, 4(13):1400486, 2014.

[37] Yanzhong Pei, Aaron LaLonde, Shiho Iwanaga, and G Jeffrey Snyder. High thermoelectric figure of merit in heavy hole dominated pbte. *Energy & Environmental Science*, 4(6):2085–2089, 2011.

[38] Min Hong, Zhi-Gang Chen, Yanzhong Pei, Lei Yang, and Jin Zou. Limit of z t enhancement in rocksalt structured chalcogenides by band convergence. *Physical Review B*, 94(16):161201, 2016.

[39] Yanzhong Pei, Heng Wang, and G Jeffrey Snyder. Band engineering of thermoelectric materials. *Advanced materials*, 24(46):6125–6135, 2012.

[40] Yanzhong Pei, Nicholas A Heinz, and G Jeffrey Snyder. Alloying to increase the band gap for improving thermoelectric properties of ag 2 te. *Journal of Materials Chemistry*, 21(45):18256–18260, 2011.

[41] Yanzhong Pei, Aaron D. LaLonde, Heng Wang, and G. Jeffrey Snyder. Low effective mass leading to high thermoelectric performance. *Energy & Environmental Science*, 5(7):7963, jun 2012.

[42] Joseph P Heremans, Mildred S Dresselhaus, Lon E Bell, and Donald T Morelli. When thermoelectrics reached the nanoscale. Technical report, 2013.

[43] Woochul Kim, Robert Wang, and Arun Majumdar. Nanostructuring expands thermal limits. *Nano Today*, 2(1):40–47, feb 2007.

[44] Qi Hao Zhang, Xiang Yang Huang, Sheng Qiang Bai, Xun Shi, Ctirad Uher, and Li Dong Chen. Thermoelectric Devices for Power Generation: Recent Progress and Future Challenges. *Advanced Engineering Materials*, 18(2):194–213, feb 2016.

[45] A. J. Minnich, M. S. Dresselhaus, Z. F. Ren, and G. Chen. Bulk nanostructured thermoelectric materials: current research and future prospects. *Energy & Environmental Science*, 2(5):466, may 2009.

[46] Chhatrasal Gayner and Kamal K. Kar. Recent advances in thermoelectric materials. *Progress in Materials Science*, 83:330–382, oct 2016.

[47] Siqi Lin, Wen Li, Zhiwei Chen, Jiawen Shen, Binghui Ge, and Yanzhong Pei. Tellurium as a high-performance elemental thermoelectric. *Nature Communications*, 7(1):10287, dec 2016.

[48] Kuei Fang Hsu, Sim Loo, Fu Guo, Wei Chen, Jeffrey S Dyck, Ctirad Uher, Tim Hogan, E K Polychroniadis, and Mercouri G Kanatzidis. Cubic AgPb(m)SbTe(2+m): bulk thermoelectric materials with high figure of merit. *Science (New York, N.Y.)*, 303(5659):818–21, feb 2004.

[49] Bo Yu, Mona Zebarjadi, Hui Wang, Kevin Lukas, Hengzhi Wang, Dezhi Wang, Cyril Opeil, Mildred Dresselhaus, Gang Chen, and Zhifeng Ren. Enhancement of Thermoelectric Properties by Modulation-Doping in Silicon Germanium Alloy Nanocomposites. *Nano Letters*, 12(4):2077–2082, apr 2012.

[50] Li-Dong Zhao, Shih-Han Lo, Yongsheng Zhang, Hui Sun, Gangjian Tan, Ctirad Uher, C. Wolverton, Vinayak P. Dravid, and Mercouri G. Kanatzidis. Ultralow thermal conductivity and high thermoelectric figure of merit in SnSe crystals. *Nature*, 508(7496):373–377, apr 2014.

[51] S H Yang, T J Zhu, T Sun, J He, S N Zhang, and X B Zhao. Nanostructures in high-performance (GeTe) _{<i>x</i>} (AgSbTe ₂) _{100âĹŠ <i>x</i>} thermoelectric materials. *Nanotechnology*, 19(24):245707, jun 2008.

[52] K. F. Hsu, Sim Loo, Fu Guo, Wei Chen, Jeffrey S Dyck, Ctirad Uher, Tim Hogan, E K Polychroniadis, Mercouri G Kanatzidis, Daryoosh Vashaee, Xiaoyuan Chen, Junming Liu, Mildred S. Dresselhaus, Gang Chen, and Zhifeng Ren. Cubic AgPbmSbTe2+m: Bulk Thermoelectric Materials with High Figure of Merit. *Science*, 303(5659):818–821, feb 2004.

[53] Jong-Soo Rhyee, Kyu Hyoung Lee, Sang Mock Lee, Eunseog Cho, Sang Il Kim, Eunsung Lee, Yong Seung Kwon, Ji Hoon Shim, and Gabriel Kotliar. Peierls distortion as a route to high thermoelectric performance in In4Se3-δ crystals. *Nature*, 459(7249):965–968, jun 2009.

[54] Huili Liu, Xun Shi, Fangfang Xu, Linlin Zhang, Wenqing Zhang, Lidong Chen, Qiang Li, Ctirad Uher, Tristan Day, and G. Jeffrey Snyder. Copper ion liquid-like thermoelectrics. *Nature Materials*, 11(5):422–425, may 2012.

[55] Lipeng Hu, Haijun Wu, Tiejun Zhu, Chenguang Fu, Jiaqing He, Pingjun Ying, and Xinbing Zhao. Tuning Multiscale Microstructures to Enhance Thermoelectric Performance of n-Type Bismuth-Telluride-Based Solid Solutions. *Advanced Energy Materials*, 5(17):1500411, sep 2015.

[56] T. Caillat, J.-P. Fleurial, and A. Borshchevsky. Preparation and thermoelectric properties of semiconducting Zn4Sb3. *Journal of Physics and Chemistry of Solids*, 58(7):1119–1125, jul 1997.

[57] Yintu Liu, Hanhui Xie, Chenguang Fu, G. Jeffrey Snyder, Xinbing Zhao, and Tiejun Zhu. Demonstration of a phonon-glass electron-crystal strategy in (Hf,Zr)NiSn half-Heusler thermoelectric materials by alloying. *Journal of Materials Chemistry A*, 3(45):22716–22722, nov 2015.

[58] âĂă Shawna R. Brown, âĂă Susan M. Kauzlarich, *, , âĂą Franck Gascoin, and âĂą G. Jeffrey Snyder*. Yb14MnSb11:âĂĽ New High Efficiency Thermoelectric Material for Power Generation. 2006.

[59] A. Saramat, G. Svensson, A. E. C. Palmqvist, C. Stiewe, E. Mueller, D. Platzek, S. G. K. Williams, D. M. Rowe, J. D. Bryan, and G. D. Stucky. Large thermoelectric figure of merit at high temperature in Czochralski-grown clathrate Ba8Ga16Ge30. *Journal of Applied Physics*, 99(2):023708, jan 2006.

[60] B. C. Sales, D. Mandrus, and R. K. Williams. Filled Skutterudite Antimonides: A New Class of Thermoelectric Materials. *Science (New York, N.Y.)*, 272(5266):1325–8, may 1996.

[61] Tingting Luo, Shanyu Wang, Han Li, and Xinfeng Tang. Low temperature thermoelectric properties of melt spun Bi85Sb15 alloys. *Intermetallics*, 32:96–102, jan 2013.

[62] Wenjie Xie, Shanyu Wang, Song Zhu, Jian He, Xinfeng Tang, Qingjie Zhang, and Terry M. Tritt. High performance Bi2Te3 nanocomposites prepared by single-element-melt-spinning spark-plasma sintering. *Journal of Materials Science*, 48(7):2745–2760, apr 2013.

[63] Machhindra Koirala, Hui Wang, Mani Pokharel, Yucheng Lan, Chuanfei Guo, Cyril Opeil, and Zhifeng Ren. Nanostructured YbAgCu ₄ for Potentially Cryogenic Thermoelectric Cooling. *Nano Letters*, 14(9):5016–5020, sep 2014.

[64] Gloria J. Lehr, Donald T. Morelli, Hyungyu Jin, and Joseph P. Heremans. YbCu2Si2âĂŞLaCu2Si2 Solid Solutions with Enhanced Thermoelectric Power Factors. *Journal of Electronic Materials*, 44(6):1663–1667, jun 2015.

[65] R. Wolfe and G. E. Smith. EFFECTS OF A MAGNETIC FIELD ON THE THERMOELECTRIC PROPERTIES OF A BISMUTHâĂŘANTIMONY ALLOY. *Applied Physics Letters*, 1(1):5–7, sep 1962.

[66] G. E. Smith and R. Wolfe. Thermoelectric Properties of BismuthâĂŘAntimony Alloys. *Journal of Applied Physics*, 33(3):841–846, mar 1962.

[67] B. Lenoir, H. Scherrer, and T. Caillat. Chapter 4 An overview of recent developments for BiSb Alloys. *Semiconductors and Semimetals*, 69:101–137, jan 2001.

[68] D. Schiferl, C. S. Barrett, and IUCr. The crystal structure of arsenic at 4.2, 78 and 299ÂřK. *Journal of Applied Crystallography*, 2(1):30–36, may 1969.

[69] M S Dresselhaus. Electronic properties of the group V semimetals. *J Phys Chem Solids*, 32(Suppl 1):3–33, 1971.

[70] V S Édel'man. Properties of electrons in bismuth. *Soviet Physics Uspekhi*, 20(10):819–835, oct 1977.

[71] Lax, Benjamin and J. G. Mavroides. *Advances in Solid State Physics*. Academic Press, New York, 1960.

[72] MS Dresselhaus. Electronic properties of the group v semimetals. *J Phys Chem Solids*, 32(Suppl 1):3–33, 1971.

[73] E.J. Tichovolsky and J.G. Mavroides. Magnetoreflection studies on the band structure of bismuth-antimony alloys. *Solid State Communications*, 7(13):927–931, jul 1969.

[74] M. Zahid Hasan and Joel E. Moore. Three-Dimensional Topological Insulators. *Annual Review of Condensed Matter Physics*, 2(1):55–78, mar 2011.

[75] G. Oelgart, G. Schneider, W. Kraak, and R. Herrmann. The Semiconductor-Semimetal Transition in Bi1âĹŠxSbx Alloys. *physica status solidi (b)*, 74(1):K75–K78, mar 1976.

[76] Metallos. Bi-sb-phase-diagram-example-greek. `https://commons.wikimedia.org/wiki/File:Bi-Sb-phase-diagram-example-greek.svg`. Accessed: 2019-05-09.

[77] A. L. Jain. Temperature Dependence of the Electrical Properties of Bismuth-Antimony Alloys. *Physical Review*, 114(6):1518–1528, jun 1959.

[78] Dale M. Brown and Fred K. Heumann. Growth of BismuthâĂŘAntimony SingleâĂŘCrystal Alloys. *Journal of Applied Physics*, 35(6):1947–1951, jun 1964.

[79] W.M. Yim and A. Amith. BiîŮÿSb alloys for magneto-thermoelectric and thermomagnetic cooling. *Solid-State Electronics*, 15(10):1141–1165, oct 1972.

[80] B. Lenoir, M. Cassart, J.-P. Michenaud, H. Scherrer, and S. Scherrer. Transport properties of Bi-RICH Bi-Sb alloys. *Journal of Physics and Chemistry of Solids*, 57(1):89–99, jan 1996.

[81] V.S Zemskov, A.D Belaya, U.S Beluy, and G.N Kozhemyakin. Growth and investigation of thermoelectric properties of BiâĂŞSb alloy single crystals. *Journal of Crystal Growth*, 212(1-2):161–166, jan 2000.

[82] Hiroyuki Kitagawa, Hiroyuki Noguchi, Toshiyasu Kiyabu, Masaki Itoh, and Yasutoshi Noda. Thermoelectric properties of BiâĂŞSb semiconducting alloys prepared by quenching and annealing. *Journal of Physics and Chemistry of Solids*, 65(7):1223–1227, jul 2004.

[83] R. Martin-Lopez, A. Dauscher, H. Scherrer, J. Hejtmanek, H. Kenzari, and B. Lenoir. Thermoelectric properties of mechanically alloyed Bi-Sb alloys. *Applied Physics A: Materials Science & Processing*, 68(5):597–602, may 1999.

[84] M. Miyajima, K. Takagi, H. Okamura, Gil Geun Lee, Y. Noda, and R. Watanabe. Thermoelectric properties of Bi-Sb composite prepared by mechanical alloying method. In *Fifteenth International Conference on Thermoelectrics. Proceedings ICT '96*, pages 18–21. IEEE.

[85] Yong-Hoon Lee and T. Koyanagi. Thermoelectric properties of n-Bi-Sb sintered alloys prepared by spark plasma sintering method. In *Proceedings ICT2001. 20 International Conference on Thermoelectrics (Cat. No.01TH8589)*, pages 278–281. IEEE.

[86] Hyungyu Jin, Christopher M Jaworski, and Joseph P Heremans. Enhancement in the figure of merit of p-type bi100- xsbx alloys through multiple valence-band doping. *Applied Physics Letters*, 101(5):053904, 2012.

[87] Z Chen, YM Han, M Zhou, CM Song, RJ Huang, Y Zhou, and LF Li. Improved thermoelectric properties of p-type bismuth antimony-based alloys prepared by spark plasma sintering. *Journal of electronic materials*, 43(4):1295–1301, 2014.

[88] Wikipedia. Diffusion pump. `https://en.wikipedia.org/wiki/Diffusion_pump`. Accessed: 2019-05-11.

[89] R. W. Cahn. *Physical Metallurgy*. Elsevier Science, 1983.

[90] Chuanbing Rong and Baogen Shen. Nanocrystalline and nanocomposite permanent magnets by melt spinning technique. *Chinese Physics B*, 27(11):117502, nov 2018.

[91] Wikipedia. Ball mill. `https://en.wikipedia.org/wiki/Ball_mill`. Accessed: 2019-05-11.

[92] Dmitri Kopeliovich. Spark plasma sintering [SubsTech].

[93] Felix Kaiser, Paul Simon, Ulrich Burkhardt, Bernd Kieback, Yuri Grin, Igor Veremchuk, Felix Kaiser, Paul Simon, Ulrich Burkhardt, Bernd Kieback, Yuri Grin, and Igor Veremchuk. Spark Plasma Sintering of Tungsten Oxides WOx (2.50 âĽď x âĽď 3): Phase Analysis and Thermoelectric Properties. *Crystals*, 7(9):271, sep 2017.

[94] Zhengliang Du, Tiejun Zhu, Yi Chen, Jian He, Hongli Gao, Guangyu Jiang, Terry M Tritt, and Xinbing Zhao. Roles of interstitial mg in improving thermoelectric properties of sb-doped mg 2 si 0.4 sn 0.6 solid solutions. *Journal of Materials Chemistry*, 22(14):6838–6844, 2012.

[95] Max L Tietze, Lorenzo Burtone, Moritz Riede, Björn Lüssem, and Karl Leo. Fermi level shift and doping efficiency in p-doped small molecule organic semiconductors: a photoelectron spectroscopy and theoretical study. *Physical Review B*, 86(3):035320, 2012.

[96] Tingting Luo, Shanyu Wang, Han Li, and Xinfeng Tang. Low temperature thermoelectric properties of melt spun Bi85Sb15 alloys. *Intermetallics*, 32:96–102, jan 2013.

[97] S. Ceresara, M. Codecasa, F. Passaretti, P. Tomeš, A. Weidenkaff, and C. Fanciulli. Thermoelectric Properties of InÂăSitu Formed Bi0.85Sb0.15/Bi-Rich Particles Composite. *Journal of Electronic Materials*, 40(5):557–560, may 2011.

[98] Min Zhou, Zhen Chen, Xinxin Chu, and Laifeng Li. Effect of Nano-ZrW2O8 on the Thermoelectric Properties of Bi85Sb15/ZrW2O8 Composites. *Journal of Electronic Materials*, 41(6):1263–1266, jun 2012.

[99] Mattias Gustavsson, Ernest Karawacki, and Silas E. Gustafsson. Thermal conductivity, thermal diffusivity, and specific heat of thin samples from transient measurements with hot disk sensors. *Review of Scientific Instruments*, 65(12):3856–3859, dec 1994.

[100] Silas E. Gustafsson. Transient plane source techniques for thermal conductivity and thermal diffusivity measurements of solid materials. *Review of Scientific Instruments*, 62(3):797–804, mar 1991.

[101] V.S Zemskov, A.D Belaya, U.S Beluy, and G.N Kozhemyakin. Growth and investigation of thermoelectric properties of BiâĂŞSb alloy single crystals. *Journal of Crystal Growth*, 212(1-2):161–166, jan 2000.

[102] Hyun-Sik Kim, Zachary M. Gibbs, Yinglu Tang, Heng Wang, and G. Jeffrey Snyder. Characterization of Lorenz number with Seebeck coefficient measurement. *APL Materials*, 3(4):041506, apr 2015.

[103] Xufeng Wang, Vahid Askarpour, Jesse Maassen, and Mark Lundstrom. On the calculation of Lorenz numbers for complex thermoelectric materials. *Journal of Applied Physics*, 123(5):055104, feb 2018.

[104] K. Malik, Diptasikha Das, A. K. Deb, V. A. Kulbachinskii, Velaga Srihari, S. Bandyopadhyay, and Aritra Banerjee. Evidence of iso-structural phase transition in rhombohedral Bi-Sb alloy. *EPL (Europhysics Letters)*, 115(5):58001, sep 2016.

[105] Mark Lundstrom. *Fundamentals of carrier transport.* Cambridge university press, 2009.

[106] B Lenoir, A Dauscher, M Cassart, Yu I Ravich, and H Scherrer. Effect of antimony content on the thermoelectric figure of merit of bi1- xsbx alloys. *Journal of Physics and Chemistry of Solids*, 59(1):129–134, 1998.

[107] Melvin Cutler and N. F. Mott. Observation of Anderson Localization in an Electron Gas. *Physical Review*, 181(3):1336–1340, may 1969.